

AMERICAN UNIVERSITY OF BEIRUT

ENHANCING THE EFFICIENCY OF SILICON BASED SOLAR CELLS
BY CONFINING PHOTON AND PHONON IN LOW DIMENSIONAL
STRUCTURES

by
YOUSSEF EL HELOU

A thesis
submitted in partial fulfillment of the requirements
for the degree of Master of Science
to the Department of Physics
of the Faculty of Arts and Sciences
at the American University of Beirut

Beirut, Lebanon
September 2017

AMERICAN UNIVERSITY OF BEIRUT

ENHANCING THE EFFICIENCY OF SILICON BASED SOLAR
CELLS BY CONFINING PHOTON AND PHONON IN LOW
DIMENSIONAL STRUCTURES

by
YOUSSEF EL HELOU

Approved by:

[]


Dr. Michel Kazan, Associate Professor
Physics Department

Advisor

[]

Dr. Leonid Klushin, Professor
Physics Department

Member of Committee

[]

Dr. Malek Tabbal, Professor
Physics Department

Member of Committee

Date of thesis/dissertation defense: [September 12, 2017]

AMERICAN UNIVERSITY OF BEIRUT

THESIS, DISSERTATION, PROJECT RELEASE FORM

Student Name:

Waddah
Middle

EL Helou
Last

Joussef
First

Master's Thesis
Dissertation

Master's Project

Doctoral

I authorize the American University of Beirut to: (a) reproduce hard or electronic copies of my thesis, dissertation, or project; (b) include such copies in the archives and digital repositories of the University; and (c) make freely available such copies to third parties for research or educational purposes.

I authorize the American University of Beirut, to: (a) reproduce hard or electronic copies of it; (b) include such copies in the archives and digital repositories of the University; and (c) make freely available such copies to third parties for research or educational purposes after:

One ---- year from the date of submission of my thesis, dissertation, or project.

Two ---- years from the date of submission of my thesis, dissertation, or project.

Three ---- years from the date of submission of my thesis, dissertation, or project.


Signature

September 15, 2017

Date

This form is signed when submitting the thesis, dissertation, or project to the University Libraries

ACKNOWLEDGMENTS

First and foremost, I would like to express my sincere gratitude to Prof. Michel Kazan, for being my advisor throughout this process, and also for his constant guidance, patience and understanding. I have profoundly benefited from my association with Prof. Kazan over the past two years, his enthusiasm in pursuing daunting problems and his passion for physics, made me enjoy the field even more.

I would like to also extend my sincere appreciation to Prof. Malek Tabbal for his willingness to help and for trying to set weekly meetings in the early stages of the thesis to discuss our progress.

I am also sincerely grateful for Prof. Leonid Klushin for his invaluable comments and sharp discussions and for showing great interest in the topic.

I would like to also thank my dear friend Abdo Iskandar, who is a PhD physics student for his support in crucial times. This support made the thesis completion possible. Iskandar is an integral member of the research team I am in.

A Special thanks to Prof. Digambara Patra, Associate Professor of Chemistry at the American University of Beirut (AUB), for opening his laboratory and allowing us to use his materials in the early thesis stages.

My sincere gratitude goes to the Central Research Science Laboratory (CSRL) crew, particularly to Mr. Joan Younes and Ms. Rania Shatila for their continuous readiness to lend a helping hand despite their heavy workload.

Finally, and most importantly, I would like to thank my family for their constant support, encouragement, patience and their unconditional love. My personal triumphs, no matter how small, have all been possible because of my family's sacrifice and faith in me. Without their support, it would have been impossible to endure these stressful times.

AN ABSTRACT OF THE THESIS OF

Youssef EL Helou

for

Master of Science

Major: Physics

Title: Enhancing the Efficiency of Silicon Based Solar Cells by Confining Photon and Phonon in Low Dimensional Structures

The interaction between phonons and photons, in ZnO NWs deposited on a silicon substrate and in silicon resonators arrays, is investigated by means of Raman spectroscopy.

The Raman spectra from the ZnO NWs deposited on a silicon substrate exhibited a significant Raman enhancement from the Si substrate and did not show any signatures of Raman scattering from the ZnO nanowires. The analysis of this result demonstrated that the localized Mie resonance in the ZnO cylindrical resonators induced forward scattering of the normally incident light into the Si substrate beneath the resonators, on which the ZnO nanowires are deposited.

On the other hand, the Raman spectra from large arrays of dielectric silicon resonators exhibited Raman enhancement accompanied with a downshift and broadening. The analysis of the Raman intensity and line shape using finite-difference time-domain simulations and a spatial correlation model demonstrated an interaction between photons confined in the resonators and phonons confined in nanosized crystallites in defective silicon in the resonators. It was shown that the Raman enhancement is due to collective lattice resonance inducing field confinement in the resonators, while the spectra downshift and broadening are signatures of the relaxation of the phonon wavevector due to phonon confinement in nanosized Si crystallites in the resonators. We found that as the resonators increase in height and their shape become cylindrical, the amplitude of their coherent oscillation increases and hence their ability to confine the incoming electric field increases.

CONTENTS

	Page
AKNOWLEDGEMENTS	v
ABSTRACT	vi
I. INTRODUCTION TO SOLAR CELLS	1
A. Silicon Based Solar Cells	1
B. Overview	2
1. History of Solar/Photovoltaic Cells and Materials	2
2. The Three Generations of Solar Cells	3
3. P-N Junction	5
C. Silicon-Based Solar Cells Models with Improved Efficiency	7
D. Our Attempts to Improve the Photovoltaic Effect in Silicon	17
II. EXPERIMENTS: GROWTH TECHNIQUES AND CHARACTERIZATION METHODS	22
A. Literature Review: ZnO NWs Growth Techniques	22
1. Hydrothermal Synthesis	22
2. Chemical Vapor Deposition	24
3. Vapor Phase Transport	24
B. Samples Preparation	25
1. Zinc Oxide Nanowires	25
2. Silicon Nanosstructuring Via Zinc Oxide Masking	28
C. Characterization Methods	31
1. Scanning Electron Microscope	31
a. SEM of ZnO NWs	35
b. SEM of Silicon Resonators Arrays	39
2. X-Ray Diffraction (XRD)	42
a. Basic Theory of X-Ray Diffraction	43
b. Bragg's Law	44
c. X-Ray Diffractometer	45
d. XRD Measurements of ZnO NWs	46

e. XRD Measurements of a Bare Silicon Substrate and of Si Resonators of Different Sizes and Shape	49
3. Raman Spectroscopy	51
a. Basic Theory of Raman Spectroscopy	52
b. Experimental Setup	56
4. Fourier Transform Infrared Reflectivity (FTIR)	61
a. Overview	61
b. Experimental Setup	62
III. RESULTS AND DISCUSSION	66
A. Zinc Oxide Nanowires	67
1. Properties, Characterizations and Applications	73
2. Application of ZnO NWs in Silicon-Based Solar Cells	73
B. Application of Periodic Silicon Resonators on a Silicon Substrate	77
C. Phonon Confinement Models for Raman Spectroscopy of Nanostructured Materials	81
D. Effect of the Shape of the Resonators in the First Sample Set	109
E. Effect of the Shape of the Resonators in the Second Sample Set	111
F. Effect of the Shape of the Resonators in the Third Sample Set	113
G. Comparative Evaluation of the Effect of Resonators Size and Shape on the Interaction Between Confined Photons and Confined Phonons	115
H. Electric Field Confinement Causes Substantial Crystallites Heating in the Resonators	116
I. Conclusion	118

BIBLIOGRAPHY

CHAPTER I

INTRODUCTION TO SOLAR CELLS

The nonrenewable energy depletion and the environmental destruction are two major areas of concern which scientists have been trying their hardest, in the past few decades, to find a convenient, sustainable and nature-friendly alternative. The development of solar cells, which is founded on one of the most desirable renewable energy source available, is considered to be one of the most efficient solutions to such problems. Solar cells are electronic devices which harness the sun's energy and convert it into electricity.

A. Silicon Based Solar Cells

Among the numerous types of solar cells that have been investigated whether in terms of their efficiency, cost, duration or reliability, the Silicon -based solar cells stand out as the strongest candidate for future development mainly because, silicon is a very well-studied material that is present in abundance in nature as silicon dioxide in sand and quartz, and it approximately accounts for about 26% of the earth's crust.

However, there are a lot of challenges regarding these devices, that have to do with their limited efficiency. First, silicon is an indirect band gap material, and therefore its optical absorption of sun's light is weak and is limited to solar photons with energies greater than the band gap energy of 1.12 eV. The Si indirect electronic band structure disfavors the electron photoexcitation from the maximum of the valence band to the minimum of the conduction band. In fact, the electron excitation from the maximum of the valence band to the minimum of the conduction band in crystalline Si requires the assistance of phonons to make up for the momentum mismatch between the maximum of the valence band and the minimum of the

conduction band. Second, Silicon is characterized by a high reflective surface, which causes the reflectance of the incoming radiation and therefore reducing drastically the number of photons that would contribute to the photovoltaic generation of electricity. Thus, these two mechanisms alone amount to the loss of about half of the incident solar energy in solar cells [1].

In the latter parts of this chapter, a thorough overview will be presented, regarding Si-based solar cells models that attempted to improve light absorption within the Si nanostructures, and thus enhance the efficiency of these photovoltaic cells.

B. Overview

1. History of Solar/Photovoltaic Cells and Materials

In 1839, French physicist Edmond Becquerel, discovered the photovoltaic effect in a liquid electrolyte [2]. Such effect represents a process through which electricity is generated when sunlight strikes a photovoltaic cell.

Light, which is an electromagnetic wave, is composed of packets of energy, the photons. Each photon carries a different amount of energy that corresponds to the different wavelengths of the solar spectrum. Therefore, when photons target a solar cell, they may either be reflected, absorbed or pass right through, depending on the energy band gap that characterizes the photovoltaic material. Whereas, the absorbed photons generate electricity.

It was not until 1873, that materials known as photoconductors were discovered by the English engineer Willoughby Smith, such as selenium, while testing materials for underwater telegraph cables. These materials could become electrically conductive when they absorb light. Afterwards, in 1876, William Grylls Adams and his student Richard Evans Day

learned that illuminating a junction between selenium and platinum has a photovoltaic effect. These discoveries formed a solid foundation for the first selenium solar cell construction in 1877, which American inventor Charles Fritts was able to successfully accomplish it without heat or moving parts in 1883, although such selenium solar cell had an efficiency of only 1%.

Several decades later, April 1954, when physicists at Bell Laboratories demonstrated the first practical silicon solar cell that reached an efficiency of 6%, and discovered that the latter is more efficient than selenium. Such findings led to the introduction of solar cells capable of powering electrical equipment. Afterwards, in 1956, silicon photovoltaics started to sell commercially, but their high production cost kept them from reaching a widespread of markets.

Fast forward to the current period, the synthesis of various structures of silicon nanocrystals led to the development of more improved silicon solar cells, whether in terms of efficiency that reached the 24% mark or in terms of a reduced cost, and hence this major tweak in the fabrication of silicon photovoltaic cells established three different generations of solar cells.

2. The Three Generations of Solar Cells

The main factors behind fabricating different types of solar cells are based on solid-state physics, chemistry and material science. These different types of solar cell technology can be divided into three categories: crystalline silicon technologies, thin-film technologies and other organic cells technologies.

For the first generation, the crystalline silicon technology, the photovoltaic cells are mainly based on silicon wafers which shows an efficiency that varies between 15 and 20%.

The market is saturated with such types of solar cells, which are mainly deployed on the rooftops, since they demonstrated good performance as well as a high stability. The drawback is that they require a lot of energy in production [3].

Moving on to the second generation, the thin-film technology, which is based on amorphous silicon, the efficiency for this one drops quite a bit, and varies in the 10-15% range. The cost for such solar cell generation is reduced in comparison to the first generation, since it avoids the usage of silicon wafers and adopts a lower material consumption strategy. However, the production for this type of photovoltaic cells requires vacuum processes and high temperature treatments, therefore there is a large energy consumption associated with the production of these solar cells. Therefore, such generation is based on scarce elements which is still a limiting factor in the price [3].

As for the third generation, the organic cells technology, such as small molecules or polymers, it incorporates the use of high performance experiment multi-junction solar cells which hold the world record in efficiency.

In addition, the high cost of production makes this generation of solar cells not so desirable commercially [3].

3. P-N Junction

A solar cell is basically a PN junction device. In other words, it is made of two types of semiconductors, a p-type silicon layer and an n-type silicon layer that interface each other. The n-type is characterized by an excess of electrons, while the p-type represents an excess in holes.

The p-type silicon is produced by adding atoms, such as boron or gallium, that have one less electron in their outer energy level than silicon. Thus, because of this deficiency in electron, boron or gallium, are required to form the bonds with the surrounding silicon atoms. Hence an electron vacancy or “hole” is created [4].

As for the n-type silicon, it is made by including atoms characterized by having one more electron than silicon on their outer energy level, such as phosphorus, which has five valence electrons. Phosphorus can form a bond with the surrounding silicon atoms, but one electron remains uninvolved in this process, and therefore it is free to move within the silicon structure [5].

These materials introduced above, whether it's the boron, gallium or phosphorous, are called dopants. A dopant is actually referred to as an impurity that is purposely introduced or mixed into a pure semiconductor material (for example the crystal silicon) in order to change or optimize the latter's electrical properties for specific application. Thus, a “P-type Doping” is the introduction of impurity atoms with one less valence electron than silicon (i.e. boron). Whereas, an “N-type Doping” is the introduction of impurity atoms with one more valence electron than silicon (i.e. phosphorous) [6].

The junction between the two layers is nonconductive. This non-conducting layer occurs because the electrons on one side of the junction (n-type) diffuse into the holes located on the other side of the junction (p-type). Furthermore, a depletion zone is formed around the junction, in which the electrons fill the holes, as it can be seen in Figure 1.1 below.

It should be noted that, as electrons diffuse, they leave positively charged holes in the n-type region. Similarly, the p-type region, where holes were initially present, is now filled with negatively charged ions.

This process keeps on going until equilibrium is reached, and a voltage difference is formed across the junction. This voltage difference is called the “built-in electric field” or “built-in voltage” [6].

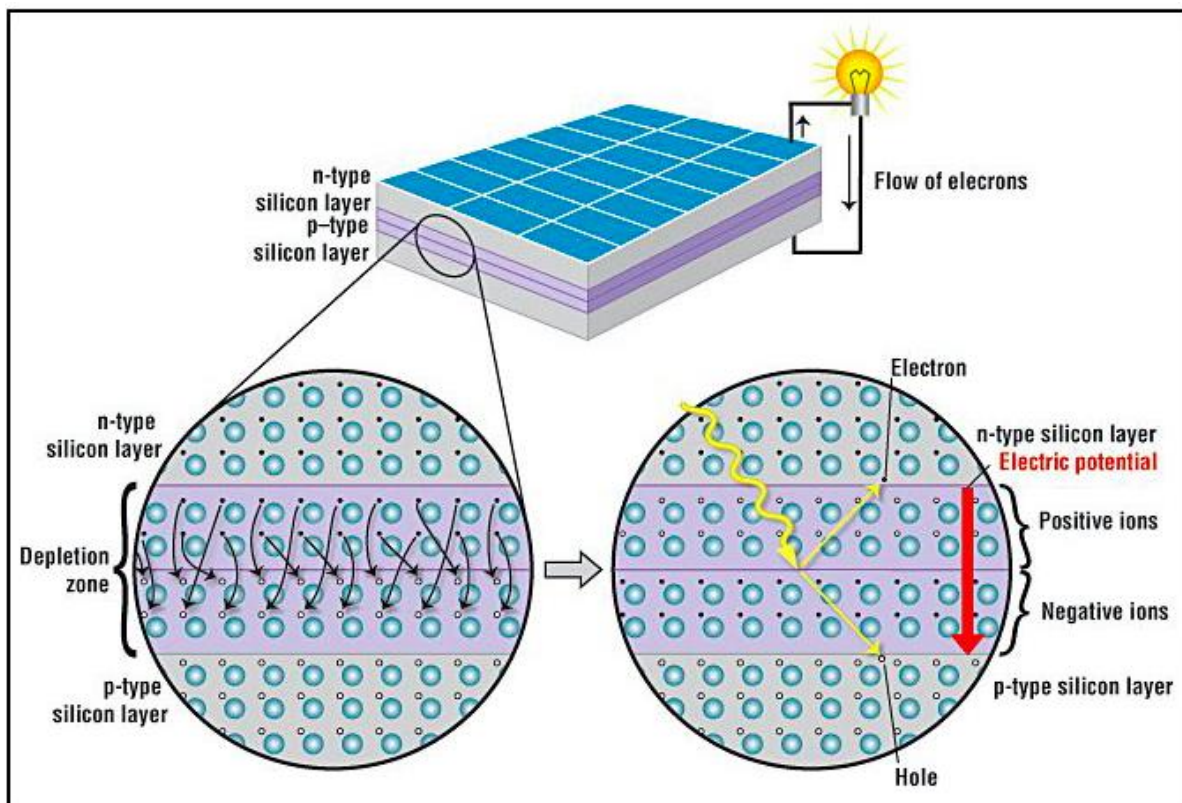


Fig. 1.1 Schematic representation of a solar cell, showing the n-type and p-type layers, with a close-up view of the depletion zone around the junction between the n-type and p-type layers [6].

C. Silicon based Solar Cells Models with Improved Efficiency

In this part of this chapter, an overview is presented, regarding Si-based solar cells models that attempted to improve light absorption within the Si nanostructures, and thus enhance the efficiency of these photovoltaic cells.

Keng-Te Lin et al. presented a model entitled, “Enhanced Efficiency of Silicon-Based Solar Cell by Surface Plasmon Resonance Effects Over Device Electrode”, that aims to improve the conversion efficiency in conventional silicon Si solar cells, by using Surface Plasmon Resonance SPR effects to harvest incident light energy over metal finger electrodes [7].

The target in mind for the authors was to test the SPR-based Extraordinary Optical Transmission EOT phenomenon on finger electrodes to increase the External Quantum Efficiency EQE of Si-based solar cells.

First and foremost, the study starts by using standard Si crystalline solar cell processes for fabrication.

Then, this experimental part resumes with the formation of n^+ -p junction by doping silicon with n^+ impurities and therefore creating a depletion zone between the implanted n^+ layer and the p-type substrate. The formation of the n^+ -p depletion region, and therefore the junction, is crucial for light harvesting in the solar cell.

Afterwards, a SiO_2 layer was deposited through low-pressure chemical vapor deposition on Si wafer with 20 nm thickness and etched to form contact area for current conduction.

Then, the metal electrode is deposited on top side, as seen in the Figure 1.2 below, by using Al-Si-Cu with 100 nm thickness, while the metal finger and holes are patterned by E-beam lithographic on the metal film.

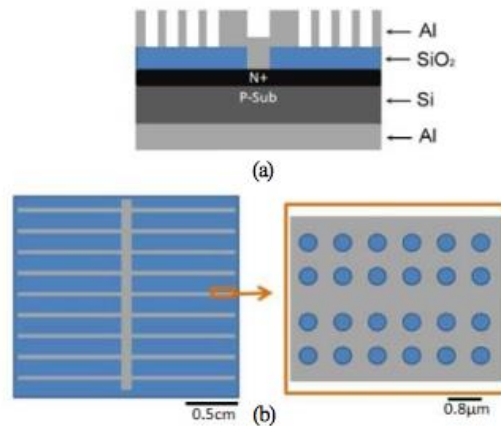


FIG. 1.2. Schematic showing tested device. (a) Cross-sectional view of a device featuring a metal hole array, for the SPR effect, on the Al electrode. (b) Top view of a device for mimicking a conventional solar cell; (left) the opaque metal finger electrodes are colored gray; expanded inset (right): design of the electrode for the suggested SPR effect.

Two devices were actually prepared, one with metal hole array on metal metal finger electrode and another device that mimics the conventional solar cell by using a simple metal finger electrode. The reason behind that is to showcase the difference between the solar cell presenting metallic hole arrays upon the metal finger regions, as seen in FIG. 1.2 (b), and the one that lacks any structure upon the metal finger regions.

After finalizing the experimental setups, a numerical method called the Three Dimensional - Finite Difference Time Domain (3D-FDTD) approach is used to determine the optical behavior of metal hole arrays and their structures.

As shown in FIG. 1.3 (a) below, plane waves, propagating from $2 \mu\text{m}$ above the metal hole arrays on Si substrate, are set; while three detectors are set up to study the behavior of that

incident light through metal arrays at the Air-Al interface, 100 nm below the Air-Al interface, and at the SiO₂ film-Si interface, respectively.

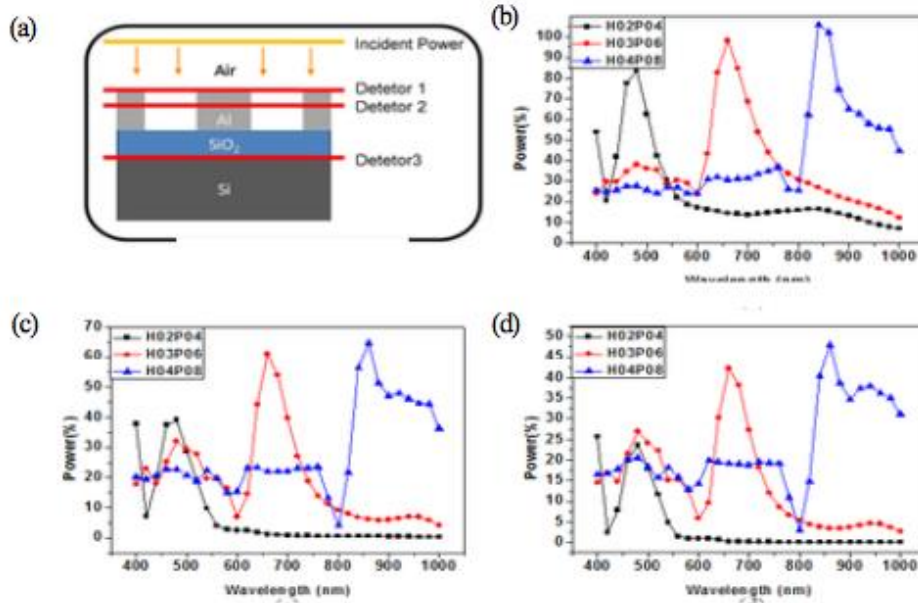


FIG. 1.3. (a) Layout for the FDTD simulation. (b)-(d) Calculated behavior of the 1st, 2nd and 3rd devices respectively, toward incident light passing through the metal hole arrays (Dimensions for the three structures are mentioned in the paragraph below).

In order to enhance the Extraordinary Optical Transmission EOT of Si-based solar cells, the spectra (Power Vs Wavelength) of the extraordinary optical transmittance in the metal hole arrays should match the working wavelength of the cells, knowing that the metal hole arrays on the finger electrodes structures are designed to have working wavelengths of 400, 600 and 800 nm, and various diameters of 200, 300 and 400 nm respectively.

It can be seen in FIG. 1.3 (b), which represents the transmitted spectra of the variation of Power as a function of Wavelength at the air-Al interface, that the transmitted peaks are

located at 480, 650 and 850 nm, which correspond to the actual SPR phenomena of the metal hole arrays structures.

However, FIG. 1.3 (c) and (d), which correspond the transmitted spectra of the metal hole array structures recorded 100 nm below the air-Al interface and that of the SiO₂-Si interface, measured respectively by Detectors 2 and 3, show clearly that the transmitted power decreased further as the waves propagated through the cavity. In other words, the intensities of the transmitted peaks decreased upon going from Detector 1 to Detector 3.

As for the electric field distributions through the metallic hole arrays of various sizes, Figure 4 displays the effect of incident passing through the following wavelengths: 480, 650 and 850 nm of the different metallic hole arrays structures.

For the first structure, shown in Figure 1.4 (a) below, (Working wavelength: wavelength: 400 nm, diameter:200 nm), for which the incident light is at 450 nm wavelength which is near the SPR transmission peak, it is obvious that there is a strong transmittance of electric intensity through the metallic hole arrays.

As the wavelength is increased to 650 and 850 nm (Figures 1.4 (b) and (c)), the electric field intensity transmitted through the first structure decreased immensely. This is due to a large size of wavelengths in comparison with a 200 nm diameter of the holes of the first structure.

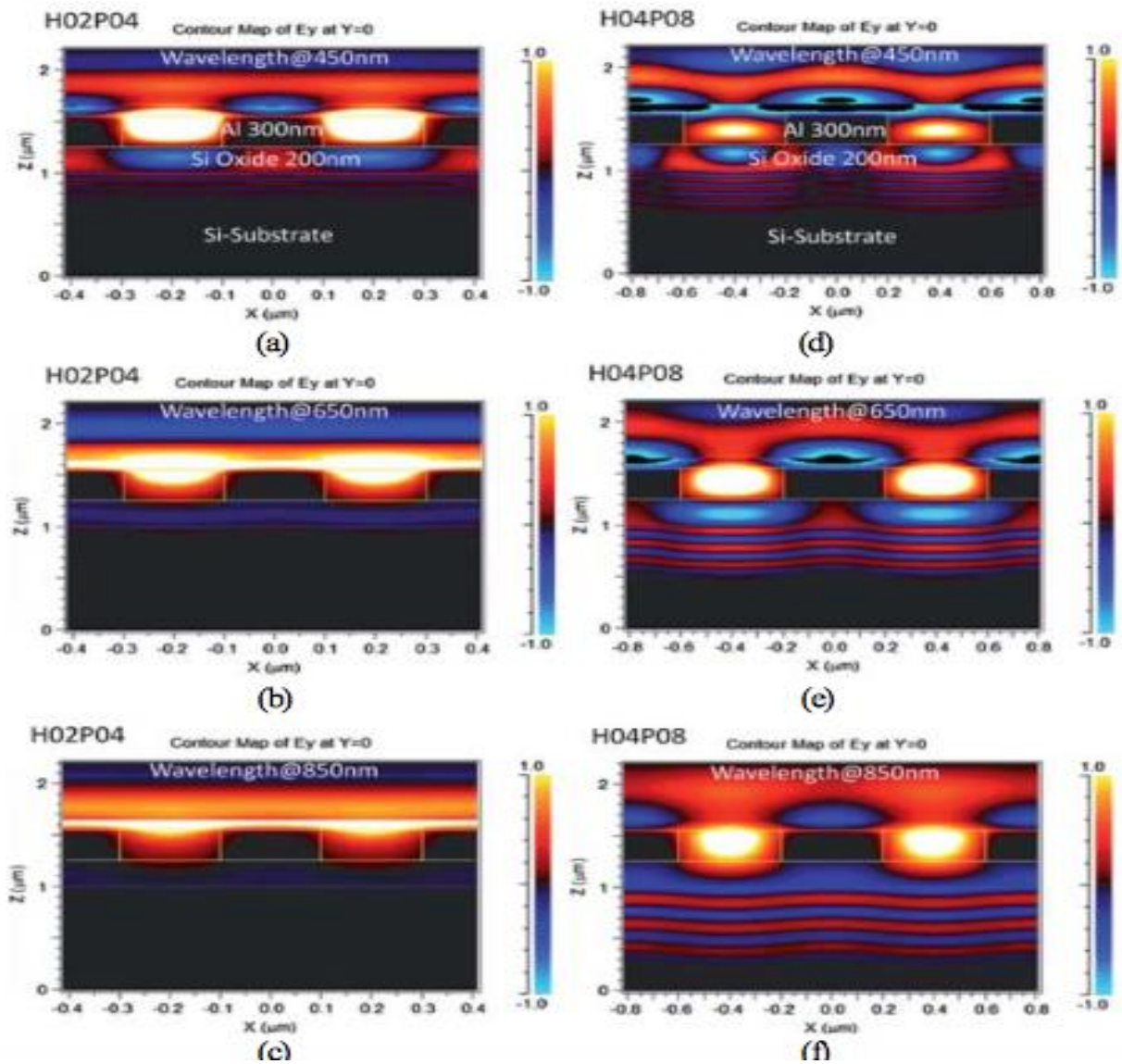


Fig. 1.4. Calculated electric field distributions after incident light had passed through the metallic hole arrays of (a) to (c), and (d) to (f) at wavelengths of 450 nm for (a) and (d), 650 nm for (b) and (e) and 850 nm for (c) and (f).

On the contrary, the third structure (Working wavelength: 800 nm, diameter: 400 nm), for which the incident light is at 850 nm, displays a clear transmittance of electric field intensity through the metallic hole arrays (Figure 1.4 (f), because the 850 nm wavelength is near the SPR transmission peak of this structure which is 800 nm. It is observable in Figures

1.4 (d) and (e), respectively, that when the wavelengths decreased, there still remained a fair amount of the electric field intensity passing through the third structure. Thus, incident light within the visible and NIR (Near Infrared Region) regimes could still be transmitted through a metallic hole array structure even if its SPR peak is in the NIR regime. In addition, patterning the transmission peak of the SPR with a larger hole diameter could improve the electric field intensity.

Afterwards, in order to draw a comparison between the conventional Si-based solar cell and the solar cell with metallic hole arrays on the metal finger electrodes, several tests have been conducted on four samples regarding their performance in terms of current density, as shown in the table below.

	Test	H02P04	H03P06	H04P08
Normal detecting area (cm ²)	0.327	0.327	0.327	0.327
Excess detecting area (cm ²)	0.000	0.165	0.165	0.165
Total photocurrent (mA)	1.430	2.197	2.710	2.800
Normal current (mA)	1.430	1.430	1.430	1.430
Excess current (mA)	0.000	0.767	1.280	1.370
Normal current density, J_{normal} (mA cm ⁻²)	4.377	4.377	4.377	4.377
Excess current density, J_{excess} (mA cm ⁻²)	0.000	4.651	7.758	8.303
Percentage ($J_{\text{excess}}/J_{\text{normal}}$)	0 %	106 %	177 %	190 %

Table I. Performance of solar cells featuring distinct finger electrode designs.

The “Test” sample in Table I, corresponds to the conventional Si-based solar cell without the metallic hole arrays. Whereas, H02P02, H03P06 and H04P08 correspond to the three structures discussed previously that have the following dimensions: $\lambda = 400 \text{ nm}, D = 200 \text{ nm}$; $\lambda = 600 \text{ nm}, D = 300 \text{ nm}$ and $\lambda = 800 \text{ nm}, D = 400 \text{ nm}$.

Furthermore, Table I displays the constituent parts of the total photocurrent in every tested device. Noting that for the Test sample/conventional solar cell, the major light absorption occurs in the detection region between the metal finger electrodes, without any contribution from the “normal detecting area” due to the absence of a covering metal. However, as for the other samples, irradiation energy could be absorbed in both the normal detecting area and the excess detecting area. The latter corresponds to the area of the entire sub-wavelength structure for SPR beneath the metal finger electrode.

The authors found that the total photocurrent was lowest for the Test sample among all the other measured devices. In addition, the excess current density J_{excess} is expected to be zero in the conventional solar cell (Test sample), which was the case experimentally. However, this was not the case for the other structures, which showed a significant value for the excess current density. This result implies that the presence of the SPR structures enhanced the generated photocurrent.

In addition, in order to determine whether the surface Plasmons were generated by the metal hole arrays over the metal finger electrodes, the ratio of J_{excess} to J_{normal} would allow such explanation.

If the ratio is zero, then no carriers are generated beneath the metal finger electrodes, as in the Test sample. If not, then the surface plasmons are activated by the sub-wavelength optical

structures to assist the incident light penetrating through the hole arrays, and therefore increasing the photocurrent.

Another model that proposes a new way of enhancing the efficiency of silicon solar cells, was presented in 2012 by Takuya Matsui et al.

This work entitled “High-Efficiency Thin-Film Silicon Solar Cells with Improved Light-Soaking Stability”, focuses on enhancing the light soaking firmness of Hydrogenated amorphous silicon films (a-Si: H) in both a-Si:H single-junction and a-Si:H/ μ c-Si:H tandem solar cells, by decreasing the density of Si-H₂ bond in amorphous silicon. However, a reduction in the density of Si-H₂ can be done only by preventing the incorporation of reactive species such as: SiH₂ and higher silane radicals into the film during the a-Si:H deposition [8].

Achieving stable Hydrogenated amorphous silicon films requires the use of an unconventional deposition technique, which involves the application of a triode electrode configuration in the Plasma-Enhanced Chemical Vapor Deposition (PECVD) process. The latter does not only help synthesizing stable intrinsic a-Si: H layers, but decreases as well the density of Si-H₂ in such films, which is not the case with a-Si: H films prepared by the conventional PECVD with a diode electrode configuration.

It should be noted that for the experimental part, the p-i-n junction solar cell that is fabricated in this work consists of the following, p-layer of “ μ c-Si: H” and n-layer of “ μ c-Si: H”, while in between those two regions the following layers are sandwiched: p-layer of a-SiC: H deposited over a triple undoped layers of a-SiC: H.

Furthermore, since in the triode PECVD technique, the synthesis of a-Si: H is dominated by the diffusion of long-lifetime radicals such as SiH₃; therefore, the incorporation of short-lifetime radicals such as SiH₂ and higher silane radicals (Si_nH_m with n>2), which are

the reason behind the formation of Si-H₂ bond structure in a-Si: H, can be reduced effectively by moving the surface of the growing a-Si: H film away from the plasma zone

For the purpose of showcasing the difference between the two different processes, the triode PECVD and the diode PECVD, FIG. 1.5, displayed below, shows the degradation characteristics of the a-Si: H p-i-n solar cells with 250 nm thick intrinsic i-layers prepared by triode and diode PECVD. It can be seen that the initial efficiencies of both processes are somehow comparable. However, long-term light soaking resulted in different stabilized efficiencies. Additionally, after 1000 h of light exposure, the solar cell fabricated by the triode PECVD shows a degradation of 11% in terms of conversion efficiency. Whereas, the solar cell that is prepared by diode PECVD, shows a degradation of 19%. In other words, the solar cell prepared by triode PECVD is much more stabilized and efficient due to the less amount of light-induced degradation.

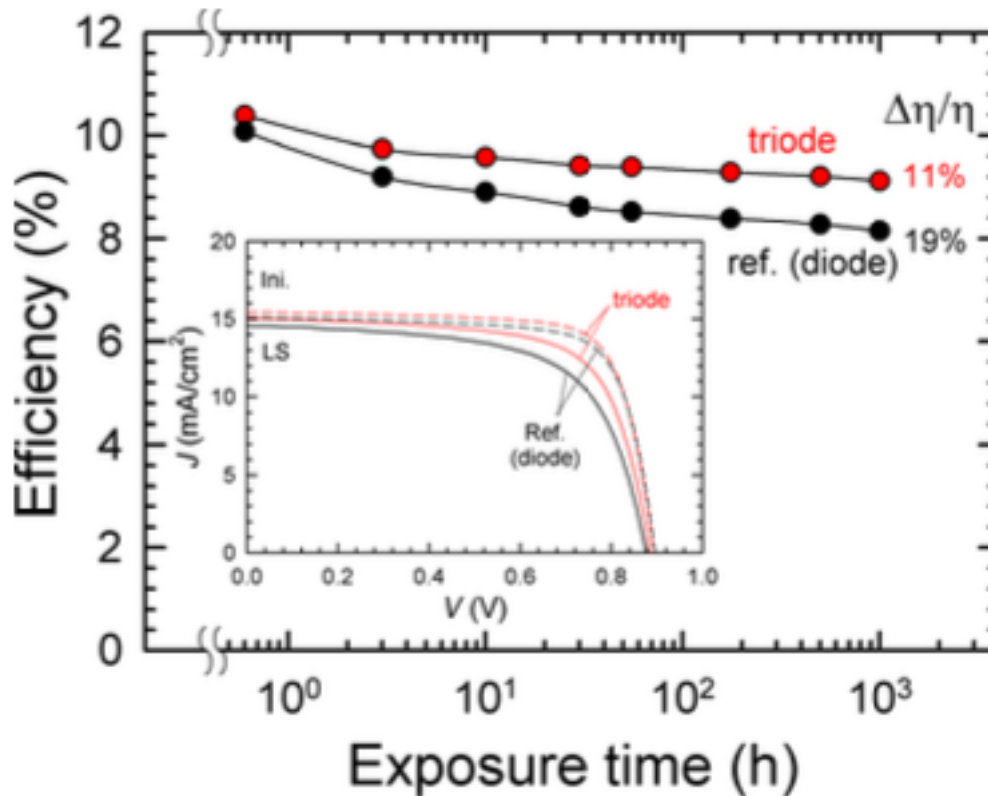


Fig. 1.5. Stability of the a-Si:H solar cells (i-layer thickness: 250 nm) under long-term light soaking. The inset shows the illuminated J-V curves of the initial and stabilized states (after 1000h illumination) for the corresponding solar cells.

In addition to proving the stability and the efficiency of these solar cells prepared by triode PECVD, it was also shown that their stability is less sensitive to the i-layer thickness variation (distance between the mesh and the substrate) in comparison with the standard cells prepared by diode PECVD.

Moreover, another method was proved to be beneficial in the reduction of the degradation ratio, and therefore leading to a more stable solar cells tandem. This method consists of a-Si:H i-layer, deposited by the triode PECVD technique described previously,

and is applied in an a-Si:H/ μ c-Si:H tandem solar cell. In other words, this technique consists of applying the a-Si:H layers as top-cell absorbers in the a-Si:H/ μ c-Si:H tandem solar cells.

The degradation ratio for this tandem solar cell was found to be 4%, which is remarkably lower than that of the single junction solar cells which was reported earlier (11%).

This improved stability of the tandem solar cell can be explained by the following reasons: First, the power generated by the a-Si:H top cell accounts for approximately two-third of the total output power of the tandem cell. Thus, the impact of the light-induced degradation of the a-Si:H top cell on the total output power is smaller than that for the a-Si:H single-junction solar cells. Another effect is that the light absorption in the a-Si:H top-cell is less than that in the single-junction solar cells because the visible light is also partly absorbed in the bottom cell in the tandem device.

D. Our Attempts to Improve the Photovoltaic Effect in Silicon

As it was mentioned earlier in this introduction, the two main challenges, regarding the pursuits to produce highly efficient photovoltaic effect in silicon Si, are centered around: the high reflectivity and the indirect electronic band structure of Si.

For that matter, in order to enhance significantly the efficiency of the photovoltaic effect in Si, the solutions proposed require the reduction in lossy light processes and coupling between trapped photons and phonons confined in low dimensional crystalline structures where the crystal translational symmetry is broken. In such short spatial correlation crystals, the total momentum need not be conserved in order to excite electrons from the maximum of the valence band to the minimum of the conduction band [9].

It was reported in works done by Eli Yablonovitch et al. [10] and Svetoslav Koynov et al. [11], that the reduction of lossy light and the coupling of the latter with trapped phonons can

be achieved by surface structuring in the form of periodic or random arrays of micron-sized pyramids or rods, On the other hand, Raman light scattering measurements have revealed evidence of phonon confinement in nanosized crystalline zones in highly defective crystals whereby the phonon selection rule is relaxed [12,13]. Thus, micron-sized structures are required to trap incident photons, whereas nanosized crystallites are needed to relax the requirement of total momentum conservation and enhance the probability of the electron transition from the maximum of the valence band to the minimum of the conduction band. This can be understood if we realize the large difference in wavelengths between photon and phonon. Consequently, in order to enhance the interaction between light and confined phonons, photons should be confined in micron-sized structures in which the spatial correlation length does not exceed a few nanometers.

Before tackling our attempt at a proposed solution, regarding the enhancement of the photovoltaic effect in Si, the surface structuring discussed above depends heavily on the nature of the resonators and on the way in which they are arranged on the substrate on which they are deposited. For instance, it is well known now that plasmonic nanoresonators forward scatter normally incident light towards the substrate on which they are deposited [14]. Although this process enhances the coupling between light and matter, it is much too lossy to confine photons. However, when identical plasmonic nanoresonators are arranged into a two-dimensional lattice such that the lattice period is comparable to the wavelength of the normally incident light, the fields scattered by the individual nanoresonators combine together to give rise to a field in the plane of the nanoresonators lattice [15,16]. If that field is spectrally close to the resonance frequency of the individual plasmonic nanoresonators, doubly degenerate hybrid light-plasmon collective modes (known as lattice resonance modes)

occur, inducing highly coherent plasmonic oscillations at all the lattice points [17]. This makes all the nanoresonators oscillate in a coherent fashion. This coherent oscillation of the nanoresonators makes the field scattered by one nanoresonator absorbed by the others [16], and consequently the electric field confined in the nanoresonators.

Similar to localized plasmon resonances in plasmonic nanoresonators, localized Mie resonances in dielectric resonators induce forward scattering and coupling of normally incident light into the substrate beneath the resonators [18,19], and localized Mie resonances at two-dimensional lattice points induce highly coherent oscillations in the dielectric resonators, which leads to strong field confinement in the dielectric resonators [20,21].

Our first attempt at a solution, consisted of the random deposition of Zinc Oxide nanowires ZnO NWs, of different diameters and different heights, on a Silicon substrate. The Raman spectra from the ZnO NWs deposited on a silicon substrate exhibited a significant Raman enhancement from the Si substrate and did not show any signatures of Raman scattering from the ZnO nanowires, signifying that there is no interaction between light and the ZnO Nws.

Thus, it is believed that the localized Mie resonance in the ZnO cylindrical resonators induced forward scattering of the normally incident light into the Si substrate, beneath the resonators, on which the ZnO nanowires are deposited, and therefore leading to the presence of a strong field in the Si substrate.

This solution might have solved one aspect of the problem regarding the photovoltaic enhancement in Si, which is the reduction of the lossy light, and proved that ZnO nanowires deposited on a Si substrate can be crucial and beneficial in trapping light within the latter. However, this method did not prove successful in terms of providing an interaction between

confined light and confined phonons in nanosized crystallites, and therefore solving the indirect band gap mismatch in Si, and this was proved clearly in the Raman spectra measurements, since the latter displayed an enhancement that is purely characteristic of the Silicon.

In another attempt at a better, improved solution that would solve both issues, the lossy light and the indirect electronic band structure of Si, different sets of Silicon nanoresonators arrays were periodically deposited into a two-dimensional lattice on a Silicon substrate. These Si resonators' form varied from truncated cones to pillars-like resonators, of different dimensions.

Knowing that the structuring of Si surface in the form of periodic micron-sized resonators over a large area exhibits natural development habit of nanosized crystallites embedded in highly defective Si in the resonators. In these short spatial correlation zones, the phonon selection rule may be broken due to phonon confinement, meaning that phonons located away from the zone center of the Brillouin zone can contribute to the optical phonon excitation, and hence contributing to the broadening and downshifting of the Raman spectrum of Si [22, 23]. In addition, the tips of tiny Si nanowires also present potential short spatial correlation zones for breaking the phonon selection rules [24,25]. Thus, dielectric resonators periodically arranged over a large area have the potential to simultaneously confine photons and generate confined phonons. In other words, dielectric resonators at lattice points can ensure the interaction between long living confined photons and nanosized crystallites in which the phonon selection rule is broken, and therefore providing an efficient way to successfully solve the challenges regarding the enhancement of the photovoltaic efficiency in Si.

After presenting our two attempts at a better solution, the important question, which arises now, is how the size and shape of the Si resonators influence the light confinement strength and its interaction with the nanosized crystallites in the resonators. In this contribution, we address this question and present a thorough experimental study of the effect of size and shape of Si resonators periodically arranged over a large area on the strength of the confined electric field and its interaction with nanosized crystallites in the resonators. We demonstrate the Si surface structuring that best confines the incoming electric field and ensures its interaction with nanosized crystallites for high efficiency Si-based photovoltaic cells. Raman spectroscopy has demonstrated a high potential for the evaluation of the confinement of the electric field [19, 21]. In addition, the analysis of Raman line shape can be carried out to yield quantitative determination of the spatial correlation length in the measured material [9,12,13,26,27]. For these reasons, we use Raman spectroscopy to evaluate the confined electric field and measure the crystallites sizes in the Si resonators.

CHAPTER II

EXPERIMENTS: GROWTH TECHNIQUES AND CHARACTERIZATION METHODS

A. Literature Review: ZnO NWs Growth Techniques

Among nanomaterials, Zinc Oxide is of immense interest in both academic research and industrial applications, due to its structural diversity that comes in many forms and various sizes, such as nanocombs, nanorings, nanohelices, nanosprings, nanobelts, nanocages and nanowires. Therefore, its fabrication procedures, in addition to its thermal and electrical properties have been reported by several authors using different techniques.

1. Hydrothermal Synthesis

Hydrothermal synthesis is a method used to produce single crystals, which involves water at elevated temperature and under high pressure, and it depends on the solubility of minerals in such hot aqueous solution. Therefore, water can act as both, a catalyst and an occasional solid-state phase component, during the nucleation and growth process. Typically, the temperature ranges between 100°C and 300°C and the pressure exceeds 1 atm. In comparison to other growth processes, hydrothermal synthesis is environmentally harmless, inexpensive and allows for the reduction of free energies for various equilibria.

Hanmei Hu et al. [28] synthesized ZnO nanowires and nanobelts on a large scale via a low temperature one-pot hydrothermal technique, using ZnCl_2 as zinc source, Na_2CO_3 as mineralizer, and sodium dodecyl sulfonate (SDSN) as morphology controller agent. Certain stoichiometry of each of these chemicals is added into a 50 mL Teflon-lined stainless steel autoclave, which is then filled up to 90% of the total volume with distilled water. The mixture is stirred for 40 min, and then the autoclave is sealed and maintained at 140°C for 12 h.

Afterwards, the resulting white product is filtered off, washed with ethanol and hot distilled water for several times, and then finally dried at 60°C for 4 h. The experimental results reveal that mineralizer Na₂CO₃ was introduced as a controllable agent for the crystal growth of ZnO, and the average diameter decreased with the increase of Na₂CO₃. In addition, the surfactant SDSN played a role in controlling the growth of belt-like ZnO.

Another synthesis technique was reported by Husnu EMrah Unalan et al. [29], that involves the use of microwave heating for the rapid hydrothermal synthesis of aligned ZnO nanowires on various substrates. First, they started by cleaning the various substrates used by sonication in acetone and isopropanol and then drying them in a nitrogen flow. Afterwards, a mixed solution of 10 mM of zinc acetate and 1-propanol was spin coated on n-type silicon (100), glass and polyethylene terephthalate (PET) substrates at 2000 rpm for 30 seconds. Then, the substrates were annealed at 100°C for 1 min after each spin coating to enhance adhesion followed by three layers of spin coating were performed, introducing a uniform seed layer. The substrates were then dipped in a mixture of equimolar 25mM zinc nitrate hexahydrate, hexamethylenetetramine and deionized water (resistivity 16 MΩ cm), then heated for 30 min inside a microwave oven at different power settings (120, 385 and 700 W) at atmospheric pressure, leading to a formation of vertical ZnO nanowires. The substrates were afterwards removed from the growth solution and washed with deionized water and dried under nitrogen flow. Structural analysis of the the grown ZnO nanowires has revealed the synthesis of high quality, well aligned ZnO nanowires with no structural damage, and it was observed that the length of the nanowires can be controlled by adjusting the microwave power and the growth time. This technique has proven to be the most effective among other hydrothermal techniques, since the growth rate by microwave heating was observed to be roughly 75-100 nm min⁻¹ much higher than other approaches.

2. Chemical Vapor Deposition

Chemical vapor deposition is a cheap and effective process for ZnO nanofabrication. It is a widely used materials-processing technology. It involves applying solid thin-film coatings to surfaces, or producing high-purity bulk materials and powders, as well as fabricating composite materials via infiltration techniques. Fundamentally, the process is a chemical reaction between the gaseous species at atmospheric pressure. These gaseous species are introduced into a chamber containing heated substrates to be coated, and generated by evaporation, reduction, or some other gaseous reaction. Chemical reactions take place on and near the hot surface of the substrate, resulting in the deposition of a thin film on the surface. There are many variants of Chemical vapor deposition, it can be done in hot-wall reactors and cold-wall reactors, with and without carrier gases, and at temperatures typically ranging from 200 to 1600°C [30].

O. Lupan et al. [31] reported the synthesis of ZnO nanowires and nanorods on a Silicon (1 0 0) substrate via chemical vapor deposition technique at 650°C, using metallic zinc of high purity and an oxygen-argon mixture as the starting reactants, while the synthesis was performed in a two-zone quartz flow reactor. It was shown that controlling the oxygen/zinc ratio beyond a certain critical ratio, as well as the position of the Si substrate in the growth zone of the quartz flow reactor, have contributed to ZnO of different shapes, either nanowires or nanorods, of different lengths, yet vertically well aligned. The average diameter of these high quality nanowires ranged between 50 to 200 nm.

3. Vapor Phase Transport

Vapor phase transport (VPT) is an atomic deposition process in which material physically or chemically vaporized from a solid source and is transported onto substrate

where it condenses and deposits. Many vaporization approaches can be distinguished. VPT can be in the form of thermal evaporation (by heat), laser ablation (by photons), sputtering (by positive ions or electron beam) [32]. In that regard, we mention the work of Michael H. Huang et al. [33] who reported the use of the vapor-phase transport process to grow ZnO nanowires via the vapor-liquid-solid (VLS) mechanism. The Zn vapor was generated using carbothermal or hydrogen reduction of ZnO. Afterwards, the ZnO were grown on Au-coated silicon substrates by heating a 1:1 mixture of ZnO and graphite powder to 900-925⁰C under a constant flow of argon for 5-30 min. Structural characterizations of the grown ZnO nanowires were carried out using the X-ray diffraction XRD and the scanning electron microscope SEM. The XRD revealed a high crystallinity for all samples since the diffraction peak can be indexed to a hexagonal structure of bulk ZnO, while the SEM revealed a uniform morphology of ZnO nanowires. The diameters of the nanowires ranged from 80 to 120 nm and their lengths between 10 to 20 μm. It was found that higher temperatures and longer reaction durations contributed to a significant crystal overgrowth and produced nanowires with larger diameters. In addition, a hydrogen reduction introduced a decrease in the nanowires' diameter, while the thermal treatment was done at 525-575⁰C and lasted for 30 min.

B. Samples Preparation

1. Zinc Oxide Nanowires

Zinc Oxide nanowires were first synthesized using a hydrothermal technique, which was proposed and carried on in Professor Digambara Patra's laboratory in the Chemistry Department. However, this method did not yield the desired expected results, there was an

abundance of strong agglomeration around the ZnO nanowires as shown in FIG. 2.1(a. and b.).

This method is strongly prone to human errors, since it does not involve the use of a machinery to synthesize the nanowires.

In addition, the X-Ray Diffractometer (XRD) results were not in agreement with the typical XRD pattern, we noticed the appearance of additional peaks that are probably attributed to the existence of these clusters or impurities around the nanowires.

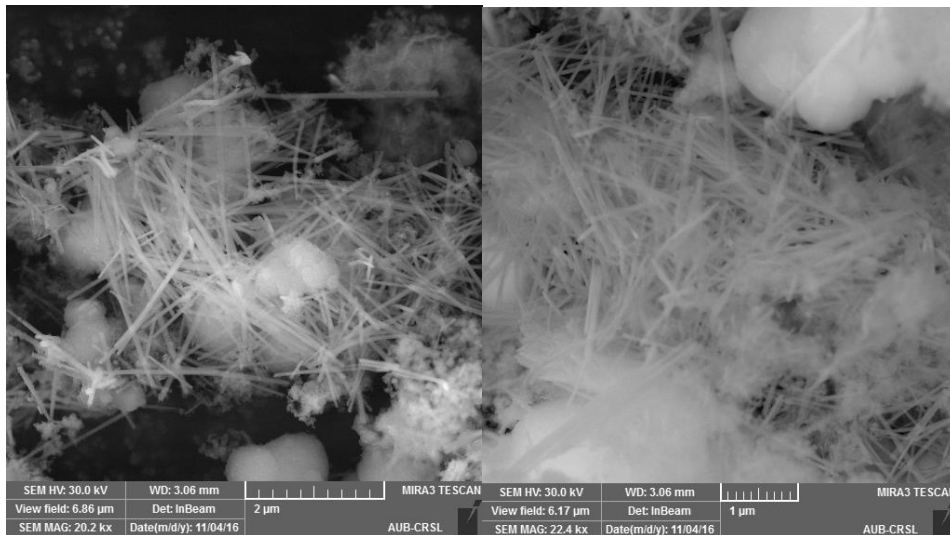
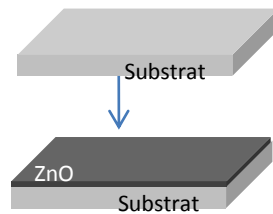


Fig. 2.1 (a and b) Scanning electron micrographs showing an abundance of strong agglomeration around the ZnO nanowires

Afterwards, we proceeded to use a well aligned, small diameter Zinc Oxide nanowires grown on a silicon substrate, and which were synthesized and imported from a laboratory in France through the help of the PhD student Abdo Iskandar. The synthesis process of these ZnO nanowires consists of these two following parts:

Preparation of seed ZnO layer

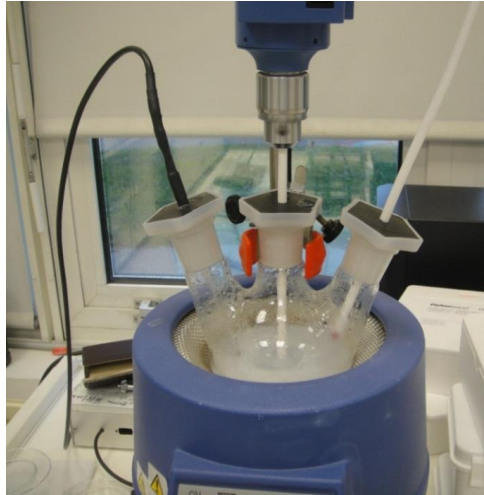
ZnO seed layer is a very thin layer (15-20nm) consisting of ZnO nanoparticles that act as a nucleation layer for the growth of ZnO NWs. In this study, the seed layer was prepared in the following manner: 2.197g of Zinc Acetate ($\text{Zn}(\text{CH}_3\text{COO})_2 \cdot 2\text{H}_2\text{O}$) was dissolved in 20ml of ethanol by stirring constantly for a time period of 24 hrs. This solution was spin-coated onto a clean silicon substrate. After spin-coating the seed layer was annealed at 400°C on a hot plate for a time period of 10 mins. The spin coating was repeated twice, followed by annealing after each spin coating step.



Growth of ZnO NWs

For the growth of ZnO NWs, chemical bath deposition method was used. In this method, 0.025M Zinc Acetate was dissolved in 250 ml of deionized water. This solution was stirred for a few minutes, following which 0.3 ml of ammonium hydroxide (concentration 28%) was added to this solution maintained under constant stirring. This solution was then heated to 87°C in a three-neck flask. Once the temperature was attained, the Si substrate with the ZnO seed layer was introduced into the solution for a time period of 15 minute or more depending on the length of NWs required. ZnO NWs grew on this substrate. Finally, the sample was thoroughly washed with deionized water and dried in air.

The same synthesis process was repeated by varying the concentration of the Zinc Acetate and fixing the other parameters.



2. Silicon Nanostructuring via Zinc Oxide Masking

In this part, we report on the growth of resonators in the form of pillars and truncated cones, which were fabricated in Si by reaction etching (RIE) using a ZnO hard mask, while Lithography of 355 nm laser interference was employed to define the mask patterns.

Nowadays, the growing need of material structuring at micro and nanoscale level, in material science, has led to the development of various methods such as the conventional reactive-ion etching (RIE). This is due to the fact that some applications require a well-defined and ordered structures as it allows creation of super-repellent materials for antireflective surfaces for solar cells. Furthermore, for structuration of any kind of materials, the choice of the mask plays a crucial role as far as plasma-etching process is concerned, since the mask should offer a high selectivity in addition to presenting an ease in the implementation of its deposition and structuring. For instance, for deep etching, hard mask materials are usually employed.

However, the utilization of a hard mask involves implementation of additional steps in the fabrication process, and at times the material used as a mask cannot be completely removed from the structures after etching. Such arising problem has led to the use of ZnO as a mask for creating structured silicon, since it presents many advantages over other materials. [34]

The method proposed is a combination of two techniques: Laser interferential lithography (LIL) which is used for patterning and RIE technique using zinc oxide as a mask.

As it can be seen in FIG. 2.2 below, ZnO layer is first deposited on the Silicon substrate followed by the deposition of a photoresist layer by spin-coating on top of it (FIG. 2.2a). Specific patterns are created in the photoresist lithographically by simple or multiple exposures of 355 nm laser interference followed by the development step. In other words, a square lattice with circular patterns of period 700 nm was created by a double exposure of the sample, whereby the diameter of the features could be controlled by changing the exposure time. (FIG. 2.2b). Afterward, ZnO is selectively wet-etched by means of a photoresist mask (FIG. 2.2c). Then, after transferring the pattern to the ZnO layer, the photoresist can then be removed by a simple step which involves chemical dissolution (FIG. 2.2d). Afterwards, the resulting ZnO pattern is transferred to the substrate by reactive-ion etching (FIG. 2.2e). Finally, the residual mask is etched off in an acidic solution consisting of ferric chloride (10^{-2} M $\text{FeCl}_3 \cdot \text{H}_2\text{O}$), FIG. 2.2 (f) [35].

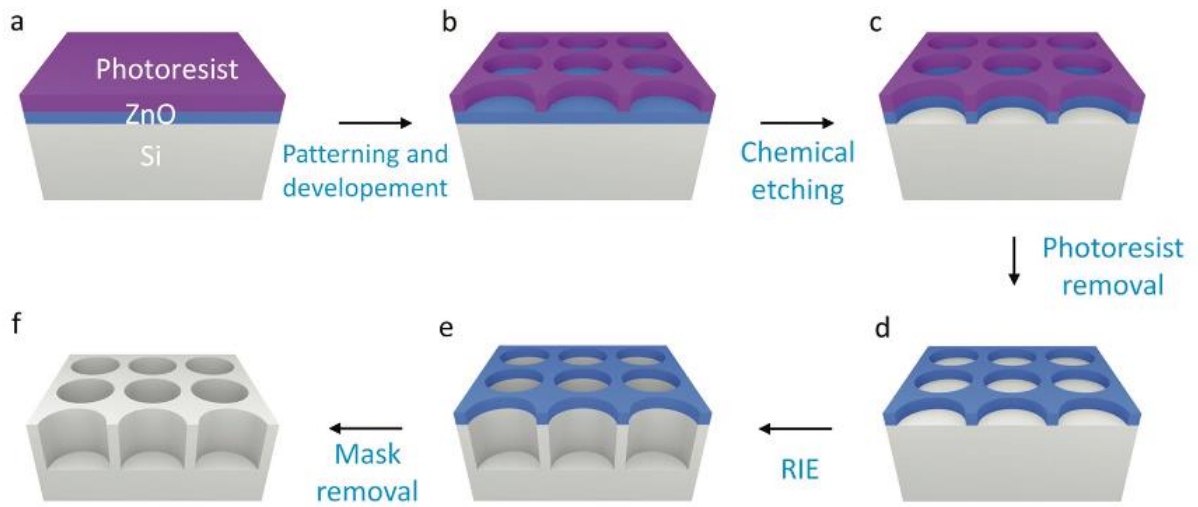


FIG. 2.2 Schematic representing the various stages involved in the ZnO mask fabrication process and its transfer to the Si substrate.

Thereafter, 10 min of Si etching using SF_6/O_2 gas mixture was conducted in a Plassys MU400 reactor, performed with RIE power of 90 W, the depth of the features is about 2 μm , with the etching rate for silicon was 240 nm min^{-1} . The ZnO mask still remains on top of the structures and its thickness remains comparable to the initial one. Noting that the etching rate of silicon is 20 times higher as compared to the one of ZnO. The height of the resonator could be controlled by varying the etching time.

The same synthesis processes were repeated by varying the etching time, the Power of the laser beam, and the temperature of the SF_6/O_2 gas mixture under which etching was performed.

C. Characterization Methods

1. Scanning Electron Microscope (SEM)

Scanning Electron Microscope (SEM) is a magnification tool that is used to produce images of a sample by scanning it with a focused beam of electrons.

The high resolution images produced provide topographical, morphological and compositional information about the studied samples.

The Scanning Electron Microscope examines the sample's surface in a raster pattern using an electron beam which interacts with atoms in the sample, and then the detected signal is combined with the beam's position to produce an image.

The main components of a typical SEM are the following: electron column, detectors, display, vacuum system, sample chamber and electronics control. (FIG. 2.3)

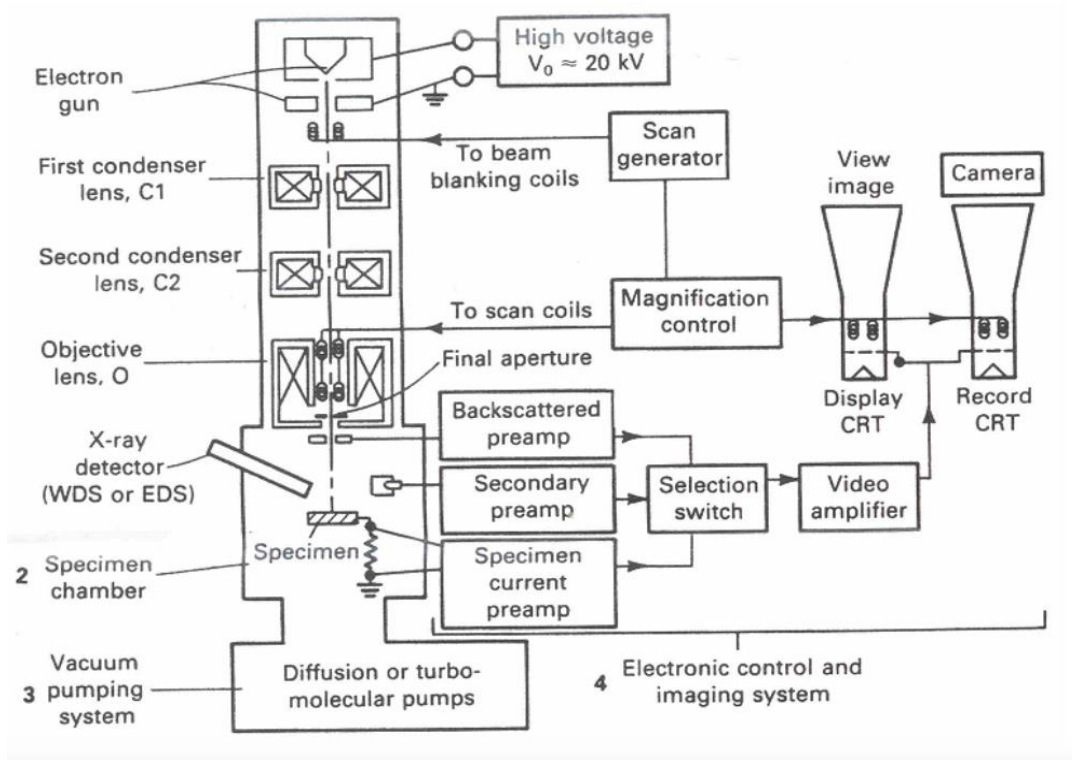


FIG. 2.3. Optical diagram for Scanning Electron Microscope

Electron Column: It consists of an electron gun and two electromagnetic lenses. The electron gun fitted with a tungsten filament cathode, generates a beam of energetic electrons down the column by heating the filament at high temperature (about 2800 K).

The reason behind the usage of a tungsten material is its highest melting point and lowest vapor pressure of all metals. As for the purpose of the three electromagnetic lenses, it can be divided into two parts: The combination of the first two lenses, condenser lens C_1 and condenser lens C_2 , de-magnify the beam into a smaller area called “spot size” or “resolution”. While the third lens, which is called the objective lens, helps focusing the beam onto the studied specimen, with the help of a magnetic field that is generated inside the lenses. These lenses, altogether, operate in vacuum.

Sample Chamber: it is the stage that stably supports the sample and moves smoothly. It must be solid and insulated from exterior conditions and vibrations in order to produce a clear image. The sample holder can move horizontally, vertically, tilt or rotate, depending on the field of view. The vertical movement provides a variation in the image resolution, and a change in the depth of focus.

Detectors: Out of the various detectors that can be used, we distinguish the secondary electron detector (SE) used to detect the secondary electrons emitted from the sample. By changing the voltage applied on this detector, you can control the number of secondary electrons to be collected. This type of detectors is used to provide some surface topography information which are displayed on a computer monitor. As for the other detectors such as, the Back-Scattered electron detector and the X-Ray detector, they provide information from a relatively deep region about the composition of the specimen, and they are used for elemental

analysis such as the characteristics of individual elements that constitute the specimen.

Vacuum System: The sample chamber must be kept at a high vacuum of 10^{-3} to 10^{-4} Pa, to protect the sample inside from interference with the external conditions and reduce any possible contamination, such as the air particles which would block the electrons beam path towards the specimen, and hence distorting the surface topography images.

A normal Scanning Electron Microscope operates at a high vacuum. It used scanning coils which produce a magnetic field by using fluctuating voltage, so that they are able to manipulate the electron beam and move it precisely over a defined region of the sample. Upon interaction of the electron beam with the surface of the specimen, it dislodges secondary electrons from the surface of the sample which are then attracted by a secondary electron detector. Those secondary electrons are characterized by low energy electrons, and can produce a very high resolution images of a sample's surface topography.

Additional sensors detect the Back-Scattered electrons and characteristics X-Rays. The Back-Scattered electrons are reflected from the sample by elastic scattering. They have a wide range of energy that could equate the incident electron energy or go down to 50 eV. Since the intensity of the Back-Scattered electrons is strongly related to the atomic number (Z) of the specimen, hence the images obtained by Back-Scattered electrons provide information about the distribution of different elements in the sample.

As for the characteristic X-Rays, they are emitted when the electron beam removes an inner shell electron from the specimen, causing a higher energy electron to fill the shell and release energy. Those radiations can be used for elemental analysis such as the composition and distribution of individual elements within the sample. The interaction volume between the electron beam and the specimen with the various electrons emitted and their respective

energies is shown in Figure 2.4.

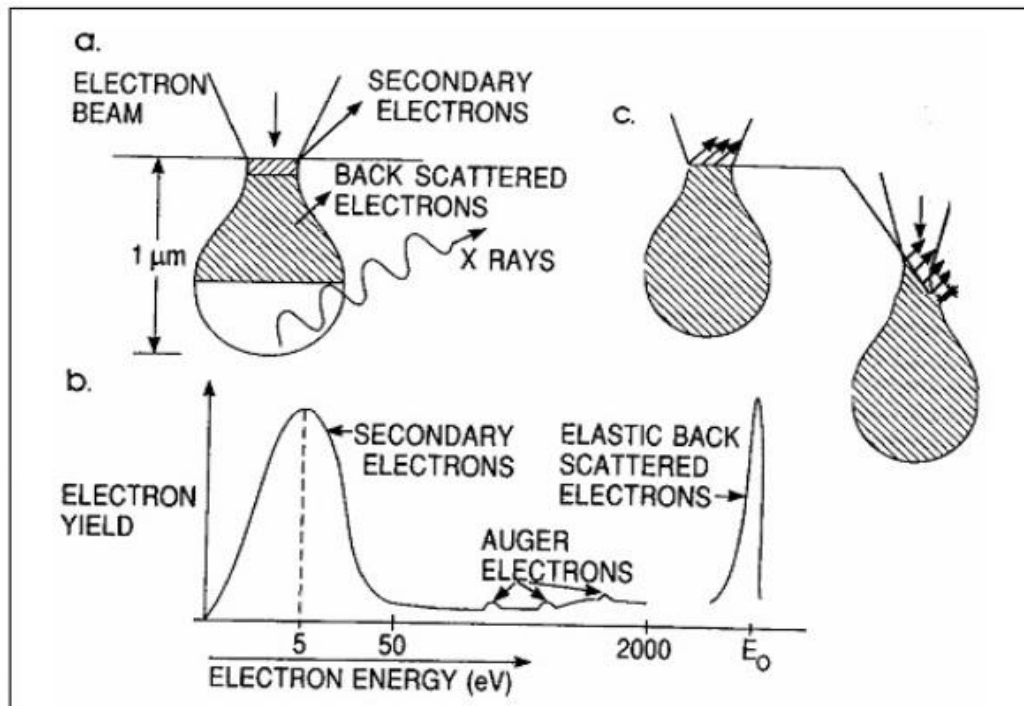


Fig. 2.4 (a) Electron interactions with the surface during bombardment. (b) Type of electrons and corresponding energies of the emitted electrons after element interaction. (c) Effect of surface topography on electron emission. [36]

The Scanning Electron Microscope that was used to study our samples is the Tescan MIRA3. It is a high performance SEM system that achieves high resolution and low-noise imaging, and is characterized by an ultra-fast scanning system.

The detection of the secondary electrons was done using the In-Beam detector, located in the objective lens, rather than using the SE detector which does not function well at a short working distances (WD). However, the advantage of the In-Beam detector is that it allows

imaging at a very short working distances (WD), allowing the achievement of better images resolution, and it enables the observation of extraordinary sharp surface details and highlights the topography clearly.

a. SEM of ZnO NWs

The manipulated parameters in each sample impacted the morphology and growth of ZnO nanowires to a varying degree. Hence, it is imperative to analyze the synthesis results to determine the best process that yields a high quality and repeatable ZnO nanowires.

As mentioned previously, we focused specifically on varying the following parameters: the concentration of Zinc Acetate, the duration of dip-coating process and the temperature of the mixed solution.

Therefore, two different durations of dip-coating processes were tested at a fixed concentration of Zinc Acetate 0.025 M and a fixed temperature 87⁰C, and it was found that consistent nanowire growth occurred when keeping the Zinc Oxide seed layer immersed in the mixed solution of Zinc Acetate, ammonium hydroxide and water, for 60 min and more.

The SEM image in FIG. 2.5 (a) shows absence of consistent morphology of ZnO nanowires and unstable growth that seems to be hindered due to the insufficient thermodynamic activation of the growth nucleus, which is attributed to the short period of dip-coating process that lasted 15 min.

While in FIG. 2.5 (b), for which the dip-coating process was maintained for 90 min, the SEM image shows well defined ZnO nanowires with a high degree of vertical alignment to the Si substrate. It is also observed in FIG. 2.6 (a) and (b), that the average diameter for each process increased when increasing the time of the dip-coating process.

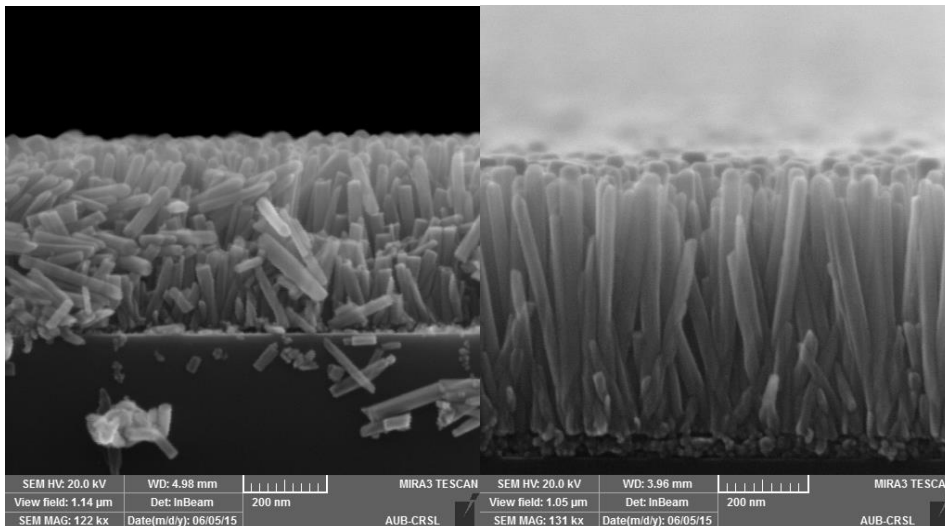


Fig. 2.5 (a) and (b) respectively. SEM images of ZnO nanowires prepared at a dip-coating process durations that exceed 60 min, while fixing the concentration of the Zinc Acetate 0.025 M and the temperature of the mixed solution at 87⁰C.

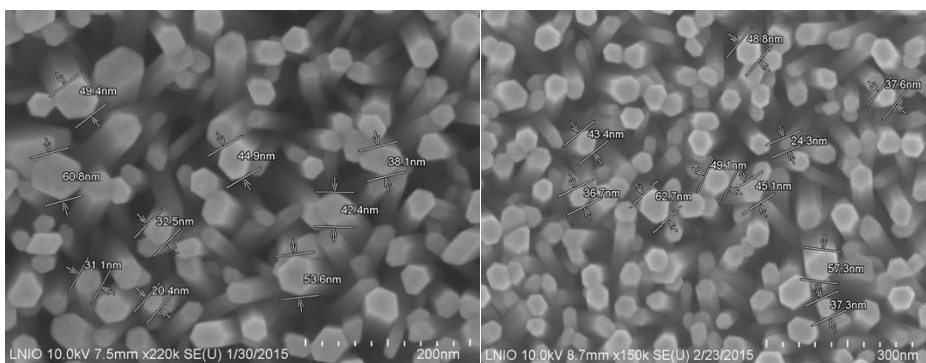


Fig. 2.6 (a) and (b) respectively. SEM images in top view showing the diameters of ZnO nanowires prepared at a dip-coating process durations that exceed 60 min, while fixing the concentration of the Zinc Acetate 0.025 M and the temperature of the mixed solution at 87⁰C.

It was also shown that the growth of well aligned ZnO nanowires can be controlled by varying the concentration of the Zinc Acetate solution. Therefore 3 different concentrations varying between 0.023 M and 0.03 were tested, and each one was accompanied by a different

duration of the dip-coating process, while fixing the temperature. It was found that the largest concentration of Zinc Acetate 0.03 M yielded the best nanowires quality, with a high degree of vertical alignment and a uniform size and shape within the same sample (FIG. 2.7).

The average diameter size was found to increase from 25 nm to 95 nm when increasing the Zinc Acetate concentration from 0.023 M to 0.03 M (FIG. 2.8).

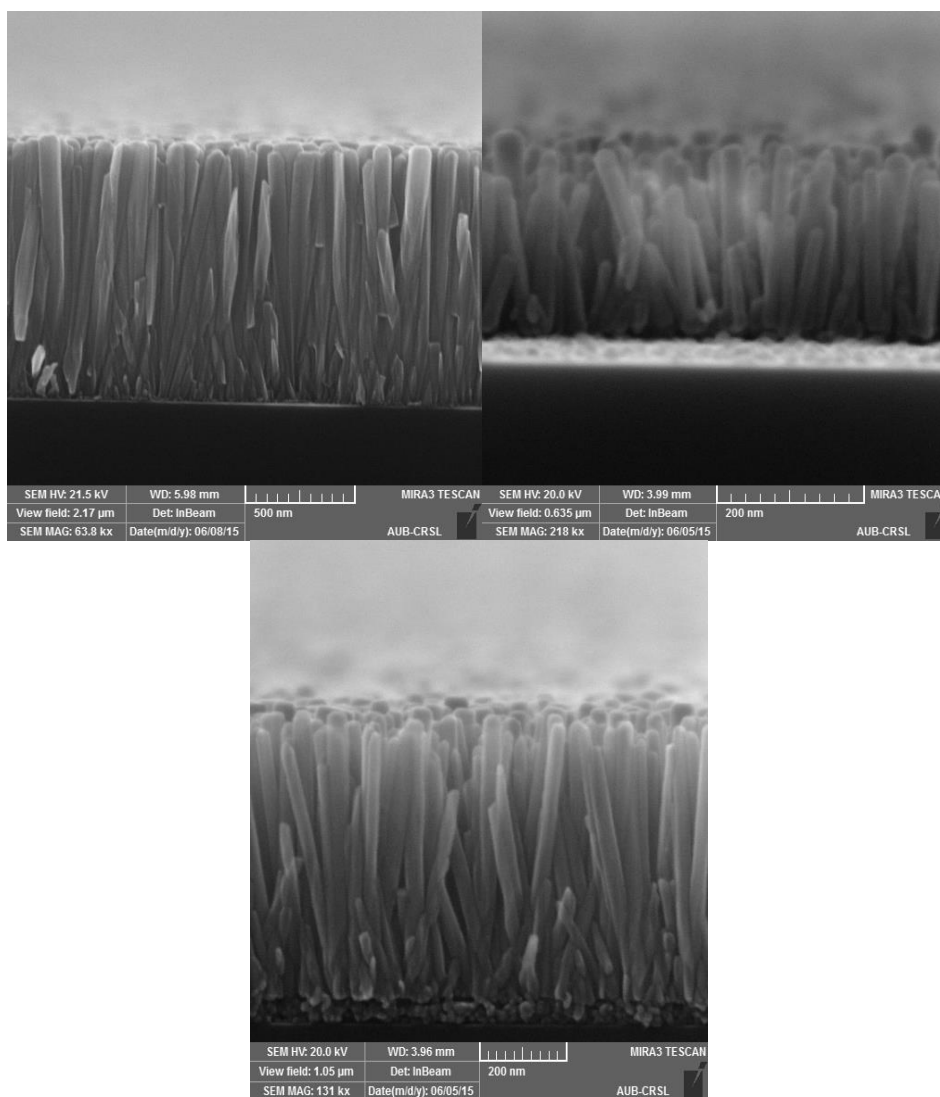


Fig. 2.7 (a), (b), and (c) respectively. SEM images of ZnO nanowires prepared with varying Zinc Acetate concentration: (a) 0.023 M, (b) 0.025 M, (c) 0.03 M and a varying dip-coating process durations, while fixing the temperature of the mixed solution at 87⁰C.

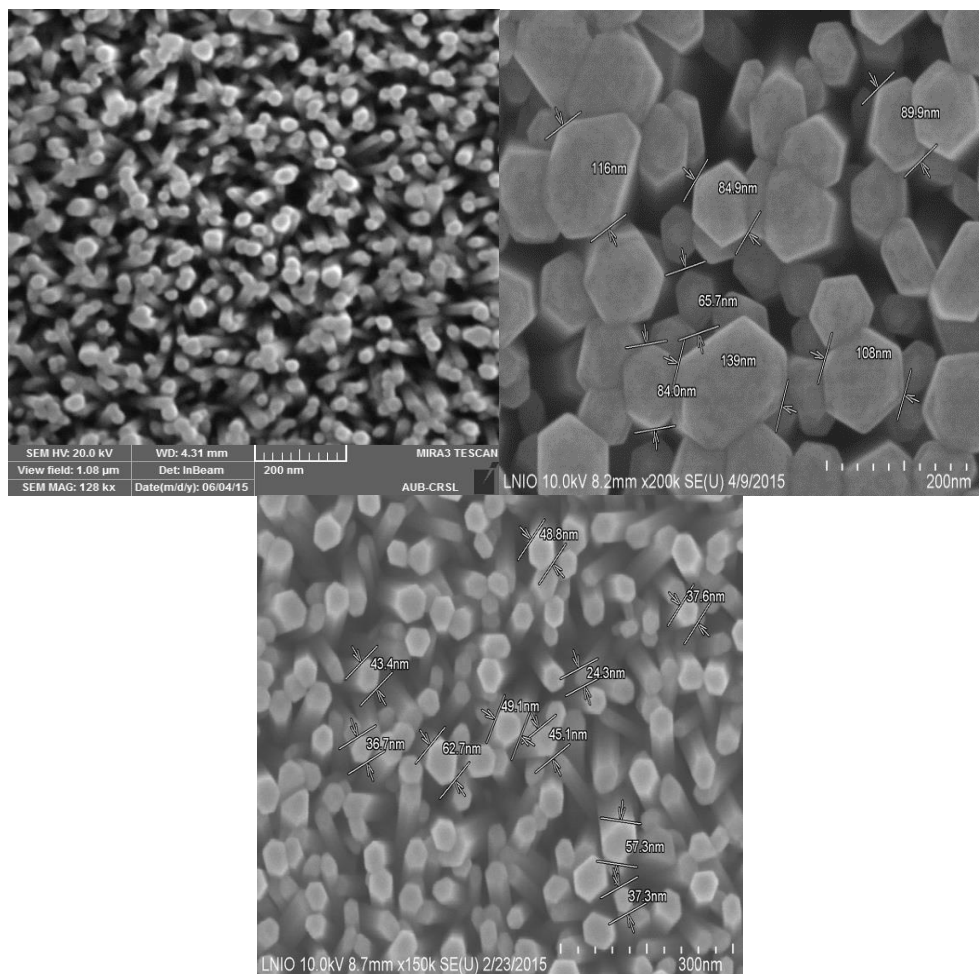


Fig. 2.8 (a), (b) and (c) respectively. SEM images in top view showing the diameters of ZnO nanowires prepared with varying Zinc Acetate concentration: (a) 0.023 M, (b) 0.025 M, (c) 0.03 M and a varying dip-coating process durations, while fixing the temperature of the mixed solution at 87⁰C.

In conclusion and based on the SEM results, we found for concentrations of Zinc Acetate between 0.025 M and 0.023 M and for a dip-coating process that exceed the 60 min period, we obtained the best nanowires quality, with a high degree of vertical alignment and a uniform size and shape. We also observed that the diameter of the nanowires could be tuned by varying either the concentration of the Zinc Acetate solution or the duration of the immersing process.

b .SEM of Silicon Resonators Arrays

Similarly, to the ZnO NWs, the primary aim was to test how manipulating the growth conditions would affect the silicon resonators arrays, whether in terms of size or morphology. Noting that those samples were synthesized using a combination of both, the Interference Lithography and the Reaction Etching techniques.

These growth conditions include the following manipulated parameters: the etching time, the Power of the laser beam, and the temperature of the SF₆/O₂ gas mixture under which etching was performed. Whereas, everything else was fixed.

The formation mechanism for the resonators, initially started by fixing: the pressure of the mixed gases SF₆/ O₂ at 4 mTorr, the power of the laser beam at 90 W and the etching time at t = 5 min. Whereas the variable in this first procedure is the temperature of the mixed gases which varied from 5⁰C up to 30⁰C.

It can be observed in **FIG. 2.9** below, that with each temperature increase, the tip diameter of the silicon resonators arrays increased as well. While the bottom diameter of the silicon arrays showed a decremental tendency in response to that temperature rise. As for the height of the silicon nanocones, it showed a consistency and remained almost the same for temperatures varying between 5⁰C and 15⁰C, whereas it got smaller and underwent a sudden shortening when the temperature was increased up to 30⁰C.

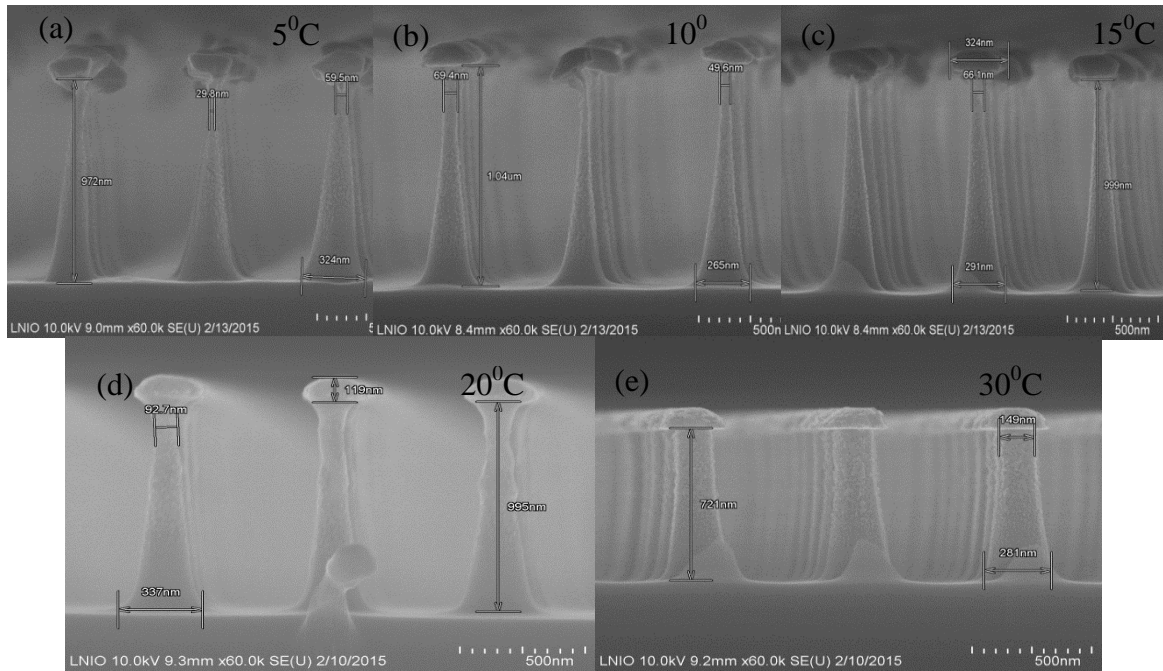


FIG. 2.9 Reporting results on the synthesis of Silicon resonators arrays that were fabricated using a combination of Interference Lithography and Reaction Etching. (a) Diameter of the tip: 30-60 nm; Diameter of the bottom: 324 nm; Height: 972 nm. (b) Diameter of the tip: 50-70 nm; Diameter of the bottom: 265 nm; Height: 1 μ m. (c) Diameter of the tip: 70 nm; Diameter of the bottom: 290 nm; Height: 1 μ m. (d) Diameter of the tip: 97 nm; Diameter of the bottom: 337 nm; Height: 992 nm; (e) Diameter of the tip: 149 nm; Diameter of the bottom: 281 nm; Height: 727 nm.

In another set of SEM images related to the structures discussed previously, it can be seen in FIG. 2.10 below, that the arrays of silicon resonators display a high degree of vertical alignment and a periodicity in spacing. In addition, the SEM images clearly show how the tip of the resonators vary when the growth processes parameters are altered, giving formation to resonators in the form of nanocones and pillars.

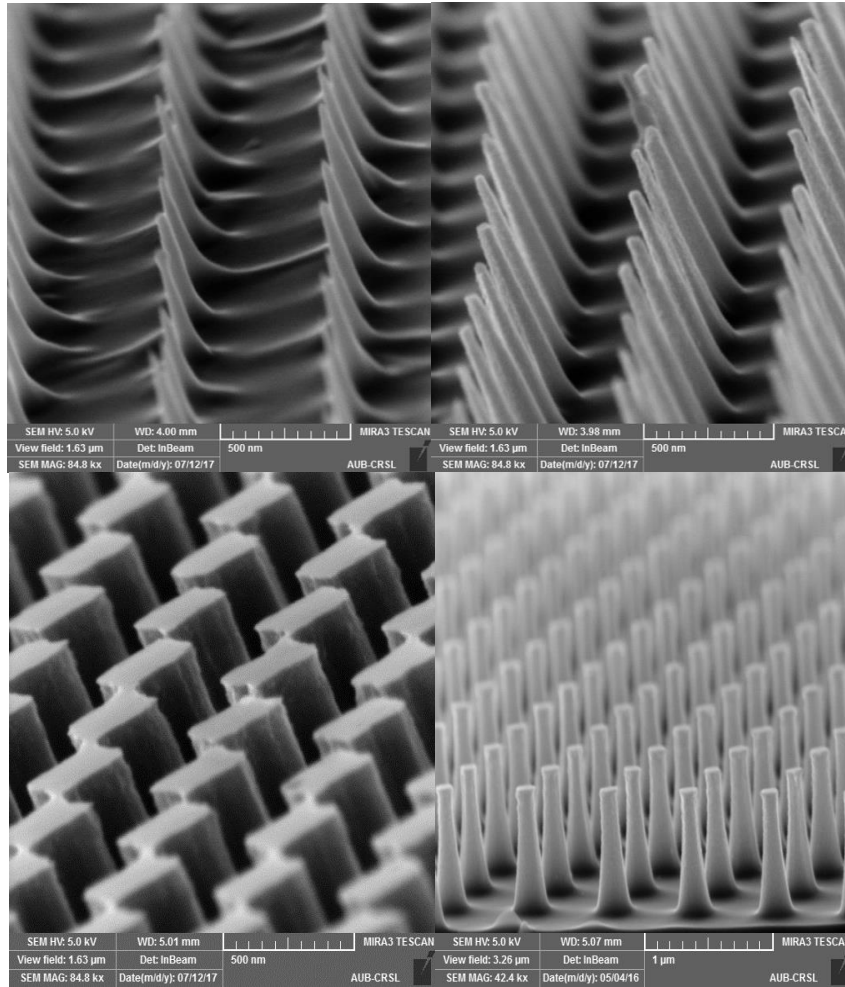


FIG. 2.10 Scanning Electron Micrograph SEM of periodic silicon resonators arrays displaying multiple shapes that vary from nanocones-like to truncated cones and to pillar-like structures.

Moving on to another set of samples, in which the varied parameters are the laser beam's power and the etching time, while the temperature is maintained at 15 °C for both samples.

Regarding the first sample of this set (see FIG. 2.11 below), for which the laser power increased up to 200 W, it can be observed that the tip and the bottom diameters are almost identical and much larger than those of the structures discussed previously, despite that the

etching process lasted only for 2 minutes, and thus giving formation to pillar-like silicon resonators arrays.

As for the second sample of this set, for which the etching time is upped to 5 min, the tip diameter exhibited a tremendous drop in comparison to the first sample, while the bottom diameter decremented by a relatively reasonable amount, and therefore giving formation to silicon nanocones arrays.

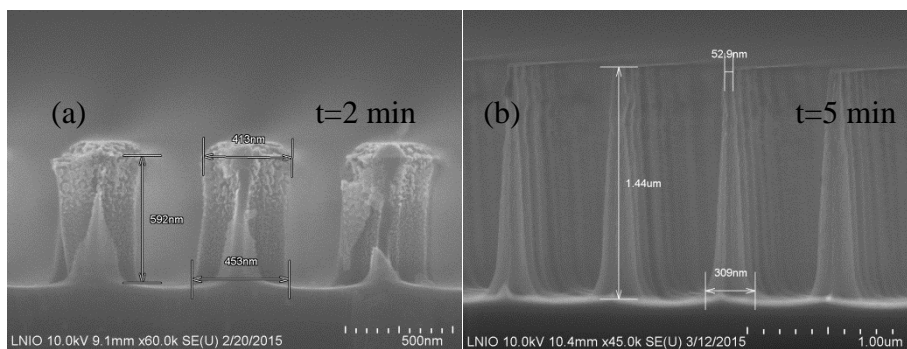


FIG. 2.11 Reporting results on the synthesis of Silicon resonators arrays that were fabricated using a combination of Interference Lithography and Reaction Etching.

(a) Diameter of the tip: 413 nm; Diameter of the bottom: 453 nm; Height: 592 nm.

(b) Diameter of the tip: 53 nm; Diameter of the bottom: 309 nm; Height: 1.44 μm.

2. X-Ray Diffraction (XRD)

X-Ray diffraction is a rapid analytical technique used for characterization and phase identification of a crystalline material. It determines the exact positions, structures and other structural parameters such as average grain size and crystal defects of atoms in a crystal, by striking a beam of X-Ray on the crystal which causes a beam of light to diffract into many directions.

This non-destructive analytical technique is based on constructive interference of a monochromatic beam of X-Rays scattered at specific angles from the different set of lattice structures in a specimen.

Therefore, the result is a graph of the the intensity of diffracted beams making an angle of 2θ with the incident beam.

a. Basic Theory of X-Ray Diffraction

X-Rays are a form of electromagnetic radiation of shorter wavelength but high energy than normal light. They are produced when electrons strike a metal target, in particular when the electrons collide with the atoms and the nuclei of the metal target.

These X-Rays are generated in a highly evacuated glass bulbs, referred to as X-Ray tube, that consists of two electrodes: a cathode which provides a source of electron and an anode made of platinum, tungsten or another heavy metal of high melting point, and which acts as the target for electrons and releases X-Rays.

Two separate processes can be distinguished which would give rise to X-Rays radiation. In one process, accelerating electrons emitted from the cathode with a high voltage, undergo sudden stopping, braking or slowing of their high speed upon collision with the target, followed by an X-Ray emission. These X-Rays are called “Braking radiation” (Bremsstrahlung).

In the second process, high energy electrons emitted from the cathode expel an electron out of the inner shell of the bombarded atom. An electron from a higher energy level will then drop down to fill the vacancy emitting X-Rays with precise energies determined by the electron energy levels.

These X-Rays are known as “*Characteristic X-Rays*”.

b. Bragg's Law

Bragg diffraction occurs when two X-Ray beams, with identical wavelength that is similar to the atomic separation and in phase, strike on two parallel lattice planes of a crystalline solid. Then the scattered waves off the two planes interfere constructively and remain in phase in accordance with the Bragg Law. (A schematic illustration of the requirements of Bragg's law is shown in (FIG. 2.12). This is described by the following relation:

$$2d\sin\theta = n\lambda$$

Where:

- d is the lattice or inter-planar spacing.
- θ is the angle between the incident ray and the lattice plane (scattering angle).
- λ is the wavelength of the incident wave.
- n is a positive integer.

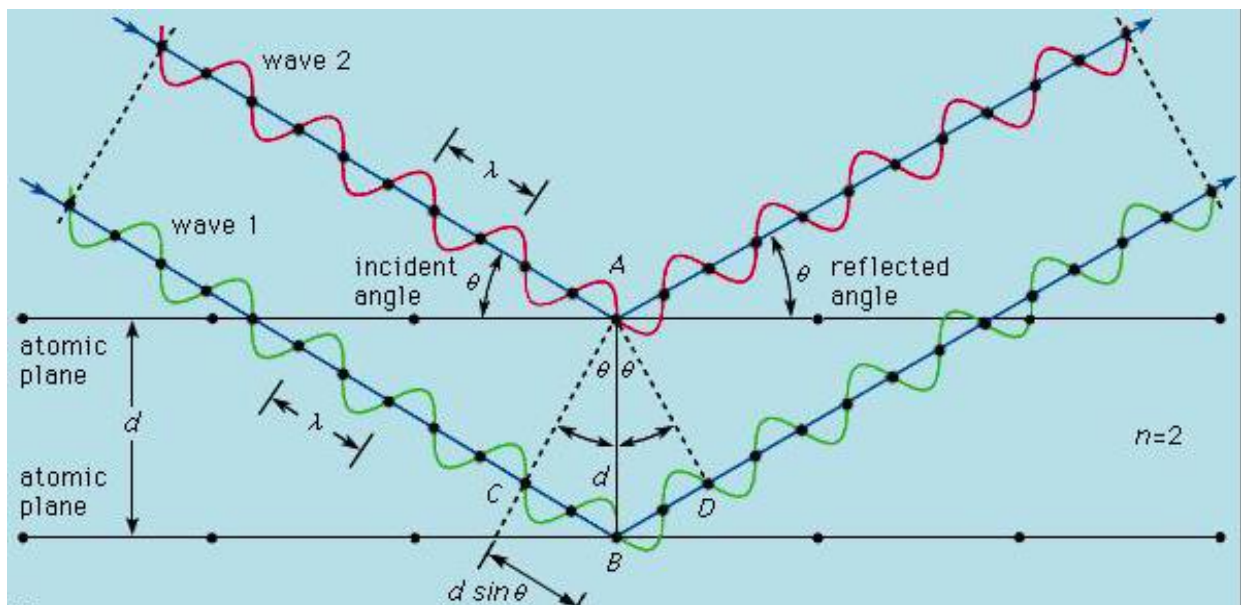


Fig. 2.12 Schematic of Bragg's Law condition [54]

c. X-Ray Diffractometer

The X-Ray diffractometer that was used to study the structure of the samples and their chemical composition is the D8 ADVANCED X-Ray diffractometer. This model is equipped with stepper motors with optical encoder to ensure extremely precise angular values.

The D8 X-Ray diffractometer consists of three basic elements: An X-Ray tube, a sample holder and an x-Ray detector.

For the XRD analysis, the sample is first placed on the sample holder, then X-Rays are generated in the cathode ray tube by heating a filament to produce electrons. Afterwards, an applied voltage would accelerate the electrons which are then collimated and directed at an angle θ towards the sample to bombard it.

After constructive interference occurs, signifying an accordance of the incident X-Rays with Bragg's Law, a peak in the intensity of the reflected X-Rays takes place which is recorded by a detector located on the opposite side at an angle 2θ .

The sample and the detector will keep rotating in the path of the collimated X-Ray beam, while recording all the intensities of the reflected X-Rays, and a diffraction pattern is formed that includes the intensity peaks.

A detector records those X-Ray signals and converts them to a count rate which is then displayed on the computer monitor as a function of the detector angle 2θ .

A schematic of the basic components of the diffractometer is shown in the figure below (FIG. 2.13).

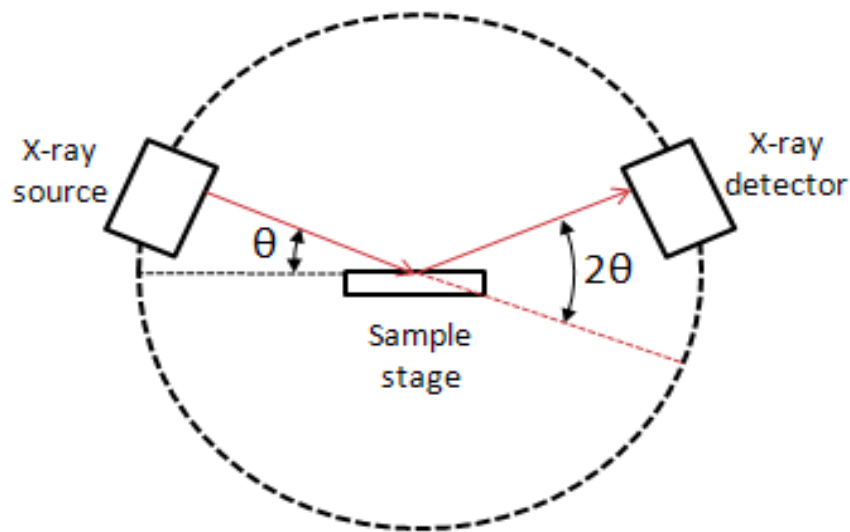


FIG. 2.13 A simple representation of an X-Ray diffractometer.

d. XRD Measurements of Zinc Oxide Nanowires

The X-Ray diffraction patterns shown in the figures below correspond to all the samples prepared by using the chemical bath deposition technique. In these, ZnO nanowires were grown on a silicon substrate at different conditions of solution concentration, preparation time and thermal treatments.

The first figure displayed below (FIG. 2.14), which corresponds to that of the Silicon substrate, is well indexed to the p-type (100) surface oriented Si wafers structure. There are no additional diffraction peaks observed that might correspond to impurities.

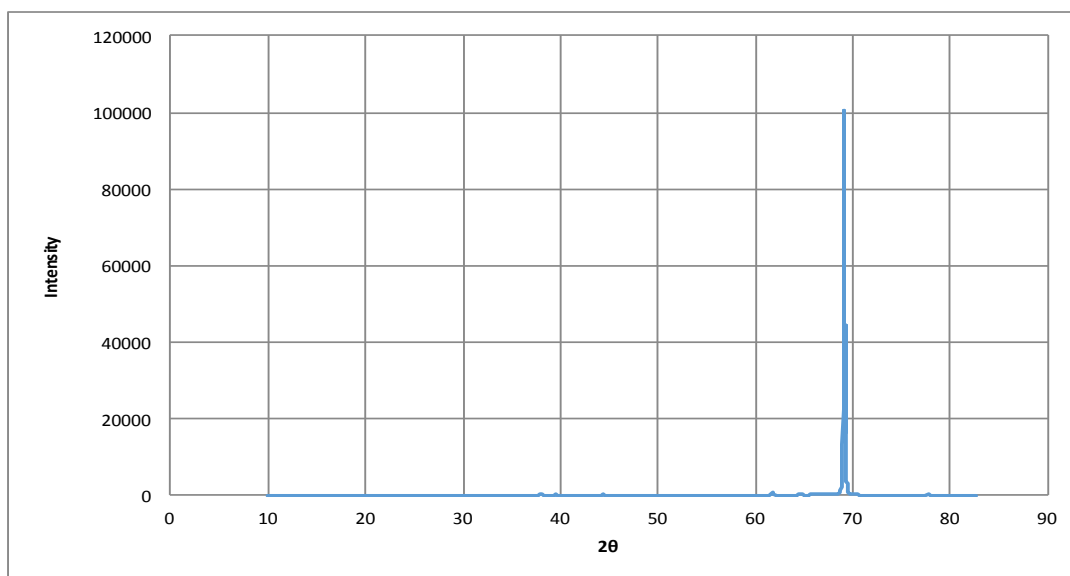


FIG. 2.14 XRD of undoped p-type (100) Si substrates which were cleaned with ethanol and de-ionized water.

As for the other spectra, they correspond to ZnO nanowires grown on the silicon substrate by varying the temperature of the heated mixed solution, the Zinc Acetate concentration and the duration of the dip-coating process, respectively. All of the peaks that were obtained in the XRD patterns can be indexed to the hexagonal ZnO wurtzite structure.

However, a characteristic peak corresponding to Si is detected, this is because the ZnO nanowires are grown on the Si substrate.

Regarding the parameters by which the growth process of the ZnO is manipulated, we noticed that when increasing the Zinc Acetate concentration from 0.023 M to 0.025 M, the intensity of the characteristic peaks almost doubled up, while fixing the temperature at 87⁰C and decreasing the dip-coating process duration to half.

Then, when fixing the concentration of Zinc Acetate and the temperature, while increasing the dip-coating process from 15 min to 90 min, the intensity of the characteristic peaks elevated dramatically.

Finally, when keeping the concentration of Zinc Acetate constant, while reducing the the duration of dip-coating process and the temperature by a small margin, the intensity of the peaks remained almost stable.

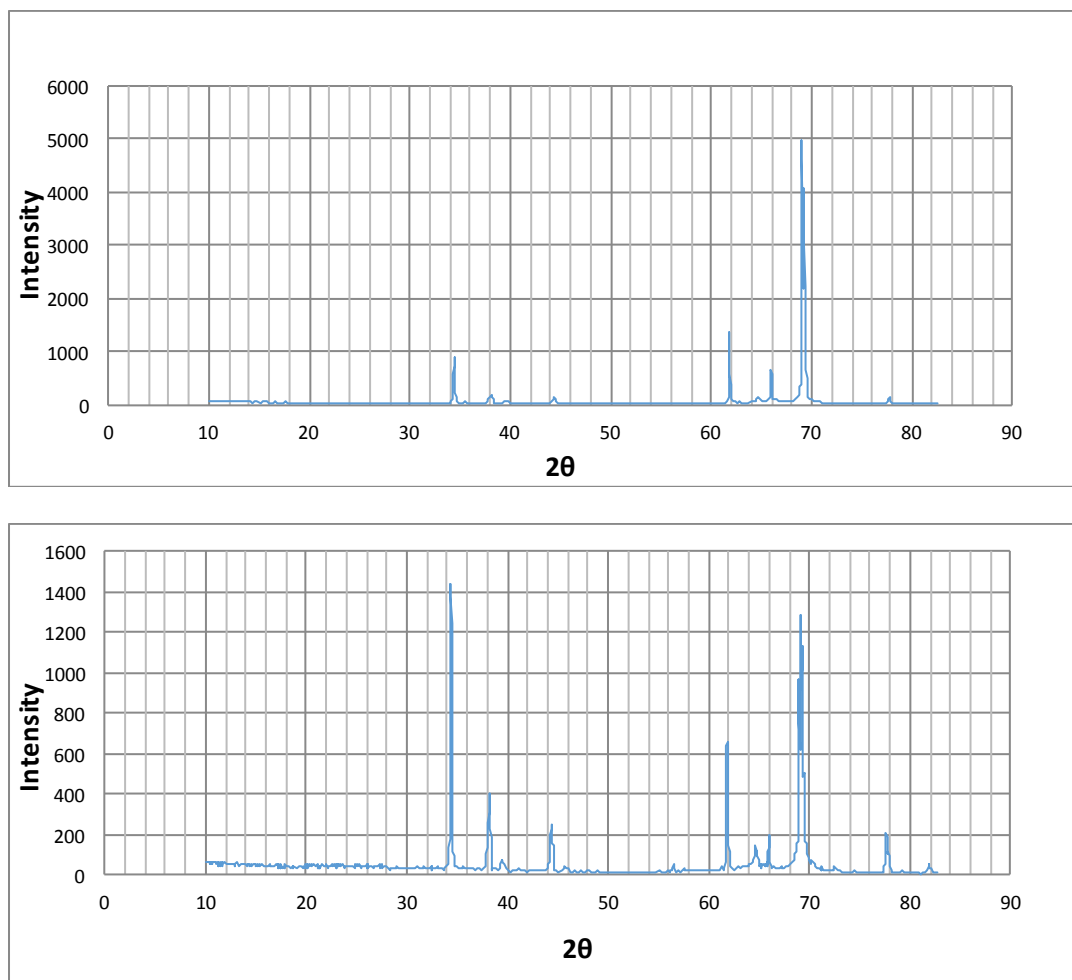


FIG. 2.15 XRD of ZnO nanowires samples prepared by varying the concentration of Zinc Acetate and the duration of dip-coating process while fixing the temperature of the mixed solution.

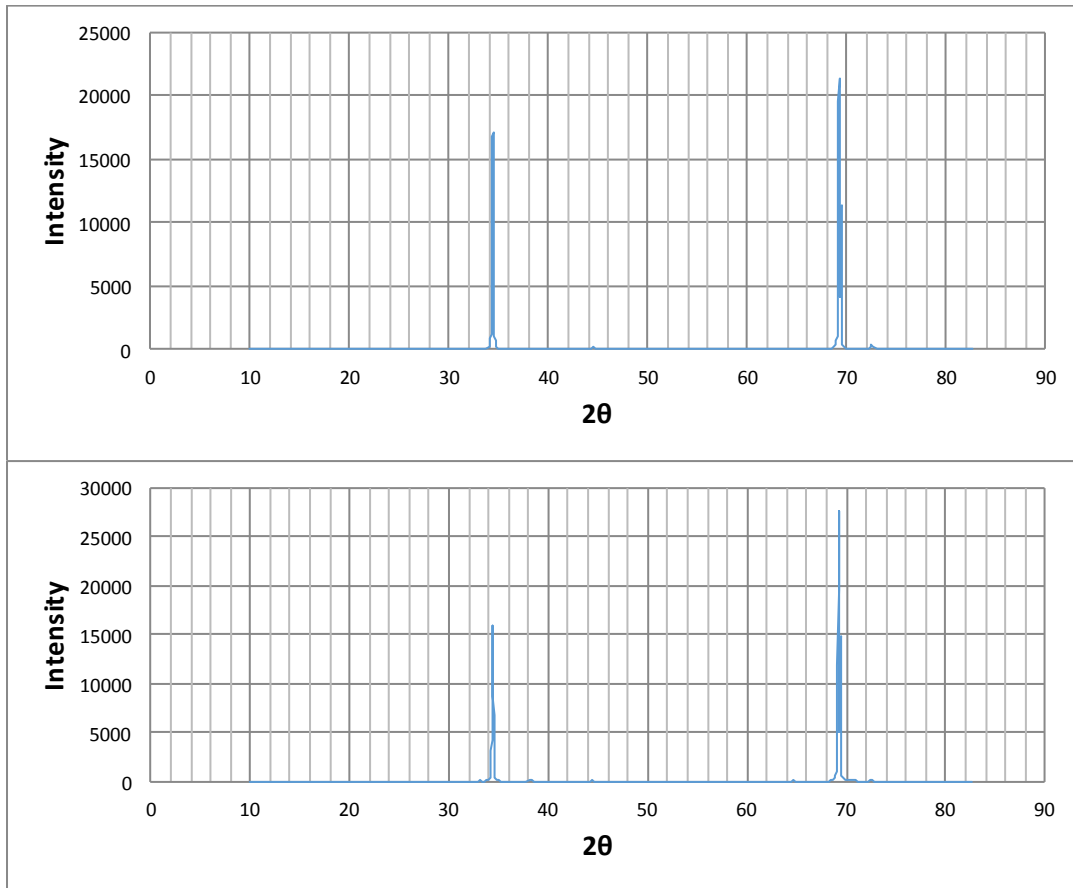


FIG. 2.16 XRD of ZnO nanowires samples prepared by varying the duration of dip-coating process and the temperature of the mixed solution while fixing the concentration of Zinc Acetate.

e. XRD Measurements of a bare Si substrate and of Si resonators of different sizes and shape

The X-ray diffraction XRD patterns, shown in the figure below, correspond to different Si resonators arranged on a bare Si substrate. The observed peaks are well indexed to Si crystallographic phase. No extra peaks related to any impurity are observed, which confirms that the as-grown resonators are pure Silicon structures.

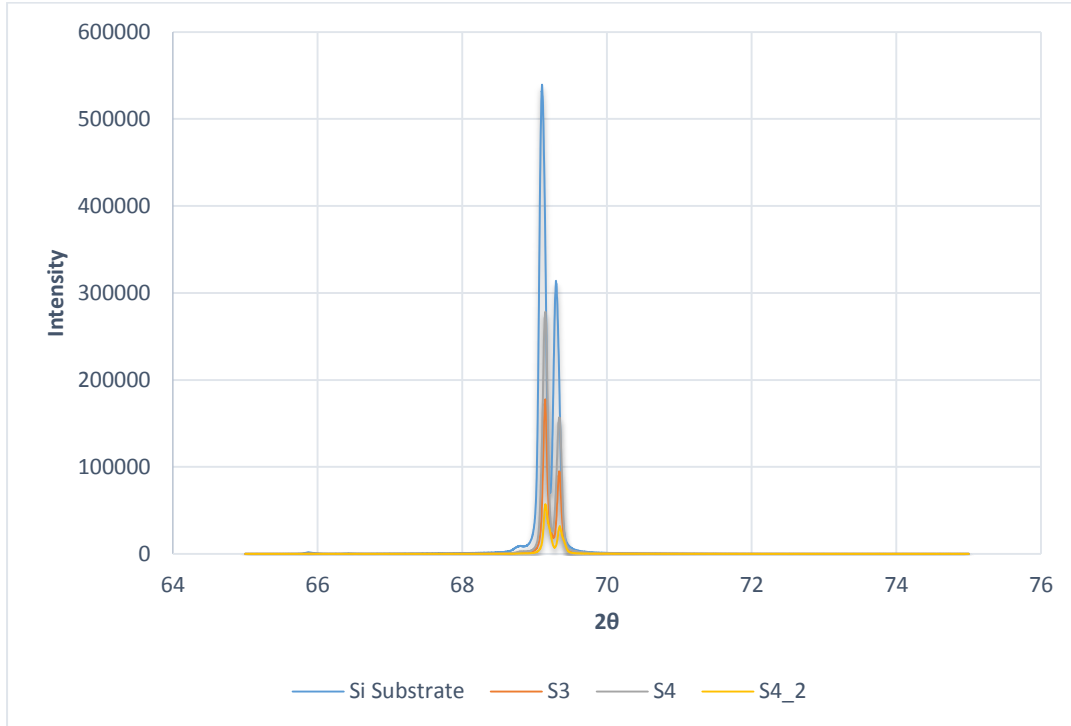


FIG. 2.17 XRD patterns of a bare Si substrate and of Si resonators of different sizes and shape arranged on the latter.

However, it is obvious that the diffraction patterns exhibited a broadening in peaks' width and an increase in peaks' intensity. These observed changes in patterns arise mainly due to two factors: crystallite size and lattice strain, since the crystallite size and lattice strain affect Bragg peak by increasing the peak width and intensity and shift the 2θ peak position accordingly [37]. In other words, a size reduction in the crystallites in addition to the crystallographic defects, would account for a wider and more enhanced XRD peak.

For that purpose, in order to estimate the crystallite size of Si resonators, Scherrer equation is used.

The Scherrer equation relates the peak broadening represented by the full width at half maximum in radian (β_{FWHM}) to the average grain size of a sample as [38] :

$$d = \frac{K\lambda}{\beta \cos\theta_{\beta}}$$

Where, d is the coherent scattering length (crystallite size), θ_{β} is the Bragg angle, and K is a constant that depends on both apparatus and the sample studied, and it is usually taken to $K = 0.9$. While the X-ray wavelength is taken to be: $\lambda = 0.154 \text{ nm}$.

The bare Si substrate and the Si resonators' crystallites sizes results are illustrated in the table below:

Table. Calculated crystallite sizes derived from Scherrer equation

Samples	Si Substrate	S3	S4	S4_2
Angle	69.112	69.146	69.144	69.15
Crystallite Size	96.4 nm	142 nm	115 nm	107 nm

3. Raman Spectroscopy

Raman Spectroscopy is a powerful optical spectroscopic technique that can examine the vibrational energy levels of molecules in various fields, and it is based on the inelastic scattering of light during light-matter interactions.

This technique allows one to extract detailed and specific information on a molecular level that other laser or electronic spectroscopic methods would provide to a limited extent.

Of all the various systems that can be investigated by Raman Spectroscopy, we distinguish the following: chemical identity, reactivity, diffusion, charge states, phenomenology at interfaces, in addition to the mechanical and electrical stress and the influence of electric fields on molecular properties.

Raman spectroscopy is as well a noninvasive and nondestructive imaging technique and requires minimal or no sample preparation.

a. Basic Theory of Raman Spectroscopy

The ground breaking work of Sir Chandrasekhara Venkata Raman (C.V. Raman) in the field of light scattering, started out in 1922 when he published his work on the “Molecular Diffraction of Light” the first part of a series of studies with his collaborators which eventually led to his discovery, on the 28th of February 1928, of the inelastic scattering of light and its effects which gained him the 1930 Nobel Prize in Physics.

The process starts with an electromagnetic radiation striking on a molecule and interacting with the cloud of electrons around the nucleus of the molecule causing them to distort/polarize and to form a transient and unstable energy state called the virtual energy level.

During this light-matter interaction, a very tiny fraction of photons collides with the heavier nucleus of the molecule which is initially in either the ground rovibronic state (lowest rotational and vibrational energy level of the ground state) or in an excited rovibronic state, and this interaction results in an energy exchange between the photon and the molecule, causing a change in the energy and in the frequency of the scattered light, and therefore resulting in an inelastically scattered photon. Hence the Raman Spectroscopy process.

In Raman Spectroscopy, the vibrational frequency (ν_m) of a molecule is measured as a shift from the incident beam frequency (ν_0). Thus, in Raman Scattering, if the energy is transferred from the incident photon to the molecule (which is the case often times, because

at room temperature most of the molecules occupy the ground vibrational state), then the molecule is excited to higher energy state and the photon is scattered with a red-shifted frequency, $\nu_0 - \nu_m$, and is referred to as “Stokes shift”. (See FIG. 2.18)

However, if the molecule is in a higher excited energy level, it will transfer its energy to the scattered photon and falls back to the ground level, and the output is then characterized by a blue shifted frequency, $\nu_0 + \nu_m$, and is referred to as “anti-Stokes shift”. (See FIG. 2.18)

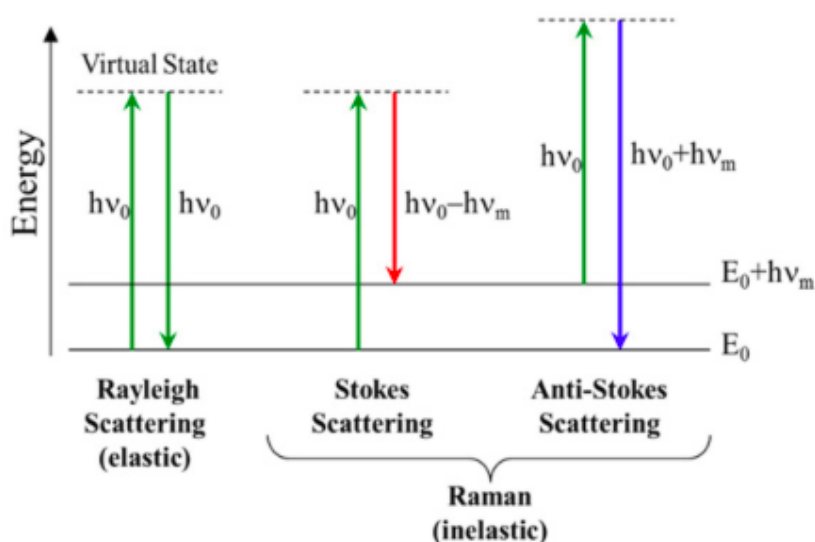


FIG. 2.18 Schematic representing the three different forms of scattering.

Nevertheless, Raman Scattering should not be confused with fluorescence, because in the latter an incident photon is completely absorbed by the molecule which causes it to move to a higher electronic energy state. Later on, this photon of energy is emitted, and the molecule returns to a lower energy state, while in the case of Raman Scattering, the photon is emitted instantaneously.

On the other hand, the majority of the incident photons are scattered off by the electron cloud without any loss of energy, during the light-matter interaction, and therefore there is no change in frequency, since the electrons are comparatively light.

The scattering is elastic in this case and this is known as Rayleigh Scattering. (See FIG. 2.18)

The total distribution of the molecules in any energy level is given by the Maxwell-Boltzmann equation:

$$\frac{N_n}{N_m} = \frac{g_n}{g_m} e^{-\frac{(E_n - E_m)}{KT}} \quad (2-1)$$

Where:

- K is the Boltzmann's constant ($1.3897 \cdot 10^{-23} \text{ JK}^{-1}$)
- T is the given temperature.
- N_n is the number of molecules in the excited vibrational energy level n.
- N_m is the number of molecules in the ground vibrational energy level m.
- $g_{n/m}$ is the degeneracy of the levels in n and m.
- $E_n - E_m$ is the energy difference between the vibrational energy levels.

As for Raman Scattering, this phenomenon can be interpreted according to the classical theory as follows: the electric field (E) of the electromagnetic wave (laser beam) fluctuates with time (t) as will be described here:

$$E = E_0 \cos(2\pi\nu_0 t) \quad (2-2)$$

Where:

- E_0 : Vibrational amplitude.
- ν_0 : Frequency of the laser.

When this laser light is incident on a molecule, then an electric dipole moment P is induced:

$$P = \alpha E = \alpha E_0 \cos(2\pi\nu_0 t) \quad (2-3)$$

Where α is the Proportionality constant, and is called polarizability of the material which depends on the molecular structure and the nature of the bonds.

If the molecule is vibrating with a frequency ν_m , the physical displacement of the atom about their equilibrium position is expressed as:

$$q = q_0 \cos(2\pi\nu_m t) \quad (2-4)$$

Where q_0 is the vibrational amplitude.

For a small amplitude of vibration, the polarizability α is a linear function of q , and can be approximated using a Taylor series expansion:

$$\alpha = \alpha_0 + \left(\frac{\partial\alpha}{\partial q}\right)_q q + \dots \quad (2-5)$$

Where

- α_0 is the polarizability at the equilibrium position.
- $\left(\frac{\partial\alpha}{\partial q}\right)_q$ Rate of change of α with respect to the change in q evaluated at equilibrium position.

Combining equations (2-3), (2-4) and (2-5), we obtain:

$$P = \alpha E_0 \cos(2\pi\nu_0 t)$$

$$P = \alpha_0 E_0 \cos(2\pi\nu_0 t) + \left(\frac{\partial\alpha}{\partial q}\right)_0 q E_0 \cos(2\pi\nu_0 t)$$

$$P = \alpha_0 E_0 \cos(2\pi\nu_0 t) + \left(\frac{\partial\alpha}{\partial q}\right)_0 q_0 E_0 \cos(2\pi\nu_0 t) \cos(2\pi\nu_m t)$$

$$P = \alpha_0 E_0 \cos(2\pi\nu_0 t) + \frac{1}{2} \left(\frac{\partial\alpha}{\partial q}\right)_0 q_0 E_0 [\cos(2\pi(\nu_0 + \nu_m)t) + \cos(2\pi(\nu_0 - \nu_m)t)] \quad (2-6)$$

The first term of this equation represents an oscillating dipole that radiates light of frequency ν_0 (Rayleigh Scattering)

The second term corresponds to the Raman Scattering of frequency $\nu_0 + \nu_m$ (Anti-Stokes), and $\nu_0 - \nu_m$ (Stokes).

- Note that if $(\frac{\partial \alpha}{\partial q})_0 \approx 0$, then the vibration is not Raman-active.

b. Experimental Setup

The Raman Spectroscopy instrumentation underwent several changes since its discovery in 1928, for it was based on a mercury lamp and a quartz spectrograph and it was limited for the spectroscopic study of scattered light only. Then various forms of mercury lamps followed and were implemented in 1930s and 1940s. It was not until the early 1960s that Raman spectroscopy became practically used due to the development of lasers, and therefore the requirement of light source monochromaticity was fulfilled.

Then in the late 1970s, Raman spectroscopy with optical microscope came to use, for microanalysis in many fields (Micro-Raman Spectroscopy).

The Raman spectroscopy system consists of a spectrograph with the following main components: an excitation source, a light detector and a light collection and delivery system.

The excitation source consists of a laser, while a Charged Coupled Device (CCD) camera is used for detection, and an optical microscope for light collection.

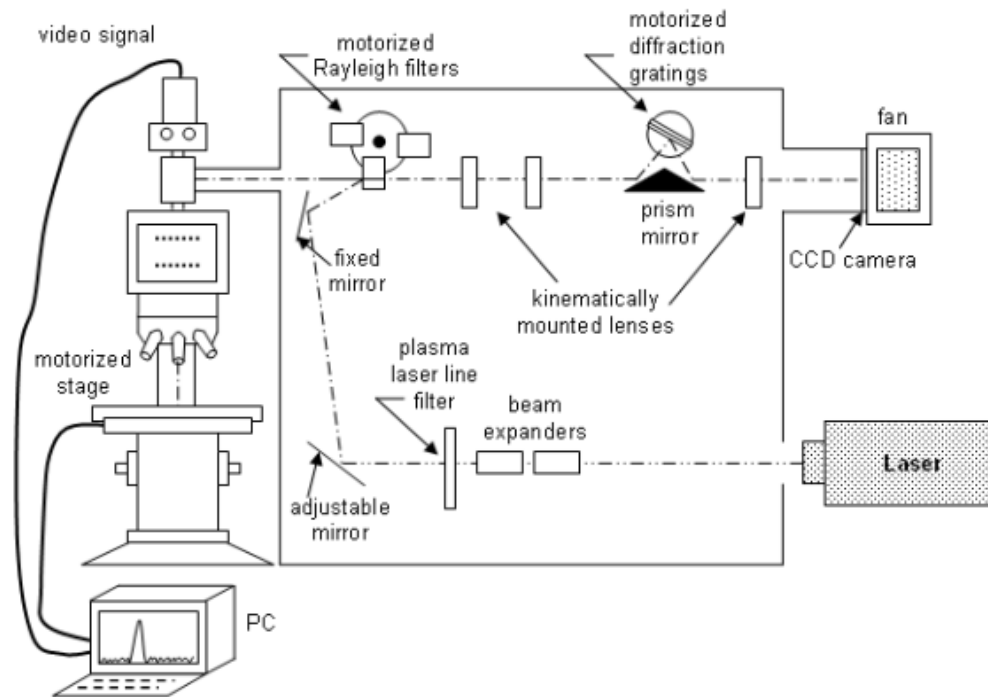


Fig. 2.19 Diagram of Raman Microscope System used for Raman spectroscopy and delivery.

Light Sources: a typical Raman laser consists of various characteristics, such as a narrow line-width in comparison to the width of the Raman lines in Raman spectrum which is around 1 to 10 cm^{-1} , a low power consumption, a stable power output, and a stable wavelength output. On average, power from the excitation source needed for Raman spectroscopy can range from about 3-10 mWs. Raman spectroscopy requires a monochromatic light source to achieve a good spectral resolution of acquired Raman spectra. The Raman scattering intensity is dependent on the laser power output. Therefore, increasing the laser power can be harmful to the sample in some cases.

Light Detector: This system consists of a slit, a diffraction grating, a mirror and a detector. Light illuminating the slit is narrowed by the latter as it enters the detection system

of the spectrometer so that it undergoes diffraction. Reducing the slit width increases the diffraction, and the former therefore acts as a source point. Afterwards, the diffracted light emerging from the slit travels to a collimating lens and then is directed onto a diffraction grating. The diffraction grating consists of a large number of equidistant, very fine, parallel and closely spaced slits that split the light into its constituent wavelengths. Depending on the number of the grating's slits and the spacing between them, as well as the angle at which the light is incident on the diffraction grating, only selected components of the light are directed towards the focusing lens. However, in order to have an extended scan and detect more center wavenumber, the grating is then not kept stationary but is rather adjusted to rotate, while the remaining light that is not directed towards the focus lens is collected by the detector. In that case, a baffle which is a mechanical system, whose function is to shield the light coming from sources outside the field of view, decreases the stray light in the system, while the shutter controls the detector exposure time.

The Raman signal is considered to be usually quite weak, therefore the micro-Raman Spectroscopy uses a CCD camera equipped with a cooling system, due to its inherent low noise features. Such cooling system can consist of a fan or liquid nitrogen system, depending on the needed requirements to achieve low noise

Rayleigh Filters: A Raman Spectroscopy system is equipped with a variety of optical filters used to prevent the undesired light that has the the same wavelength as the incident light (Rayleigh or elastic) from reaching the spectrometer and drowning out the relatively weak Raman signal, especially that the elastically scattered light intensity is about 10^7 times greater than the weak Raman signal.

Two basic types of filters are used: a notch filter and an edge filter. The notch filter blocks the Rayleigh scattered light while allowing both long and shorter wavelengths Raman scattered light to pass as close to it as 50 cm^{-1} on both sides of the Rayleigh line, therefore allowing the measurement of both Stokes and Anti-Stokes Raman scattering. As for the edge filter, it rejects the Rayleigh scattered light while allowing Raman scattered light to pass only on the Stokes shifted side of the Rayleigh line [39].

Objective Lenses: The objective lenses not only help focusing the laser beam but also locating a specific region in a sample, and they are characterized by a certain magnification and a numerical aperture. Therefore, when the laser of a specific wavelength is used as the excitation source for Raman micro-spectroscopy, in that case as the spot size on the sample due to the laser beam is reduced, the spatial resolution becomes higher and a diffraction pattern appears as shown in FIG. 2.20. The beam spot diameter depends on the laser's wavelength and the numerical aperture of the objective lens, and is calculated using the following equation:

$$\phi = 1.22\lambda \frac{\lambda}{N.A.}$$

With:

$d = \phi$: Is the spot diameter.

$N.A.$: Numerical Aperture of the objective lens.

λ : wavelength of the laser beam.

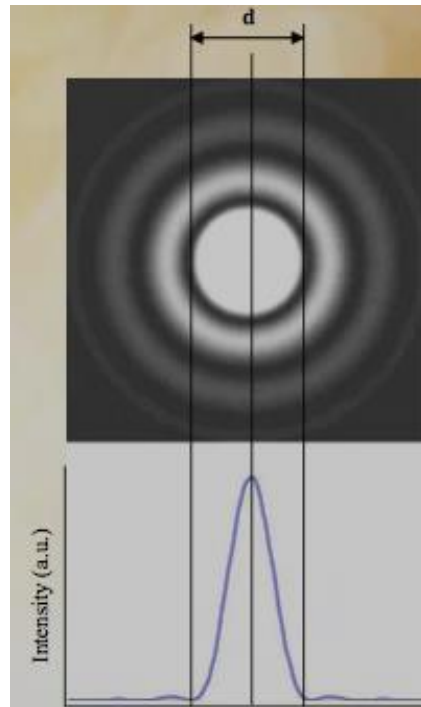


Fig. 2.20 Airy-disk resulting from diffraction with a circular aperture.

As for the diffraction pattern produced it corresponds to an Airy pattern, and the bright center area is called the “Airy-disk”. The size “ d ” of the bright center corresponds to the diameter of the laser beam spot on the sample, therefore d and \emptyset are different parameters representing the same quantity.

It should be noted that in order to achieve a high lateral resolution, it is desirable to have a small spot size. This can be done by using an objective lens with a high Numerical Aperture and a shorter wavelength.

4. Fourier Transform Infrared Reflectivity (FTIR)

a. Overview

Fourier Transform Infrared (FTIR) Spectrometer is a non-destructive vibrational spectroscopy technique that is used to identify organic and inorganic materials, and provides molecular information about a sample.

The main principal of this technique relies on the study of interactions between matter and electromagnetic fields in the Infrared region, where an infrared radiation is absorbed by a vibrating molecule causing it to move to a higher vibrational state, which are represented as peaks in the IR spectrum.

However, it should be noted that an infrared frequency would only be absorbed if its photon energy corresponds to the frequencies of the vibrational energy levels of the molecules making up the sample.

Therefore, infrared spectroscopy technique provides fingerprint information on the chemical composition of the sample, and the absorption properties can be extracted as well.

The FTIR Spectrometer holds some major advantages over other dispersive IR techniques, which include: extremely fast measurements and high detectors sensitivity.

FTIR spectrometer allows all frequencies to be measured simultaneously unlike the dispersive techniques where each frequency is measured individually by the detector. In addition, the detectors high sensitivity results in much lower noise levels.

b. Experimental Setup

The Zinc Oxide nanowires samples were analyzed using the Nicolet 4700 FTIR Spectrometer, from the Thermo Electron Corporation, in the mid-infrared region from 400 cm^{-1} to 4000 cm^{-1} , because the absorption of most organic compounds and inorganic ions is within this region.

The main components of this FTIR Spectrometer consist of an infrared source, an interferometer, a sample compartment, a detector, an amplifier, A/D convertor and a computer monitor where Fourier Transform is performed on the interferogram to obtain the spectrum.

FTIR Spectrometer relies on the technique of splitting then superimposing two or more waves, to detect the differences between them. Therefore, such instrument functionality is best depicted using the Michelson Interferometer which consists the core of the FTIR Spectrometer.

A schematic of the Michelson Interferometer is shown in the figure below (FIG. 2.21).

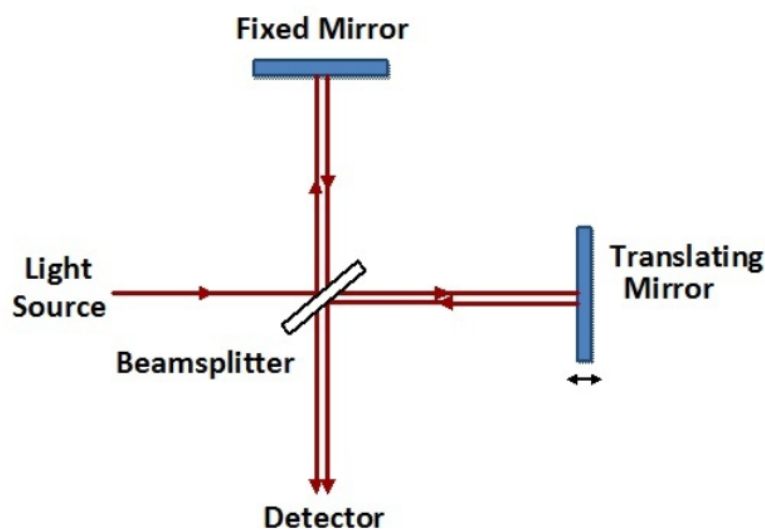


FIG. 2.21 Schematic illustration of Michelson interferometer [41].

The arrangement of Michelson Interferometer consists of two mirrors; a fixed and a movable one, a beam splitter and a single monochromatic light source. Light from the laser source strikes the beam splitter which is designed to split the incident beam into two parts: 50% of the radiation are being reflected to the fixed mirror, and the other half is being transmitted towards the movable mirror. Afterwards, the two split beams retrace their paths and recombine at the beam splitter producing a constructive and destructive interference pattern due to the optical path lengths difference between the two beams. In other words, an interferogram is formed on the viewing screen. The difference of the intensity of these two beams is measured as a function of the difference of the paths.

The ZnO nanowires samples will undergo diffuse reflection rather than specular one. Therefore, in order to minimize the specular reflection effect, a *Thermo Scientific Smart Diffuse Reflectance Accessory* is attached to the FTIR Spectrometer. This device maximizes the collection and the detection of diffusely scattered radiation, resulting in the highest quality spectral results. The Smart Diffuse Reflectance Accessory comes complete with two

sample slides: one holder that has an integral sample cup within it, which eliminates the need to worry about easily lost small parts, and the second holder has an integral gold mirror that can be used as a background reference.

This accessory operates by directing the infrared energy from the interferometer, into a sample cup filled with the solid powder. The infrared radiation then interacts with the particles causing the light to diffuse or scatter as it moves throughout the sample. The output mirror collects the diffusely scattered energy, which is directed to the detector in the spectrometer as shown in the figure below (FIG. 2.22).

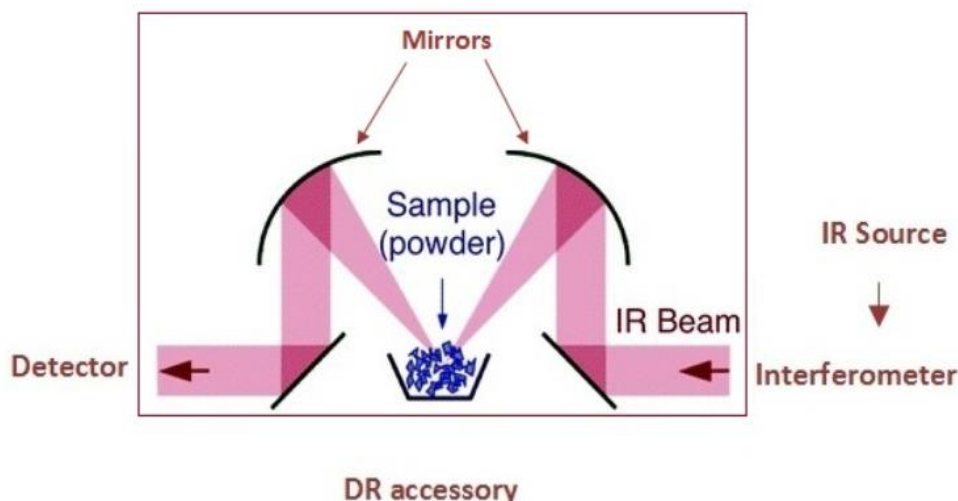


FIG.

2.22 Diffuse reflectance FTIR spectrometer. [42]

An interferogram signal is generated, that consists of all the recorded altered IR beams. Then using a computer monitor, Fourier Transform is performed on the interferogram to transform it into a frequency distribution spectrum (IR spectrum). The figure below shows the Fourier Transform of an interferogram signal into the frequency space (FIG. 11).

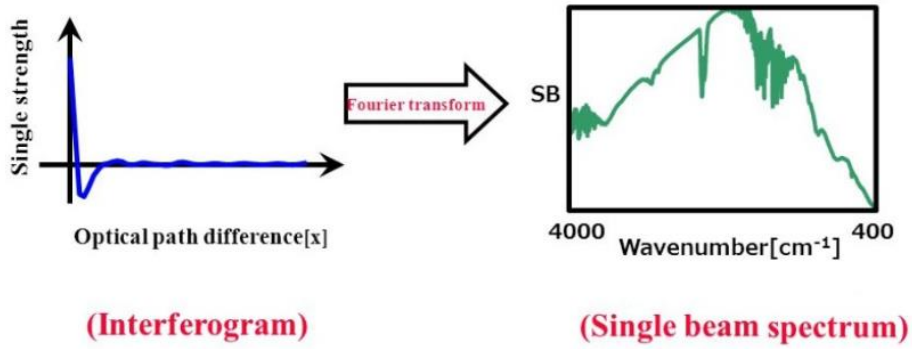


FIG. 2.23 Fourier Transform

Mathematically, the original interferogram function can be obtained by inverse Fourier transformation. Therefore, the mathematical expression of Fourier Transform can be expressed as:

$$F(w) = \int_{-\infty}^{+\infty} f(x) e^{iwx} dx$$

And the inverse Fourier Transform is:

$$f(x) = \frac{1}{2\pi} \int_{-\infty}^{+\infty} F(w) e^{-iwx} dw$$

Where:

- w is the angular frequency
- x is the optical path difference in our case.
- $F(w)$ is the spectrum function or frequency signal.
- $f(x)$ is the interferogram function or time signal.

However, since a computer can only work with finite discrete signals and not continuous ones, the integral can be replaced by a sum and the infinite borders of the integrals can be replaced by a finite number:

$$f_k = \frac{1}{N} \sum_{n=0}^{N-1} F_n e^{\frac{2\pi i k n}{N}} \qquad F_n = \sum_{k=0}^{N-1} F_k e^{-\frac{2\pi i k n}{N}} \qquad [41]$$

CHAPTER III

RESULTS AND DISCUSSION

In infinite crystalline materials, the Raman shift and line shape are determined by the energy and lifetime of the optical phonon at the center of the Brillouin zone. Localized elastic fields (caused by point defects) and extended elastic fields (caused by internal or external stress), however, alter the energy and lifetime of the zone center optical phonon, and consequently modify the Raman shift and line shape [42,43]. In addition, the interaction between light and matter may trigger several mechanisms that can further distort the Raman spectrum. For instance, high laser powers can induce high concentrations of free carrier, and hence the induced free carriers continuum gas can couple with the discrete phonon modes to give rise to the so-called Fano resonance [44], which usually results in an asymmetric Raman line shape [45, 46]. Moreover, high laser powers can cause a local temperature rise, which reduces the lifetime of the excited phonons and weakens their energies. This temperature-related phenomenon further broadens the Raman peak and shifts it toward lower frequencies [47]. In nanosized crystallites, additional size effects combine with the effects described above, distorting further the Raman spectrum [48]. In fact, in nanosized crystallites, the Heisenberg uncertainty principle imposes the relaxation of the conservation of the total momentum, and consequently the relaxation of the requirement that only the zone center optical phonons participate in the Raman scattering processes. Thus, phonons away from the Brillouin zone center contribute to the response of the nanosized crystallite to an optical excitation. According to Heisenberg uncertainty principle, all the phonons whose wavevectors are roughly equal to or smaller than the inverse of the crystallite size contribute to the response of the crystallite to an optical excitation [72,49]. This results in a further downshift and

broadening of the Raman peak. It follows from the discussion above that the Raman shift and line shape may be determined by many effects combined together [50].

In what follows, two attempts that aim at enhancing the photovoltaic effect in Silicon-based solar cells are presented. The first model is based on randomly distributed ZnO NWs grown on a Silicon substrate, whereas the second model is based on Silicon resonators arrays periodically deposited into a two-dimensional lattice on a Silicon substrate.

A. Zinc Oxide Nanowires:

1. Properties, Characterizations and Applications

Zinc Oxide nanowires (ZnO NWs), a major component in the fabrication of electronics, low-voltage and short-wavelength optoelectronics, photonics and solar cells devices, are a distinctive material that exhibits semiconducting, piezoelectric and pyroelectric properties.

This One-Dimensional (1-D) semiconductor nanostructure, has been of immense interest in both academic research and industrial applications, due to its potential as building blocks for other structures.

Zinc Oxide nanowires are considered the most important nanomaterials for nanotechnology in today's research, among all the other One-Dimensional nanostructures. [51]

With a wide bandgap of 3.37 eV and a large exciton binding energy of 60 meV at room temperature, Zinc Oxide nanowires, which belong to the II-VI group, exhibit strong piezoelectric and pyroelectric properties due to a lack of a center of symmetry in wurtzite, combined with large electromechanical coupling. [51]

In addition, the high exciton binding energy (60 meV) in ZnO crystal can ensure an efficient excitonic emission at room temperature. [52]

The wurtzite structure of ZnO (Fig. 3.2), can be described as a number of alternating planes composed of tetrahedrally coordinated O^{2-} and Zn^{2+} ions, stacked alternately along the c-axis (Fig.3.1). [53]

Polar surfaces of positive and negative charges, (0001)-Zn and (0001)-O respectively, are produced by the oppositely charged ions, which also results in a normal dipole moment and spontaneous polarization along the c-axis, as well as a divergence in surface energy. [53]

Other characteristics of ZnO are as follows: the melting point is 1975 °C, the density is 5.67 g/cm³ and a lattice constant of a=3.25 and c=5.207 Å. [57]

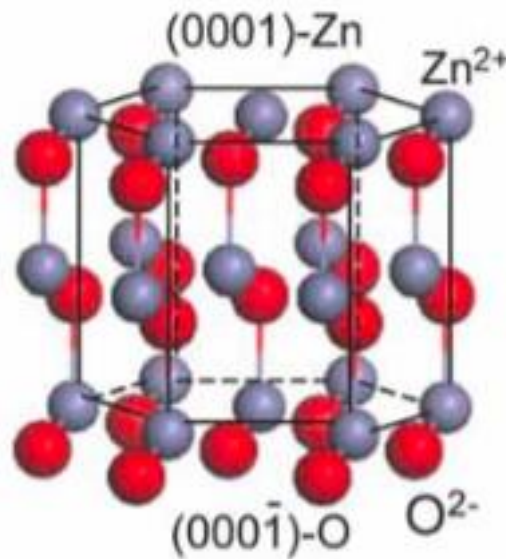


Fig. 3.1 Structure model of ZnO, showing the \pm (0001) polar surfaces

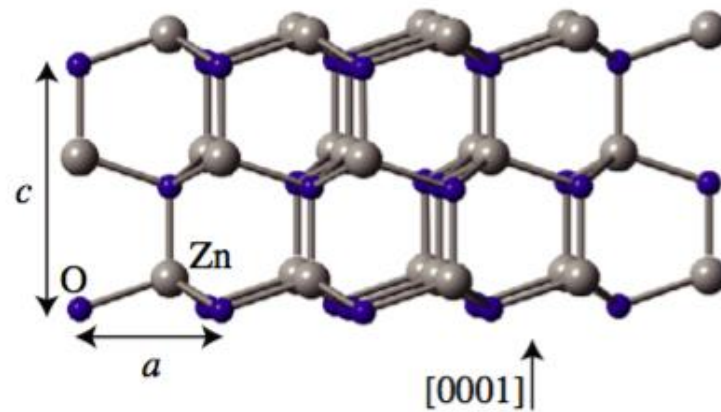


Fig. 3.2 The wurtzite crystal structure of ZnO with lattice parameters a and c indicated

Zinc Oxide is known to be an n-type semiconductor, due to the electron donors that originate from its native defects, such as oxygen vacancies, zinc interstitials, or incidental hydrogen introduced during the growth process [54,55].

Heating the ZnO arrays to high temperatures generally creates these vacancies, which form impurity bands with shallow donor levels with ionization energy about 30-60 meV and deep levels around 0.7-2.3 eV [54,55].

Further researches have proved that n-type conductivity can be enhanced by doping Group-III (Al, Ga, In) and Group-IV(Sn) elements into ZnO [55].

On the other hand, p-type ZnO has been investigated by incorporating Group-V elements (N, P, As, Sb). However, obtaining p-type doping in ZnO has proved to be a very difficult task. [55,56]

Some of the investigated reasons as to why it is hard to achieve a p-type doped ZnO would be: the ability of ZnO to revert towards n-type conductivity which makes it unstable, the defects which are not responsible for n-type conductivity, play a role as compensating centers

in p-type doping, and the fact that there are very few candidate shallow acceptors in ZnO. [55]

Zinc Oxide is characterized by thermal stability during the usage, and possesses as well a high radiation, chemical and thermal resistance [55,57].

Zinc Oxide is responsive to many gases, and its usage transcends the gas sensors to include varistors and generators of surface acoustic waves, due to its unique optical, acoustic and electric properties [55,57].

Zinc Oxide nanowires exhibit two luminescence bands: a short wavelength band located near the absorption edge of the crystal and denoted by “the edge luminescence”, and a broad long-wavelength band for which the maximum is in the green spectral range (FIG. 3.3) [57].

For the edge luminescence, which has an excitonic nature, its maximum is at 3.35 eV and its decay time is 0.7 nS.

As for the green luminescence, it arises as a result of electronic transitions from the ground and excited states, of a shallow donor to some deep acceptor Zinc vacancies [57].

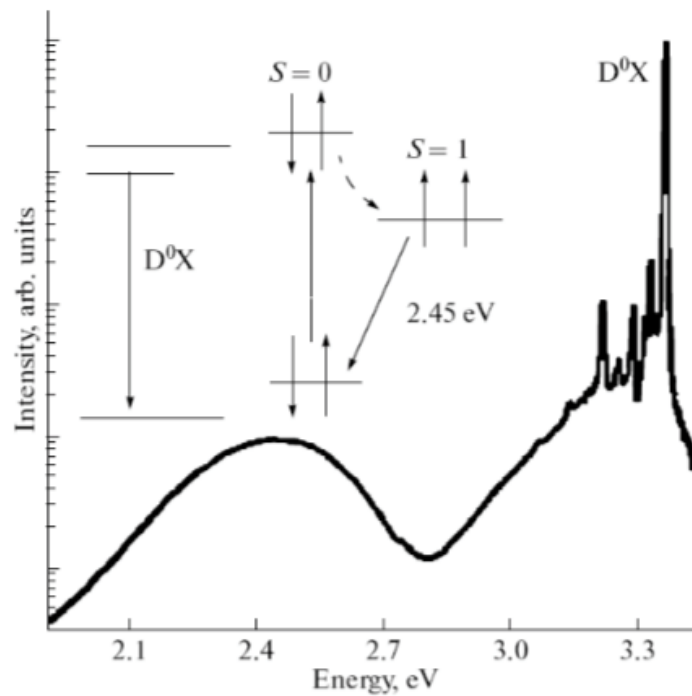


Fig. 3.3 Photoluminescence spectrum of a ZnO crystal and a model of electronic transitions.

Zinc Oxide nanowires are as well a major component in the fabrication of ultrafast hybrid plasmonic lasers.

These plasmonic lasers achieve optical confinement using the surface plasmon polaritons and quasi particles of photons and electrons at metal-dielectric interfaces. In addition, the ZnO excitons are exhibited near the surface plasmon polariton frequency which provide an accelerated spontaneous recombination, gain switching and gain recovery in comparison to conventional photonic ZnO nanowires lasers [58].

Furthermore, what separate this new hybrid class of light source from the conventional ZnO nanowires lasers, is that their spatial scale is decoupled from the vacuum wavelength which provides a faster light-matter interaction [59].

These plasmonic lasers consist of individual ZnO nanowires placed on a 10 nm thick lithium fluoride (LiF) spacer layer over a silver (Ag) substrate (Fig. 3.4). The LiF spacer layer

provides optical confinement control and isolates ZnO excitations from rapid cooling at the metal surface [60].

Then, under optical pumping, ZnO displays very strong optical gain necessary to achieve plasmonic lasing near its band-edge at 3.37 eV and with a large binding energy of 60 meV to ensure its stability at room temperature [61].

These ultrafast hybrid plasmonic lasers are used in a vast range of applications that extend to include the following: Raman sensing, non-linear optical switching, non-linear frequency generation and in the physics of strong field phenomena as well [62,64,65,66].

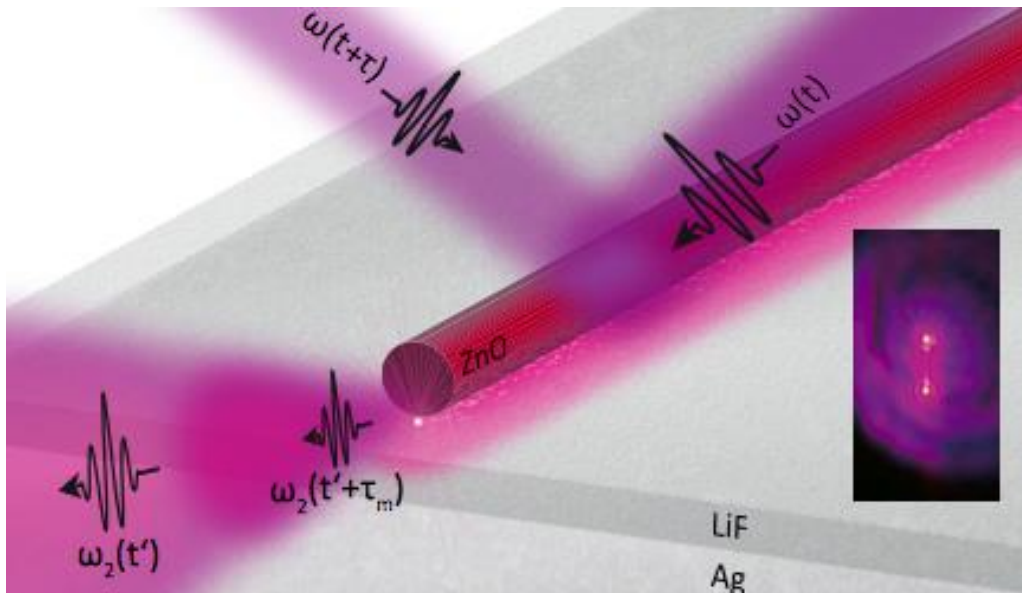


Fig. 3.4. Schematic of the geometry and the emission of a ZnO nanowire optically excited with two time-delayed (τ) pump pulses. The inset shows a picture of a lasing plasmonic nanowire.

Some experimental works have shown that ZnO in its various shapes, in particular the nanowires, is very resistive to high-energy radiation, making it a suitable candidate for space applications than other wide band-gap semiconductors. [67] It has also been shown, theoretically and experimentally, the size-dependence of Young's Modulus in Zinc Oxide nanowires. For diameters smaller than about 120 nm, the Young's Modulus of ZnO nanowires increases dramatically with decreasing diameters [67].

Zinc Oxide nanowires also exhibit thermodynamical properties like heat capacity and thermal conductivity which are strongly influenced by the phonon properties particularly the vibrational density of states. It has relatively high heat capacity, high heat conductivity and low thermal expansion. The specific heat capacity of ZnO is reported to be about $40 \text{ J.mol}^{-1}\text{K}^{-1}$ AT 300K [69]. The thermal expansion coefficients are reported as $\alpha_c = 2.49 \times 10^{-6} \text{ K}^{-1}$ and $\alpha_a = 4.31 \times 10^{-6} \text{ K}^{-1}$ for expansion parallel and perpendicular to c-axis respectively. The thermal conductivity of ZnO is reported to be about $k = 1.0 \text{ W cm}^{-1} \text{ K}^{-1}$ at 300 K, making ZnO a suitable material for high power electronic devices.

2. Application of ZnO NWs in Silicon-Based Solar Cells

Our first attempt at a solution, consisted of the deposition of a randomly distributed Zinc Oxide nanowires ZnO NWs, of different diameters and different heights, on a Silicon substrate.

It can be clearly seen, that the Raman spectrum, of the bulk Si substrate solely, reveals a characteristic sharp peak near 520 cm^{-1} accompanied by a downshift and broadening (FIG. 3.5 and 3.6, Black curve).

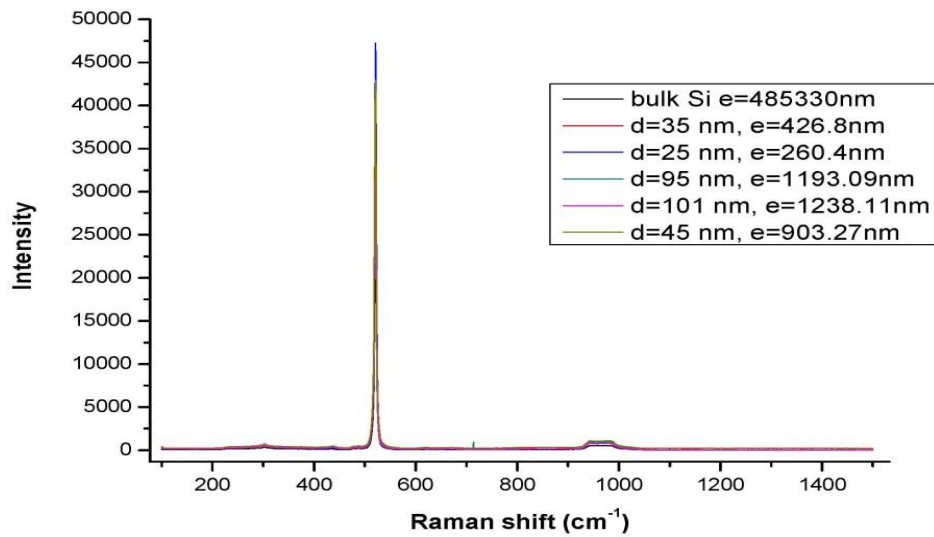


Fig. 3.5 Raman spectra of bulk Si, and of the same substrate but with ZnO nanowires of different diameters and different lengths grown on it. These Raman spectra show no characteristic peak that corresponds to wurtzite hexagonal structure of ZnO nanowires.

It is further observed, that the Raman spectra from the ZnO NWs deposited on a silicon substrate exhibited a significant Raman enhancement from the Si substrate and did not show any signatures of Raman scattering from the ZnO nanowires, signifying that there is no interaction between light and the ZnO Nws (FIG. 3.6).

This reveals that the presence of the ZnO nanowires helps enhancing the signal of the Si substrate, by forward scattering the incident light into the substrate.

Thus, it is believed that the localized Mie resonance in the ZnO cylindrical resonators induced forward scattering of the normally incident light into the Si substrate, beneath the resonators, on which the ZnO nanowires are deposited, and therefore leading to the presence of a strong field in the Si substrate.

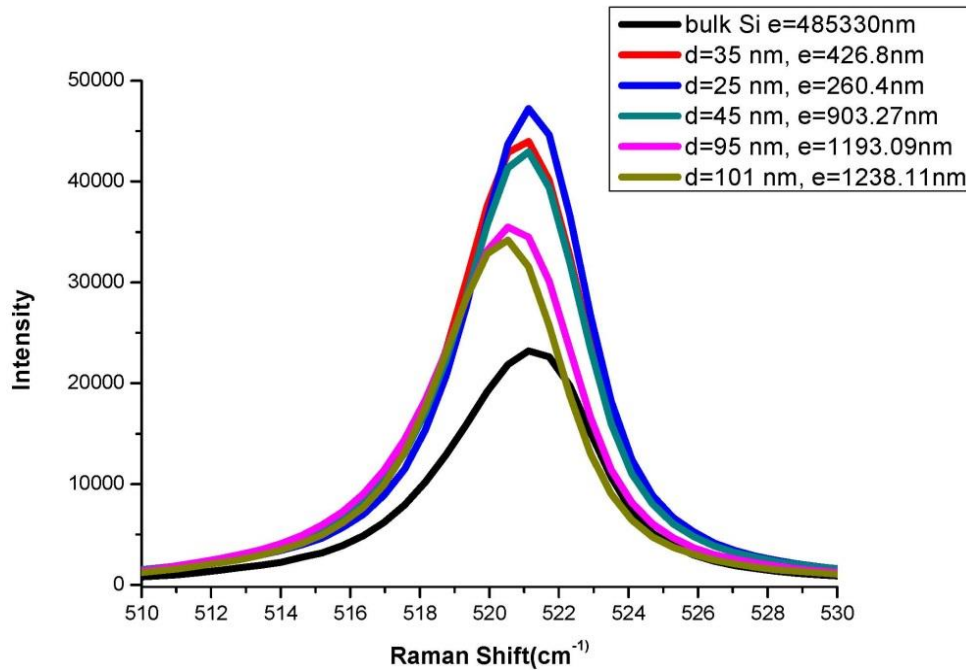


Fig. 3.6 Enlarged Raman spectrum of bulk Si, and of the same Si substrate but with ZnO nanowires grown on it. This spectrum shows how the characteristic Si peak varies as a function of the diameter and the length of the ZnO nanowires.

Regarding the parameters by which the Raman scattering intensity is impacted, we noticed that nanowires with varying diameters and lengths, affect the signal differently. It is observed, from the spectrum, that as the diameter and the length of the nanowires decreased, the characteristic silicon peak increased significantly (**FIG. 3.6**).

Furthermore, since the Raman effect is not exhibited in the infrared region rather only in the visible region, and in order to confirm our findings that the random deposition of ZnO NWs pump/forward scatter the incident light into the Si substrate, we tested this theory in the infrared region as well by using the Fourier Transform Infrared (FTIR) spectroscopy.

It can be clearly seen, in FIG. 3.7 below, that the FTIR spectrum of the bulk Si substrate solely, did not show any signal, but rather almost remained horizontal signaling that no reflectance or transmittance occurred.

Whereas, the IR reflectivity measurements of the ZnO NWs showed a clear drop, in terms of reflectance, relative the IR reflectivity spectrum from a bare Si substrate, which is an indication that almost the totality of the incident IR light was not reflected by the ZnO but rather it was forwardly scattered/transmitted into the Si substrate.

Therefore, we were able to confirm using Raman spectroscopy and FTIR spectroscopy, that a random deposition of ZnO NWs on a bare Si substrate, exhibits tremendous potential in pumping/forward scattering the incident light towards the Si substrate, and hence solving the high reflectivity or the lossy light issue of the Si structure.

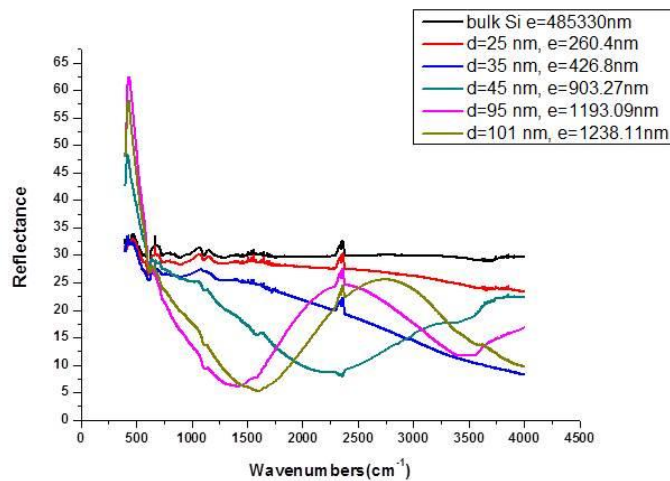


FIG. 3.7 Fourier Transform Infrared Reflectivity FTIR spectra of bulk Si, and of the same Si substrate but with ZnO nanowires grown on it.

This solution might have solved one aspect of the problem regarding the photovoltaic enhancement in Si, which is the reduction of the lossy light, and proved that ZnO nanowires deposited on a Si substrate can be crucial and beneficial in forwardly scattering almost the totality of the incident light within the latter. However, this method did not prove successful in terms of providing an interaction between confined light and confined phonons in nanosized crystallites, and therefore solving the indirect band gap mismatch in Si, and this was proved clearly in the Raman spectra measurements, since the latter displayed an enhancement that is purely characteristic of the Silicon.

B. Application of Periodic Silicon Resonators Arrays on a Silicon Substrate

In another attempt at a better, improved solution that would solve both issues, the lossy light and the indirect electronic band structure of Si, different sets of Silicon resonators arrays were periodically deposited into a two-dimensional lattice on a Silicon substrate.

The samples investigated in this work consist of Si resonators periodically arranged in a two-dimensional lattice on a Si substrate, and the surface structuring of Si was made at low temperature to prevent any impurity diffusion. Hence, we do not expect any stress- or impurity-induced elastic fields contributing to the measured Raman spectra. In order to rule out the effect of laser heating and laser-induced Fano resonance, we have decreased the excitation laser power successively until both Raman peak position and broadening became independent of laser power. It is worth noting here that we found effects of Fano resonance and laser heating for a laser power as low as $0.2 \text{ mW}/\mu\text{m}^2$, which is five times lower than the reported threshold power for the effects of laser heating and Fano resonance [70, 71]. We address the reason behind this observation at the end of this section.

Table I. Detailed structural description of the samples investigated.

Set	Sample	Resonator height (nm)	Resonator bottom diameter (nm)	Resonator top diameter (nm)	Ratio of the top diameter to the bottom diameter	Average spatial correlation length (nm)
I	S _{I,1}	450	134	15	0.112	∞
	S _{I,2}	590	453	413	0.912	6.2
II	S _{II,1}	800	334	43	0.129	5
	S _{II,2}	825	306	125	0.408	3.7
	S _{II,3}	875	380	235	0.618	6.5
III	S _{III,1}	1150	450	100	0.222	6.2
	S _{III,2}	1280	650	190	0.292	4.3
	S _{III,3}	1240	291	159	0.546	4.1

In FIG.3.8, we illustrate the Raman spectra of the samples investigated (see Table I.) together with the Raman spectrum of a bare Si substrate. All the spectra in FIG. 3.8 are recorded by using a laser power of 0.1 mW/ μm^2 and long integration time to avoid any effect of Fano resonance and laser heating. As can be noticed, most of the structured samples present a broadened and downshifted Raman peak relative to the bare Si substrate Raman peak. Since we have ruled out the effects of laser heating and Fano resonance, we confidently attribute this to phonon confinement in nanosized crystallites in the resonators. In other

words, we attribute the observed softening and broadening of the Raman resonance to the presence of nanosized crystalline zones embedded in highly defective Si in the resonators. This hypothesis is supported by previously reported Raman and thermal measurements demonstrating the presence of defect-induced confined phonons in large arrays of Si resonators [22, 23,72].

Besides the broadening and downshift of the Raman peak, FIG. 3.8 shows that the resonators induce a remarkable Raman enhancement. If the Raman spectra in FIG.2 were corrected for the areal density of the resonators, the Raman enhancement would be of orders of magnitude. As mentioned above, the phonon confinement breaks the conservation of the total momentum and allows all the phonon modes whose wavevectors equal to or smaller than $\frac{1}{D}$ (where D is the size of the crystallites in which the phonons are confined) to contribute to the sample's response to an optical excitation. This would indeed imply a Raman enhancement of the order of D^{-3} if we consider a phonon dispersion in a three-dimensional Brillouin zone. However, on the other hand, the Raman scattering efficiency is proportional to the interaction volume, which is roughly equal to D^3 . Therefore, we believe that the observed Raman enhancement is not due to phonon confinement effect. It is also known that isolated nanosized crystallites, or nanosized crystallites embedded in an amorphous medium with a very different index of refraction n can show Raman enhancement due to electromagnetic resonances induced by local field effect and surface phonon modes [80]. However, since crystalline and amorphous Si have similar indices of refraction, the Raman enhancement observed in our experiments cannot also be attributed to local field inducing electromagnetic resonances and surface modes contributing to the measured Raman spectra. Nonetheless, it has been demonstrated theoretically and experimentally that, similar to localized plasmon resonances in plasmonic nanoresonators, localized Mie resonances in dielectric resonators at

the points of a two-dimensional lattice induce highly coherent oscillations in the dielectric resonators, which leads to strong field confinement in the dielectric resonators [20,45]. We believe that this is the only reasonable explanation of the Raman enhancement observed in our experiments. Therefore, we can conclude from the Raman measurements illustrated in FIG. 3.8 that large arrays of Si resonators could ensure interaction between confined phonons and confined photons, and strongly enhance the photovoltaic effect in Si.

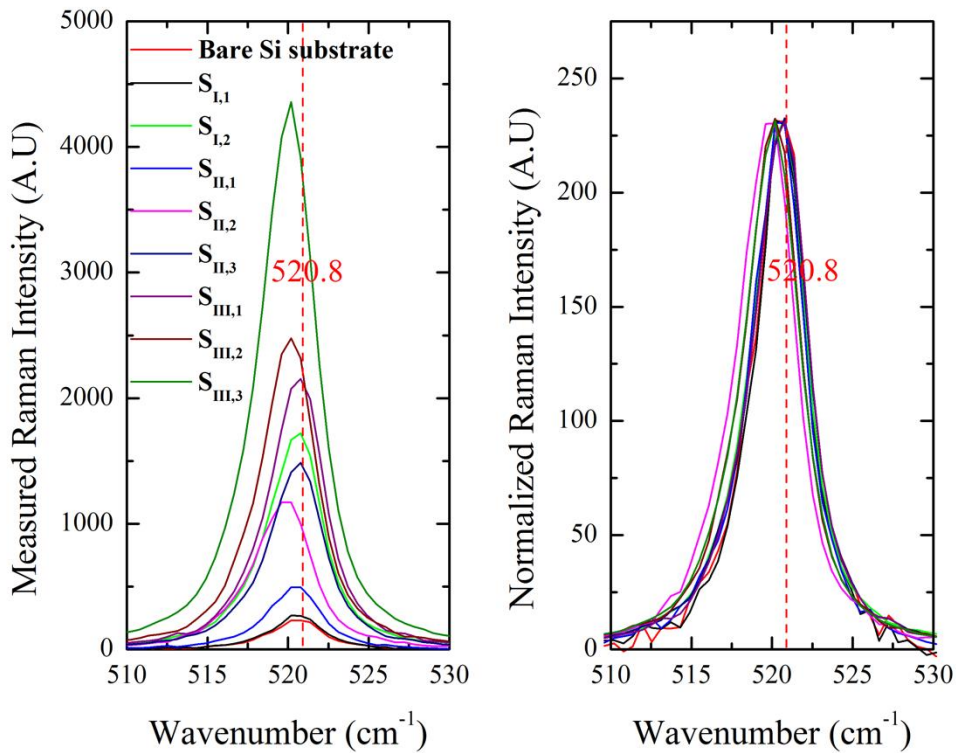


FIG. 3.8 Raman spectra from the investigated structured Si substrates and a bare Si substrate. Left-hand side: As measured Raman spectra. Right-hand side: Normalized Raman spectra. The position of the Raman peak of the bare Si substrate at 520.8 cm^{-1} is highlighted to illustrate the downshift of the Raman peaks corresponding to the structured Si substrates.

Regarding the downshifting and the broadening of the Raman peak which is the result of phonon confinement in nanosized crystallites, numerous works have done on that matter taking into account several factors starting from: the size distribution and the shape of the crystallites, as well as the position and the shape of the Raman spectra.

Below, we present the established models used to quantify the phonon confinement in low-dimensional crystals.

C. Phonon Confinement Models for Raman Spectroscopy of Nanostructured Materials

In 1981, H. Richter, Z.P. Wang and L. Ley presented a model that accounts for the observed variations in the position and shape of Raman spectra of microcrystalline silicon [73]. This model is based on the relaxation of the conservation of crystal momentum in the creation and the decay of phonons in microcrystals.

Two cases can be considered: that of an infinite crystal and another regarding finite crystal. However, the main focus in this work and in what follows is to confine the phonon to a crystal of specific geometric shape, and therefore limiting the study to a finite crystal.

In the case of infinite crystal, the wave function of a phonon is given by the following equation:

$$\phi(\vec{q}_0, \vec{r}) = u(\vec{q}_0, \vec{r})e^{-i\vec{q}_0 \cdot \vec{r}}$$

Where $u(\vec{q}_0, \vec{r})$ is the periodicity of the lattice and \vec{q}_0 is the wave vector.

On the other hand, if the studied crystallite is assumed to be spherical with a diameter L, therefore the phonon is now being restricted to the volume of the crystallite, and such confinement imposes the replacement of ϕ by a new phonon wave function as following:

$$\begin{aligned}\psi(\vec{q}_0, \vec{r}) &= A \exp\left(-\frac{r^2}{2}\left(\frac{L}{2}\right)^2\right) \phi(\vec{q}_0, \vec{r}) \\ &= \psi'(\vec{q}_0, \vec{r}) \cdot u(\vec{q}_0, \vec{r}) \text{ (eq. I)}\end{aligned}$$

With $|\psi|^2 = A^2 \exp\left(-r^2/\left(\frac{L}{2}\right)^2\right)$ is the Gaussian function &

$$\psi'(\vec{q}_0, \vec{r}) = A \exp\left(-\frac{r^2}{2}\left(\frac{L}{2}\right)^2\right) e^{-i\vec{q}_0 \cdot \vec{r}} \text{ (eq. II)}$$

Such Gaussian distribution implies that the function ψ is localized to $|r| \leq L$ and has a width of $\sqrt{\ln 2} L$.

In order to calculate the Raman spectrum, $\psi'(\vec{q}_0, \vec{r})$ must be expanded in a Fourier series:

$$\psi'(\vec{q}_0, \vec{r}) = \int d^3q C(\vec{q}_0, \vec{q}) e^{i\vec{q} \cdot \vec{r}}$$

Where the Fourier coefficients $C(\vec{q}_0, \vec{q})$ are given by:

$$C(\vec{q}_0, \vec{q}) = \frac{1}{(2\pi)^3} \int d^3r \psi'(\vec{q}_0, \vec{r}) e^{-i\vec{q} \cdot \vec{r}}$$

Inserting eq. II of ψ' into the expression above, yields:

$$C(\vec{q}_0, \vec{q}) = \frac{AL}{(2\pi)^{3/2}} \exp\left(-\frac{1}{2}\left(\frac{L}{2}\right)^2(\vec{q} - \vec{q}_0)^2\right)$$

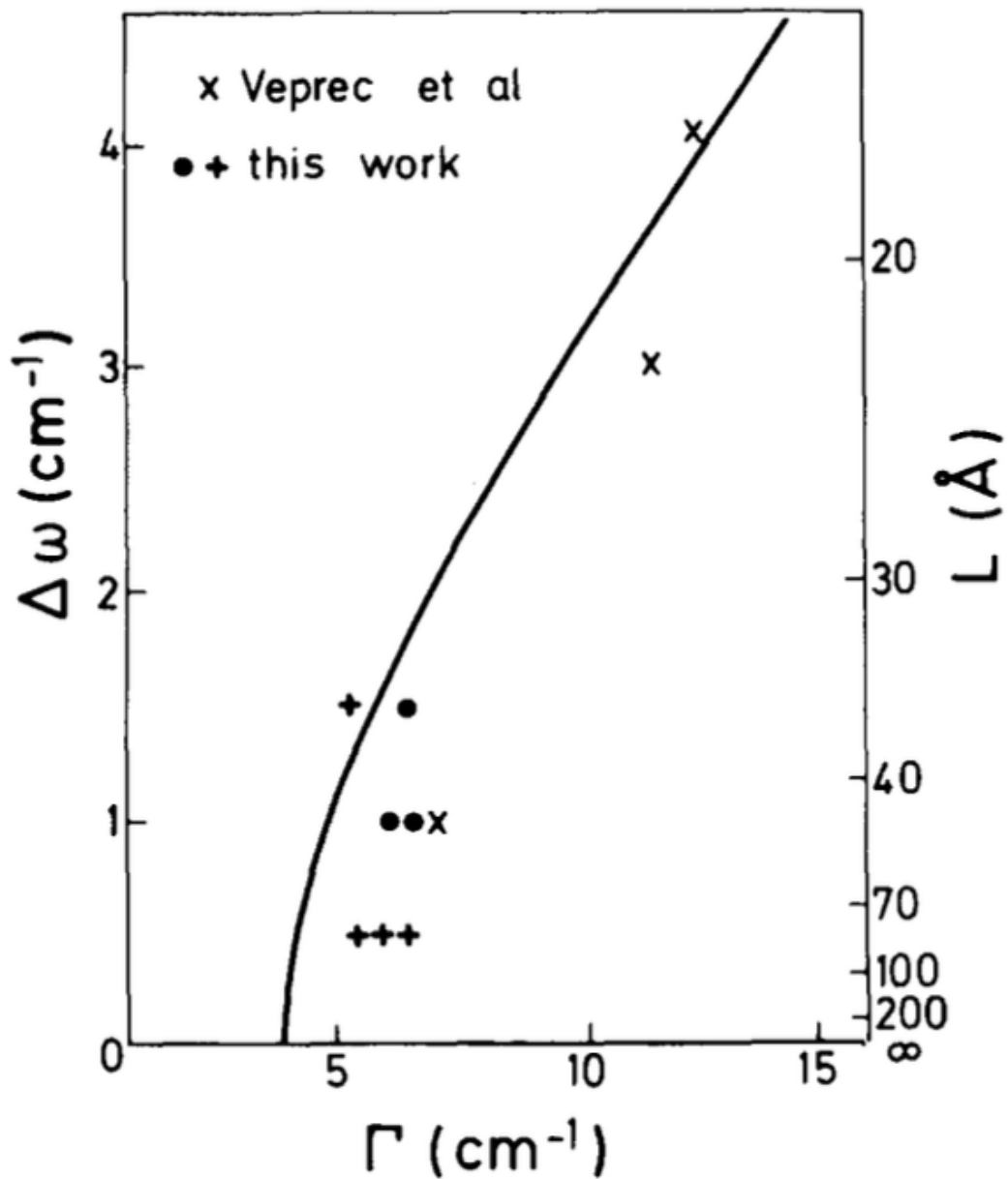
From (eq. I), it can be deduced that the microcrystal phonon wave function is a superposition of Eigen-functions ψ and ψ' with \vec{q} vectors centered at \vec{q}_0 . These Eigen-functions are weighted through the coefficients $C(\vec{q}_0, \vec{q})$ according to the particular choice of localization that is dictated by the Gaussian distribution function $|\psi|^2$.

Such localization of the phonon is in effect a relaxation of the $\Delta q = 0$ selection rule due to the very small size of the crystallite, which implies that the phonon transition matrix elements $|\langle \vec{q}_0 | \hat{\delta} | \vec{q} \rangle|^2$ have non-vanishing values according to:

$$|\langle \vec{q}_0 | \hat{\delta} | \vec{q} \rangle|^2 = |\langle \vec{q}_0 | \hat{\delta} | \vec{q}_0 \rangle|^2 \cdot C(\vec{q}_0, \vec{q})^2$$

Where $\hat{\delta}$ is the photon – phonon interaction operator.

In this model, the main focus is on the excitation of the optical phonon in silicon located at the zone center where $\vec{q} = 0$. Furthermore, If the transitions with $\vec{q} \neq 0$ are taken into account, then the energies w of these added contributions to the Raman spectrum would be determined by the dispersion relations $w(q)$. In addition, these additional transitions with $\vec{q} \neq 0$ will lead to a broadening of the Raman line by an amount Γ_1 and an associated redshift Δw of its mean position, with Γ_1 and Δw are being related together to each other through the dispersion relation $w(q)$ and the coefficients $C(\vec{q}_0, \delta)$ (FIG. 3.9).



1-

Figure 3.9 Relationship between shift $\Delta\omega$ and width Γ of the Raman line in microcrystalline silicon calculated for a range of Δq values in silicon. L represents the size of the silicon crystallite.

Γ , in Figure 3.9, is the geometrical sum of the intrinsic width Γ_0 of the zone-center phonon and the additional width Γ_1 due to the phonon dispersion (additional transitions with $\vec{q} \neq 0$ discussed earlier).

It should be noted that the phonon dispersion due to photon-phonon interactions, that occurs away from the zone-center phonon, in other words near the two-phonon Raman spectrum, is of negligible effect on the shape of the curve in Figure 1.

Regarding the right side ordinate of Figure 3.9, which represents the size of the silicon crystallites in Angstrom, such parameter L is crucial for the derivation of the Fourier coefficients $C(\vec{q}_0, \vec{q})$, since this parameter is featured in the equation:

$$C(\vec{q}_0, \vec{q}) = \frac{AL}{(2\pi)^{3/2}} \exp\left(-\frac{1}{2} \left(\frac{L}{2}\right)^2 (\vec{q} - \vec{q}_0)^2\right)$$

It is also shown by Richter et al that the numerical values, which are model dependent, are appropriate for the Longitudinal LO branch of the phonon dispersion in the direction $\Gamma - X$.

Furthermore, Figure 3.9 shows some experimental points of silicon films, that were prepared by the plasma transport method, which follow the calculated relationship between $\Delta\omega$ and Γ for spherical silicon crystallites, while the crystallite sizes calculated are in agreement with the nature of L as model parameter.

As for the Raman lines of microcrystalline samples, they predictably show an asymmetry tailing towards lower Raman shifts (lower energies), which is successfully reproduced in this model as shown in Figure 3.10.

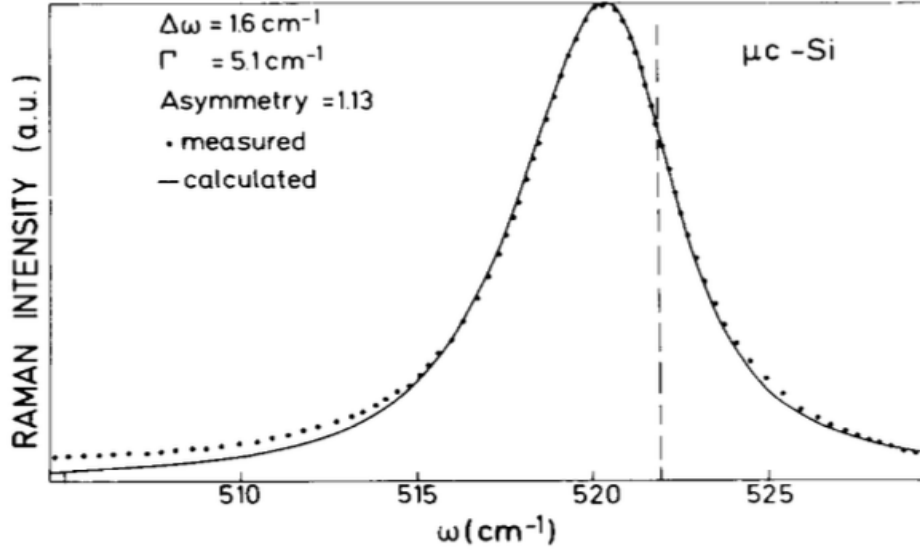


FIG. 3.10 Measured and calculated Raman line of μc -Si sample. The dashed line indicates the Raman shift for c-Si. The asymmetry is defined as a/b , where a and b are the half-widths of the Raman line.

The extra intensity below 515 cm^{-1} , which contributes to the tailing towards lower Raman shifts, is due to contributions from amorphous regions in the sample.

The dashed line in Figure 3.10 represents the Raman shift for Crystalline-Si (c-Si), for which the decay of the zone-center optical phonon obeys the the wave vector conservation rule. However, according to Klemens' work titled "Anharmonic Decay of Optical Phonons", the optical phonon splits into two acoustical phonons of equal and opposite momentum and of frequencies w' and w'' respectively, due to the cubic anharmonicities.

The corresponding transition probability of an optical phonon into two acoustical phonons can be written as following:

$$\Gamma_0(w_0) \propto |M|^2 \cdot N(w') \cdot N(w'') \quad (\text{eq. 3-1})$$

with $w' = w'' = \frac{1}{2}w_0 = 261 \text{ cm}^{-1}$; $q = q' + q''$ and $w_0 = w' + w''$

Where M is the transition matrix element; $N(w)$ is the density of acoustical phonon states at the energy w , and w_0 is the frequency of an optical phonon at the zone center for which $q_0 = 0$.

Extending the Raman effect in crystalline Si into that of microcrystal Si, by relaxing the wave vector conservation, equation (3-1) can therefore be replaced by:

$$\Gamma_0(w_0) \propto |M|^2 \int F(\vec{q}_-, \vec{q}_+) N\left(\frac{w_0}{2} - w'\right) \cdot N\left(\frac{w_0}{2} + w'\right) dw' \quad (\text{eq. 3-2})$$

Where $F(\vec{q}_-, \vec{q}_+)$ is a Gaussian weighing function of width Δq and centered around $\vec{q}\left(\frac{w_0}{2}\right)$, while the integration is limited to a range of energies w' as following:

$$F(\vec{q}_-, \vec{q}_+) = F\left(\left|\vec{q}\left(\frac{w_0}{2} - w'\right) - \vec{q}\left(\frac{w_0}{2} + w'\right)\right|\right)$$

If the averaged two phonon density of states defined in equation 9 exceeds the two phonon density of states at $\frac{w_0}{2}$, then an increase in the intrinsic width Γ_0 of the zone-center phonon is expected, and therefore Γ_0 becomes a factor of the temperature dependent Raman line width Γ according to:

$$\Gamma^2(T) = \Gamma_0^2 \left(1 + \frac{2}{e^x - 1}\right)^2 + \Gamma_1^2$$

Where $x = \frac{hw_0}{2kT}$; Γ_1 is the temperature independent contribution to the line-width of microcrystal.

For that matter, the following table displays Γ_0 and Γ_1 parameters obtained from a fit to the temperature dependent Raman line-widths of Figure 3.11, in 4 silicon samples: one single crystal of Si and 3 $\mu c - Si$.

sample	Γ_1 (cm ⁻¹)	Γ_0 (cm ⁻¹)	$\frac{\Gamma_0}{\Gamma_0(\text{cryst})}$	L (Å)
cryst. Si	0	1.7	1	∞
$\mu\text{c-Si}$, $T_D=300^\circ\text{C}$	1.8	2.0	1.18	100
$\mu\text{c-Si}$, $T_D=250^\circ\text{C}$	2.7	2.1	1.24	90
$\mu\text{c-Si}$, $T_D=175^\circ\text{C}$	4.4	2.5	1.47	80

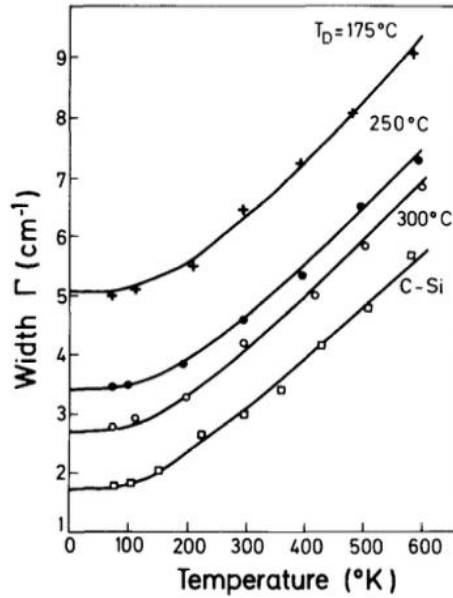


FIG. 3.11 Raman line width Γ vs. Temperature for 4 silicon samples.

The values in the table for Γ_1 and Γ_0 are determined by taking $T \rightarrow 0$ in $\Gamma(T)$ and through the slope of $\Gamma(T)$ for large T , respectively.

It is found that Γ_0 increases with Γ_1 , in other words with a decreasing crystallite size from $L=100$ Angstrom to $L=80$ Angstrom.

This result is in agreement with the phonon dispersion of Si, which validates this One-Phonon Raman Spectrum model in $\mu\text{c-Si}$, since there is a quantitative accordance between the theoretical calculations done and the measurements obtained through the experiment, and hence proving that the relaxation of the wave vector selection rule is crucial in $\mu\text{c-Si}$.

Another model was presented I.H. Campbell and P.M. Fauchet in 1986, titled “The Effects of Microcrystal Size & Shape on The One Phonon Raman Spectra of Crystalline Semiconductors” [74].

This model shows how the appropriate choice of a Gaussian phonon confinement function with a rigid boundary yields consistent results for either Si or GaAs spherical microcrystals embedded in a thin film, and how extending that same rigid confinement function, intended originally for spherical crystals, to different shapes would account for significant different results.

In a similar manner to the previous model, this study follows approximately the same order established by Richter et al. The authors start by writing down the wave-function for a phonon in an infinite crystal:

$$\phi(\vec{q}_0, \vec{r}) = u(\vec{q}_0, \vec{r})e^{-i\vec{q}_0 \cdot \vec{r}}$$

with \vec{q}_0 being the phonon wave-vector and $u(\vec{q}_0, \vec{r})$ has the periodicity of the lattice.

Now considering that the phonon wave-function is partially confined to the volume of the crystallite of diameter L, therefore the new phonon wave-function becomes:

$$\psi(\vec{q}_0, \vec{r}) = W(r, L)\phi(\vec{q}_0, \vec{r}) = \psi'(\vec{q}_0, \vec{r}) \cdot u(\vec{q}_0, \vec{r})$$

With $W(r, L)$ being the phonon weighting function which Richter et al defined it to be a Gaussian $\exp(-2r^2/L^2)$ and assumed it to have a phonon amplitude of 1/e at the boundary of the microcrystal. The new phonon wave-function also infers that it is a superposition of Eigen-functions ψ and ψ' with \vec{q} vectors centered at \vec{q}_0 .

Expanding ψ' in a Fourier series in order to calculate the effect on the Raman spectrum:

$$\psi'(\vec{q}_0, \vec{r}) = \int d^3q C(\vec{q}_0, \vec{q}) e^{i\vec{q} \cdot \vec{r}}$$

Where the Fourier coefficients $C(\vec{q}_0, \vec{q})$ are given by:

$$C(\vec{q}_0, \vec{q}) = \frac{1}{(2\pi)^3} \int d^3r \psi'(\vec{q}_0, \vec{r}) e^{-i\vec{q}\vec{r}}$$

For the spherical microcrystal and Gaussian weighting function used by Richter et al. the Fourier coefficients, for which it is assumed $q_0 = 0$, are:

$$|C(0, \vec{q})|^2 \cong e^{\frac{-q^2 L^2}{4}}$$

Therefore, the intensity of the first order Raman spectrum $I(w)$ is:

$$I(w) \cong \int \frac{d^3q |C(0, \vec{q})|^2}{(w - w(q))^2 + (\Gamma_0/2)^2}$$

Where $w(q)$ is the phonon dispersion curve, and Γ_0 is the intrinsic/natural line-width. The former is considered to be isotropic in order to simplify the calculations, while the integration is done over the entire spherical Brillouin zone.

In a study conducted by Tiong et al. [63], the latter referred to Richter's et al. model to explain the Raman spectra obtained from ion implanted GaAs. However, they had to change the phonon amplitude at the boundary from $1/e$ to $\exp(-4\pi^2)$, since the model proposed by Richter et al. has some limitations for it considers the study of only spherical silicon microcrystals.

In order to find a common ground that would make the theory consistent for both Si and GaAs, and as a result improving the fit, Campbell et al. experimented with several confinement functions with different values at the boundary of the microcrystal. Hence, three weighting functions are proposed to describe the phonon confinement:

- The first one is determined by analogy with the ground state of an electron in a hard sphere, and is given by: $\sin(\alpha r)/\alpha r$, for which $\alpha = 2\pi/L$ so that the boundary value is zero.

- The second one is deduced by analogy with a wave in a lossy medium, in other words it is a medium in which an Electromagnetic wave loses energy as it propagates, and the weighting function is then: $\exp(-\alpha r)$.
- The third one is proposed in anticipation of the size distribution of many microcrystals, and is therefore given by: $\exp(-\alpha r^2/L^2)$.

The results obtained from these three weighting functions, for spherical microcrystals, are displayed in Figure 3.12 below in terms of $\Delta\omega$ Vs. Γ , and compared to the data of other works done by Iqbal et al. and Richter et al.

$\Delta\omega$, in Figure 3.12, represents the frequency shift while Γ represents the line-width, and the scale for both of these components is the same, whereas the scale for the vertical axes on the right hand side which represents both the theoretical and experimental microcrystal size L , varies for each weighting function.

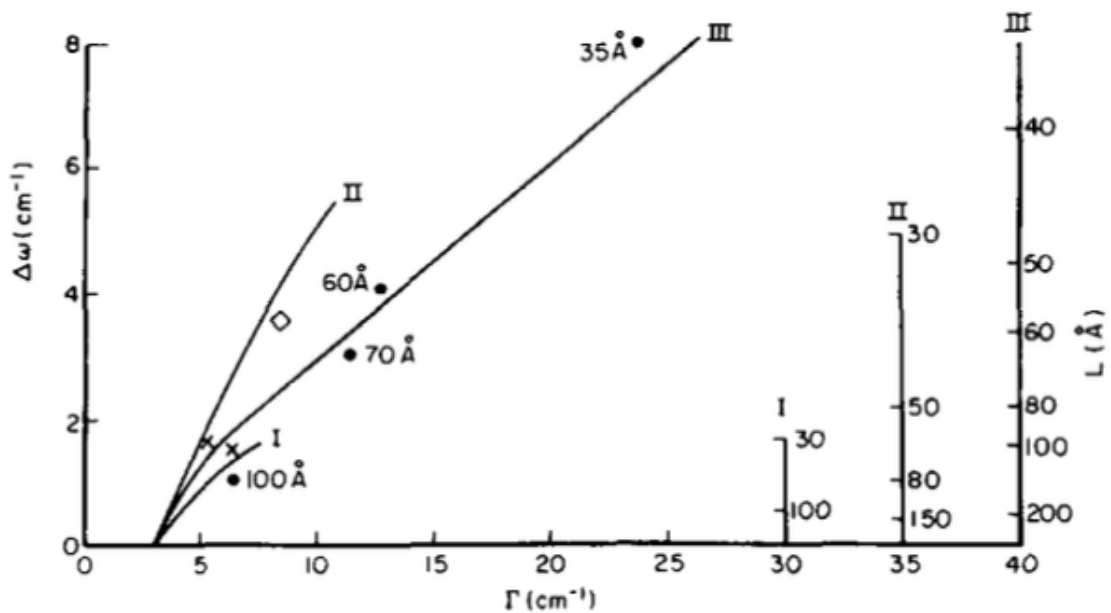


Figure 3.12 The calculated relationship between width, shift and crystal size for spherical microcrystals using three weighting functions: I-exponential, II-sinc and III-Gaussian.

Experimental points are for microcrystalline spheres from the work of Iqbal et al. (●) Richter et al. (X) and this model (◇), while the experimental sizes determined by X-Ray diffraction are indicated when available.

It is apparent in FIG. 3.12 that all functions exhibit a shift, but it can be seen that the extent of shift and broadening for each function differs and is limited to certain microcrystal sizes. Only, the Gaussian confinement function was able to confine phonons down to a microcrystal size of $L=35$ Angstrom, while displaying the largest frequency shift and broadening, in other words the Gaussian weighting function shows agreement with the data with a value of $\exp(-4\pi^2)$ at the boundary of the crystallite which is almost a negligible boundary value.

In addition, this choice of confinement function is in good accordance with the results recorded by Tiong et al. regarding the Raman spectra of ion implantation in GaAs. In conclusion, the choice of this weighting function corresponds to rigid confinement of the phonons in the microcrystal where the amplitude is almost 0 at the boundary.

Now, having defined the appropriate confinement function, which is the Gaussian with its new boundary value, it is only appropriate to test this function on three microcrystals of different shapes (FIG. 3.13). The latter alters the confinement function by assigning a direction to it as well as a magnitude, since the three studied microcrystals shapes are: a sphere, a column/cylinder and a thin film. In that case, the column shaped crystal and the thin film would lead to the following Fourier coefficients:

$$|C(0, q_1, q_2)|^2 \cong e^{-\frac{q_1^2 L_1^2}{16\pi^2}} e^{-\frac{q_2^2 L_2^2}{16\pi^2}} \left| 1 - \operatorname{erf}\left(\frac{iq_2 L_2}{\sqrt{32\pi}}\right) \right|^2 \quad \text{For the column microcrystal}$$

$$|C(0, q_1)|^2 \cong e^{-\frac{q_1^2 L_1^2}{16\pi^2}} \left| 1 - \operatorname{erf}\left(\frac{iq_1 L_1}{\sqrt{32\pi}}\right) \right|^2 \quad \text{For the thin film microcrystal}$$

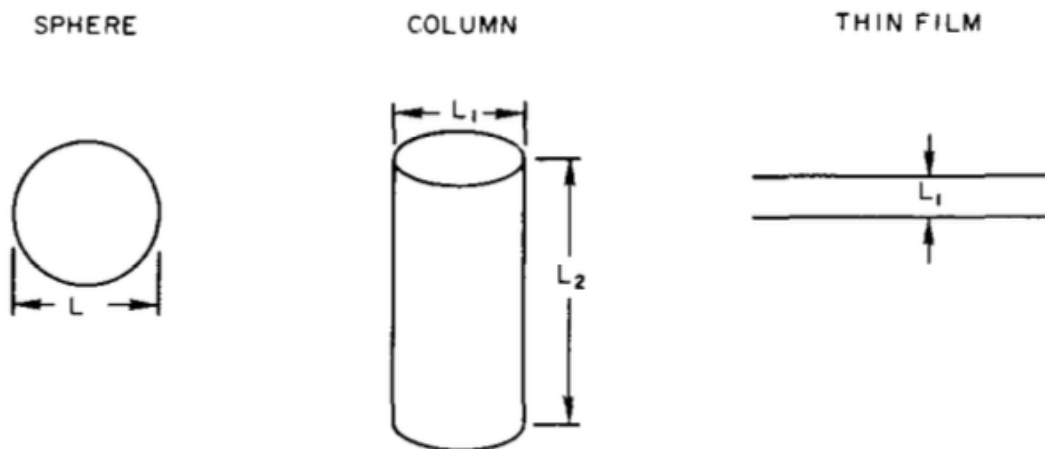


Figure 3.13. The three microcrystal shapes used in Figure 6. The length of the column, L_2 , is considered to be infinite.

FIG. 3.14 (below), shows a comparison between these three shapes in terms of Δw Vs. Γ , and displays the effect of having three, two and one dimensional confinement on the Raman spectrum, while assuming that L_2 is infinite so that the theoretical size plotted is L_1 instead.

the scale for the shift and the width are the same for the three shapes, whereas the scale for the vertical axes on the right hand side, which represents both the crystal's theoretical and experimental (when available) dimensions, is indicated separately for each.

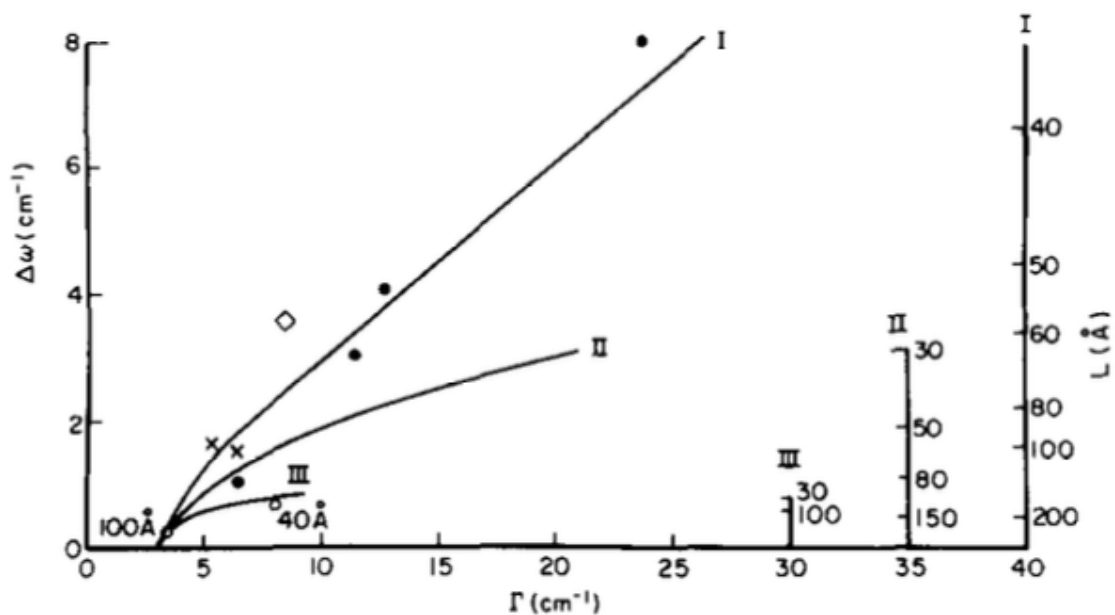


FIG. 3.14 The calculated relationship between width, shift and crystal size for three microcrystal shapes using the Gaussian weighting of Fig. 4. I-sphere, II-column and III-thin film.

The experimental points in FIG. 3.14 are the same as those in Fig. 4, with the addition of the silicon thin film data from a model constructed by Murphy et al. (o), while the thin film thickness were determined by transmission measurements. Whereas, there is no experimental data for thin columns.

Similar to FIG. 3.14, all shapes undergo a shift and a broadening to a certain extent, with the Raman line shape changing to be stronger going from a thin film, to a column and then to a sphere, since these Raman lines are affected by the number of ordinates for each microcrystal, and therefore affected by the crystallographic orientation of the various films.

For the thin film, the confinement occurs only along the Z-direction, while for the column shaped microcrystal, the confinement of phonons occurs along the X and Y-directions. As for

the sphere, the confinement of phonons occurs along three dimensions: X, Y and the Z-directions.

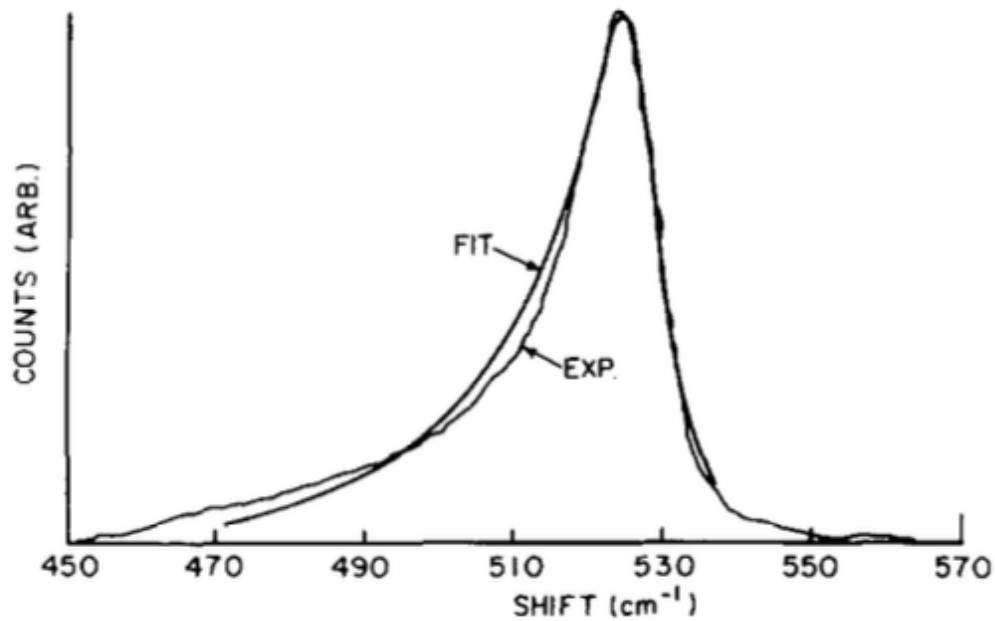


FIG. 3.15. Experimental and theoretical Raman spectra of a 40 Angstrom thin film of Si on sapphire.

FIG. 3.15, displayed above, shows a comparison between experimental and theoretical Raman spectra of a 40 Angstrom silicon thin film on sapphire (SOS) (data displayed in Fig. 3.14 as well), prepared by thermal oxidation by Murphy et al. The theoretical spectrum is corrected and shifted to account for compressive stress in the SOS.

The Raman spectrum shows a good agreement between the theory and the measured data, since both the line-width and the symmetry of both spectra are in good accordance.

In 2010, K. Roodenko et al. proposed a model entitled, Modified Phonon Confinement Model for Raman Spectroscopy of Nanostructured Materials [74], that would improve and correct the discrepancies in Richter-Campbell-Fauchet RCF model, such as:

- pointing out the proper choice of the parameters in the Gaussian confinement function, and therefore showing that the main problem in the RCF model stems from a misinterpretation of the phonon-weighting function that was initially proposed by Richter et al.
- Afterwards, introducing an anisotropic dispersion function into the confinement model which demonstrates that anisotropy is of particular importance for low-dimensional systems, since the broadening of the signal is strongly affected by the phonon dispersion of the material.

○ Defining the Phonon Weighting Function

In a similar manner to the previous two models, this study starts by establishing the equation that describes the wave function for a phonon in an infinite crystal as following:

$$\phi(\vec{q}_0, \vec{r}) = u(\vec{q}_0, \vec{r})e^{-i\vec{q}_0 \cdot \vec{r}}$$

with \vec{q}_0 being the phonon wave-vector, $u(\vec{q}_0, \vec{r})$ a periodic function and r is the space vector.

Considering that the phonon wave-function is partially confined to the volume of the crystallite of diameter L , therefore the new phonon wave-function becomes:

$$\psi(\vec{q}_0, \vec{r}) = W(r)\phi(\vec{q}_0, \vec{r}) = \psi'(\vec{q}_0, \vec{r}) \cdot u(\vec{q}_0, \vec{r})$$

With $W(r)$ being the phonon weighting function, typically defined to be a Gaussian $W(r) = \exp[-r^2/(2\sigma^2)]$, where σ is a constant and matched individually for a given measurement setup and material in accordance with the sample's dimensions.

In this work, the authors discuss the incorporation of the precise phonon-weighting function, the square wave. Then, the latter is compared to an earlier proposed weighting functions and showing that when the parameter σ of the Gaussian is chosen properly, both models, that of Richter and this one, give identical results.

Furthermore, current computational technology allows to carry out effective numerical calculations which makes it possible to incorporate anisotropy into the RCF model.

All of these points will be discussed next.

The Fourier coefficients $C(\vec{q}_0, \vec{q})$ are given in terms of $\psi'(\vec{q}_0, \vec{r})$ as following:

$$C(\vec{q}_0, \vec{q}) \sim \int d^3r \psi'(\vec{q}_0, \vec{r}) e^{-i\vec{q}\vec{r}}$$

For one-phonon scattering, it is assumed that $q_0 = 0$ at the zone center. Therefore, for a Gaussian weighting function of the form $W(r) = \exp[-r^2/(2\sigma^2)]$, the Fourier coefficients gets the following general form:

$$|C(0, \vec{q})|^2 \cong |e^{(-0.5q^2\sigma^2)^2}|$$

It is shown in the literature of other models, in particular in a model built by Adu et al., that the value of the parameter σ is not fixed, and highly disputed instead, since any result can be calibrated to fit the RCF theory if the the “universal parameter” σ is varied appropriately. In addition, this parameter is correlated with the spatial function $W(r)$, hence a proper choice of $W(r)$ is crucial.

When dealing with nanowires structures, it is intuitive to use the square-wave function $W_1(r)$, as shown in figure 3.16 below, to be able to represent the nanowire in the Cartesian coordinates system (x,y,z) as following:

$$W(x, d) = 1 \text{ for } -d/2 < x < d/2$$

else $W(x, d) = 0$ (same for the z direction)

$$W(y, L) = 1 \text{ for } -L/2 < y < L/2$$

else $W(y, L) = 0$

This type of square-wave function confines the structure in space.

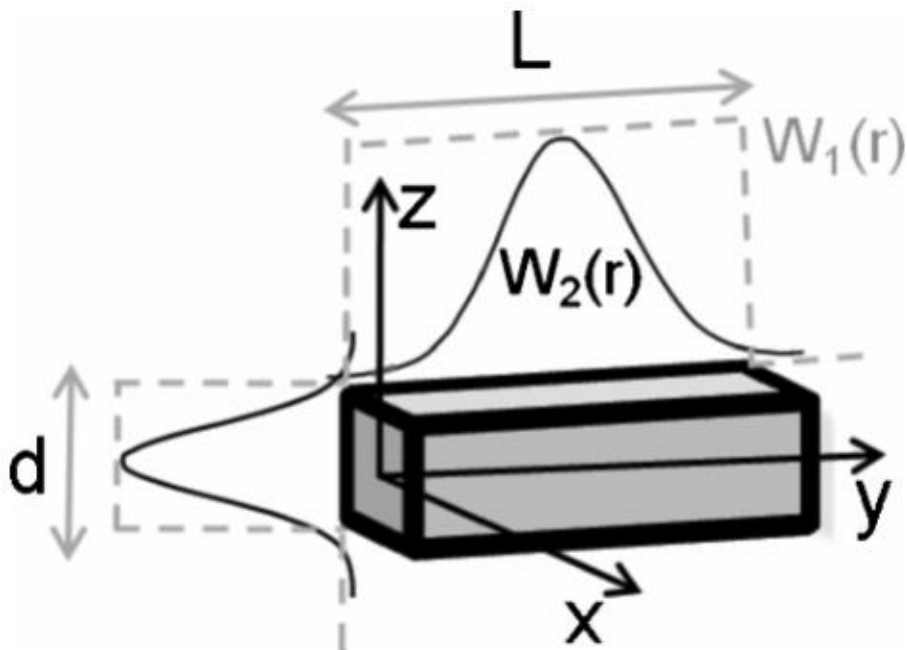


FIG. 3.16 Representation of a nanowire with the face size and length L , and the respective weight functions $W_1(r)$ (square-wave function, dashed) and $W_2(r)$ the Gaussian solid line.

For the Gaussian to match the square-wave function, especially after the Fourier transform, the standard deviation σ in the Gaussian $W(r) = \exp[-r^2/(2\sigma^2)]$, should be equal

to the distances of all points in the square wave from the center and normalized to the number of the points. In other words, σ is given by the following standard deviation equation:

$$\sigma = \sqrt{\langle x^2 \rangle} = \sqrt{\frac{\int_{-d/2}^{d/2} x^2 dx}{\int_{-d/2}^{d/2} dx}} = \frac{d}{\sqrt{12}}$$

This is the general standard deviation equation for any confined shape with a characteristic nanostructure size d in a given direction (x,y, or z).

A comparison is conducted below in Figure 3.17, between the Gaussian function given by $W_2(r) = \exp[-r^2/(2*\sigma^2)]$ with σ from the standard deviation equation., and the square-wave function given by $W_1(r)$ in r and q space. In addition, this comparative plot includes data of the phonon weighting function $W(x)$ that is characterized by a width $d = 50$ arbitrary units, and data from the models proposed by Richter et al. and Campbell and Fauchet.

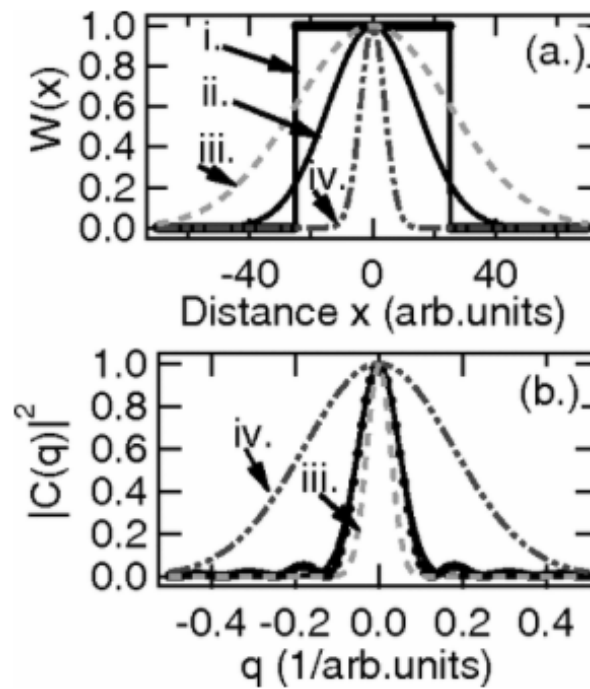


FIG. 3.17. (a) Phonon weighting function $W(x)$ calculated with $d=50$ arbitrary units. (i) square function; (ii) based on $W(x) = \exp[-x^2/(2\sigma^2)]$ with σ from the standard deviation equation; (iii) (dashed) Proposed by Richter *et al.* [60]; and (iv) (dashed-dotted) proposed by Campbell and Fauchet [75].

(b) The corresponding $|C(\vec{q})|^2$. Only the plots corresponding to plots (iv) and (iii) in (a) are marked, the rest of the lines fall closely together.

It is worth reminding the reader that Richter *et al.* suggested that the phonon amplitude falls to the value of $1/e$ at the crystallite boundary, while on the other hand, Campbell and Fauchet proposed a phonon amplitude of $\exp(-4\pi)$ at the boundary of the crystallite. Campbell and Fauchet's choice gives a much narrower window than the crystallite shape which results in a very wide Fourier-transformed Gaussian.

However, in this current model, and in q space, the Gaussian is built upon the author's procedure of "mapping" the Gaussian into a square-wave function as given by equation 6 and represented by dashed lines in FIG. 3.16. It can be seen that the built Gaussian falls completely on the major cycle of the Fourier-transformed square wave.

In addition, the Gaussian proposed by Richter *et al.* is in agreement with the Fourier-Transformed square wave, since it follows the borders of the latter.

In order to weigh the importance on the proper choice of the "universal value" α , the authors of this model, K. Roodenko *et al.*, perform a comparison in terms of the parameter α , between: A Fourier coefficient used in another model by Adu *et al.* and that which is used in this current model. These two coefficients are of the following form:

$$|C(0, q)|^2 \cong e^{(-0.5q^2 d^2 / \alpha^2)} \quad \text{by Adu et al. (Eq. 3-3)}$$

$$|C(0, q)|^2 \cong |e^{(-0.5q^2\sigma^2)^2}| \text{ by K. Roodenko et al. (Eq. 3-4)}$$

The relation between the parameters in Eqs. (3-3) and (3-4) is the following:

$$\sigma^2 = \frac{d^2}{2\alpha^2}$$

In the case of the work of Adu et al., the latter reported results for α in the range: $1.4 < \alpha < 10.4$, with $\alpha = 6.3$, as outlined by Adu et al.

As stated before, the aim of this work is to be able to fit any work into the RCF model, therefore matching equations (3-3) and (3-4), with $\sigma = \frac{d}{\sqrt{12}}$, the parameter α would yield:

$$\alpha = \sqrt{6} = 2.44$$

For that value of α , the Gaussian proposed by Adu et al. would be properly confined and therefore matching the rectangular function.

It has been shown that even when the value of the Gaussian parameter σ varied in many publications (keeping in mind that $\sigma = \frac{d}{\sqrt{12}}$ in this model), the authors who have applied the RCF model to the analysis of Raman data from nanowires samples, have obtained reasonable results.

Such discrepancies in the values of σ could be attributed to parameters that might influence the Raman line shape such as: strain and an induced heat within the nanostructure.

In summary, this part dealt with controversies regarding the proper choice of parameters within the Gaussian confinement function in analysis of Raman lines shapes measured from nanostructures. Then, it has been shown that when considering a rectangular confinement function (square-wave function), these discrepancies can be resolved.

For example, in the case of Richter et al. and “Campbell and Fauchet”, the latter have used the following weighting functions: $W(r) = \exp(-\frac{2r^2}{d^2})$ and $W(r) = \exp(-\frac{8\pi^2 r^2}{d^2})$ respectively. The lingering question in mind, in each case, was: to which value should the Gaussian function decay at the boundary of the crystallite?

However, this work showed that such question posed by whether Richter et al. or Campbell & Fauchet, can be easily resolved by choosing the square wave function, since the proper boundary conditions would be then clearly set at the edges of the nanocrystallites.

In addition, it was proven in this model, that the results obtained by a rectangular phonon confinement function are in closer agreement with the choice of Richter et al., who proposed that the Gaussian falls to an amplitude of 1/e at the crystallite boundary.

- Dispersion Relations

The RCF model proposes the following Lorentzian form for fitting of a Raman signal:

$$I(w) \sim \int d^3q |C(0, q)|^2 / \{ [w - w_0(q)]^2 + \left(\frac{\Gamma}{2}\right)^2 \}$$

Where $w_0(q)$ is the phonon-dispersion function.

It should be noted that many authors have performed the integration over the \mathbf{q} in the first Brillouin zone [74, 76, 77]. However, this is incorrect since the periodicity of the lattice is broken at the very moment when the weighting function (confinement function) $W(r)$ is introduced. Therefore, the correct way is to integrate \mathbf{q} from $-\infty$ to $+\infty$.

But it is worth mentioning, that for small crystals shapes, where the nanostructure characteristic size d is several times bigger than the lattice parameter, in that case the difference between integrating over the Brillouin zone and from $-\infty$ to $+\infty$ can become important.

Nevertheless, and as mentioned earlier in this chapter, the RCF model assumes the validity of bulk phonon dispersion for nanostructures, then the only sizes of nanostructures discussed are those that are at least ten times bigger than the lattice size of the bulk material. Under these conditions, the integration over the \mathbf{q} in the first Brillouin zone is valid.

In most cases, where the crystal structure of the nanostructured material is known and is the same for all crystallographic planes, then the phonon-dispersion function $w_0(q)$ applied is isotropic [74,76].

In another work done by Bassi et al., the latter suggested the importance of using the following phonon-dispersion function: $w_0(q_x, q_y, q_z)$ in an anisotropic crystal. While, Paillard et al., proposed a sum rule which averages over different phonon branches in all relevant crystal directions, for powders which exhibit anisotropy of phonon-dispersion. It should be noted that the second approach is only good if all directions are considered to be equivalent.

However, since this work deals with nanowires, there are different dimensions in various directions. Thus, this implies the use of different weighting functions $W(r)$ with different parameters that correspond to nanostructure sizes that are used for each direction. Hence, the sum rule proposed by Paillard et al. ,which averages $w_0(q)$, is not the proper way to describe the system.

As for the approach that is adopted in this work, it indirectly includes the phonon-dispersion function in several relevant crystallographic directions, under the assumption that the bulk phonon dispersion holds for nanostructures, and that the same surface-selection rules apply.

This approach weighs a major significance on a proper phonon-dispersion function $w_0(q_x, q_y, q_z)$, for it holds many benefits that can be summarized as following:

First, a proper $w_0(q_x, q_y, q_z)$ accounts for a strong anisotropy in anisotropic crystals, where the isotropic function $w_0(q)$ is inappropriate. Second, it accounts for dimensionality in crystals, where the appropriate length scales in the x, y and z directions differ, as in nanowires.

In this part of the chapter, an algebraic approach which allows the inclusion of an anisotropic phonon-dispersion function $w_0(q_x, q_y, q_z)$ in the RCF model is demonstrated, and hence the aim of this paper is to reveal the effects of the insertion of the anisotropy into the RCF model.

This approach is based on the following assumptions:

- a. The derivation is performed in the framework of the RCF phonon confinement model, which assumes that the bulk phonon modes can be used to describe nanostructures, while the surface modes are not taken into account.
- b. This derivation assumes that the Raman surface-selection rules, which are valid for bulk, hold for the nanostructures.
- c. This part includes only two major modes, the LO and the TO, as allowed by Raman surface-selection rules for appropriate surface orientations, respectively.

Two cases can be considered: one where the Raman-scattering directions are in $\langle 001 \rangle$ or $\langle 110 \rangle$ crystallographic directions. The other case considers Raman scattering in $\langle 111 \rangle$, $\langle 112 \rangle$ and $\langle 110 \rangle$ crystallographic directions.

The derivation of the $w_0(q_x, q_y, q_z)$ for the latter case is given in the Appendix A.

In this work, the experimental part is done using germanium Ge nanowires which are oriented along the $\langle 110 \rangle$ axes. Then, the shape of the nanowire is approximated as a rectangular box in the Cartesian system for simplicity, while the dispersion relations are chosen in three different orthogonal directions: $[110]$, $[001]$ and $[1\bar{1}0]$.

Writing down an analytical form for the dispersion function in bulk Ge [67], by following a Fourier-type expansion:

$$w(q) = A_0 + \sum_n A_n \cos(n\pi q) \quad (\text{Eq. 9})$$

Where q is the normalized parameter of the reciprocal lattice.

As for the equation of $w_0(q_1, q_2, q_3)$ which is required for simulations of the Raman signal, it involves a superposition of three properly parameterized forms of (Eq. 9) to accommodate the three possible solutions for $w_{110}(q_1)$, $w_{001}(q_2)$ and $w_{1\bar{1}0}(q_3)$, since q_1 , q_2 and q_3 are the wave-vector parameters in the $[110]$, $[001]$ and $[1\bar{1}0]$ directions.

Therefore, the equation would be:

$$w_0(q_1, q_2, q_3) = C_0 + \sum_{i=1}^3 \sum_{n=1}^{\infty} C_n^i \cos(n\pi q_i) \quad (\text{Eq. 10})$$

With the expansion being performed up to $n=4$.

The boundary conditions necessary for the fulfillment of equation 10 are the following:

$$w_0(q_1, 0, 0) = w_{110}(q_1)$$

$$w_0(0, q_2, 0) = w_{1\bar{1}0}(q_2)$$

$$w_0(0, 0, q_3) = w_{001}(q_3)$$

Where $w_{110}(q_1)$, $w_{1\bar{1}0}(q_2)$ and $w_{001}(q_3)$ are given by Eq. 9 with the appropriate parameters from the Table I below [66]. Thus, to obtain $w_0(q_1, q_2, q_3)$ it is required to solve 13 boundary equations, starting at the line-width Γ of the first Brillouin zone.

$$w_0(0,0,0) = \text{constant} = w_{110}(q_1 = 0) = w_{1\bar{1}0}(q_2 = 0) = w_{001}(q_3 = 0)$$

Relevant mode	A_0 (cm^{-1})	A_1 (cm^{-1})	A_2 (cm^{-1})	A_3 (cm^{-1})	A_4 (cm^{-1})
$\langle 110 \rangle$ TO	284.9	15.13	2.84	0.65	0.21
$\langle 001 \rangle$ LO	286.3	24	-8.4	2.8	-0.9

Table I. Parameters used to fit the phonon dispersion using Eq. (9) for three major crystallographic axes in Ge. Two of the relevant axes in a nanowire are considered in $\langle 110 \rangle$ crystallographic directions

- The Spatial Correlation Model Used in Our Calculation of the Phonon Confinement in the Silicon Resonators

The wavefunction of a Raman active phonon mode of wavevector \mathbf{q}_0 in an infinite crystal can be written in the form

$$\Phi(\mathbf{q}_0, r) = u(\mathbf{q}_0, r) \exp(-i\mathbf{q}_0 r), \quad (1)$$

where $u(\mathbf{q}_0, r)$ is the amplitude of the wavefunction having the crystal periodicity. According to the spatial correlation model, it becomes

$$\psi(\mathbf{q}_0, r) = \Theta(r, D) \phi(\mathbf{q}_0, r) = \psi'(\mathbf{q}_0, r) u(\mathbf{q}_0, r) \quad (2)$$

in a finite crystal of size D , where $\Theta(r, D)$ is the phonon weighting function describing the strength of phonon confinement in the finite crystal (here we assume a finite spherical crystal). The function $\Psi'(\mathbf{q}_0, r)$ in Eq.2 can be expanded in a Fourier series and written in the form

$$\Psi'(\mathbf{q}_0, r) = \int C(\mathbf{q}_0, \mathbf{q}) \exp(i\mathbf{q}r) d^3 q, \quad (3)$$

where the Fourier coefficients $C(\mathbf{q}_0, \mathbf{q})$ are given by

$$C(\mathbf{q}_0, \mathbf{q}) = \frac{1}{(2\pi)^3} \int \Psi'(\mathbf{q}_0, \mathbf{q}) \exp(-i\mathbf{q}r) d^3 r. \quad (4)$$

The importance of Eq.4 stems from the fact that it demonstrates that while the Raman spectrum from an infinite crystal is determined by a phonon wavefunction, a phonon wave packet formed by a superposition of eigenfunctions with wavevectors \mathbf{q} centered at \mathbf{q}_0 determines the Raman spectrum from a finite crystal. In principle, the introduction of the phonon weighting function breaks the translational symmetry and imposes that the integral in Eq.4 extends from $-\infty$ to $+\infty$. However, if the finite crystal under consideration is at least one order of magnitude greater than the lattice constant, the bulk phonon dispersion can be adopted within the spatial correlation length model, and the integration can be performed over the wavevectors within the Brillouin zone only. Upon using Eqs.1-4, it can be found that if the first order Raman spectrum from an infinite crystal is given by

$$I_{\text{inf}}(\omega) \propto \frac{1}{\pi} \cdot \frac{\frac{1}{2}\Gamma}{(\omega(\mathbf{q}_0) - \omega)^2 + \left(\frac{1}{2}\Gamma\right)^2}, \quad (5)$$

the first order Raman spectrum from a finite crystal is given by

$$I(\omega) \propto \int |C(\mathbf{q}_0, \mathbf{q})|^2 L(\omega, \mathbf{q}) d^3q, \quad (6)$$

where Γ is the zone center optical phonon damping, $\omega(\mathbf{q}_0)$ is the zone center optical phonon frequency, and $L(\omega, \mathbf{q})$ is given by

$$L(\omega, \mathbf{q}) = \frac{1}{\pi} \cdot \frac{\frac{1}{2}\Gamma}{(\omega(\mathbf{q}) - \omega)^2 + \left(\frac{1}{2}\Gamma\right)^2}. \quad (7)$$

It can be clearly noticed from Eqs. 5 and 6 that the Raman scattering from an infinite material is a process in which the total momentum is conserved (it involves the contribution of only $\mathbf{q} \approx 0$ phonons to keep the total momentum conserved). However, the Raman scattering process from a finite crystal does not require momentum conservation and involves

contribution from optical phonons away from the Brillouin zone center. In order to account for a possible distribution of crystal sizes in the resonators, we express the first order Raman spectrum as

$$I(\omega) \propto \int_0^{\infty} F(D) \left[\int |C(\mathbf{q}_0, \mathbf{q})|^2 L(\omega, \mathbf{q}) d^3 q \right] dD \quad (8)$$

It has been demonstrated that a lognormal function best describes the size distribution of Si nanocrystals embedded in a given matrix [83-84]. Therefore, we write the size distribution $F(D)$ in the form of a lognormal function as

$$F(D) = \frac{1}{\sigma} \exp \left(- \left(\frac{(\log D - \log \bar{D})^2}{2\sigma^2} \right) \right), \quad (9)$$

where \bar{D} is the most probable size and σ is the skewness of the size distribution.

Several attempts have been made to establish a universal form for the phonon weighting function $\Theta(r, D)$. The most physically accepted forms are that of Faraci *et al.* [68-85] and that of Roodenko *et al.* [76]. In our calculation, we adopt the form of the phonon weighting function established by Roodenko *et al.* because it has the advantage of easier numerical implementation. In order to express $\omega(\mathbf{q})$ with taking into account the anisotropy of the phonon dispersion in silicon, we use the method of Paillard *et al.* [43], which is based on Brout sum rule to accurately average over different phonon branches in high symmetry crystallographic directions [86].

After presenting the different confinement models used to quantify the phonon confinement in low-dimensional crystals, in what follows, we shall examine the effect of resonators shape and size on the phonon and photon confinement.

D. Effect of the shape of the resonators in the first samples set (resonators heights ranging between 450 nm and 590 nm)

The Raman spectra of the samples of the first set (samples $S_{I,1}$ and $S_{I,2}$) are shown together with finite-difference time-domain (FDTD) simulations of the electric field distribution on the surfaces of the measured samples in FIG. 3.18 The FDTD simulations clearly show that the electric field is weakly confined in the cone-like resonators, and a noticeable amount of the electric field interacts with the Si substrate beneath the resonators. Therefore, the corresponding Raman spectrum does not exhibit neither an appreciable Raman enhancement nor a downshift and broadening. However, a stronger field confinement can be noticed in the pillar-like resonators. Therefore, the corresponding Raman spectrum exhibit Raman enhancement (a signature of field confinement in the resonators) and a downshift and broadening (a signature of phonon confinement in the resonators). Thus, in the first samples set, interaction between confined photons and confined phonons is observed only in pillar-like resonators.

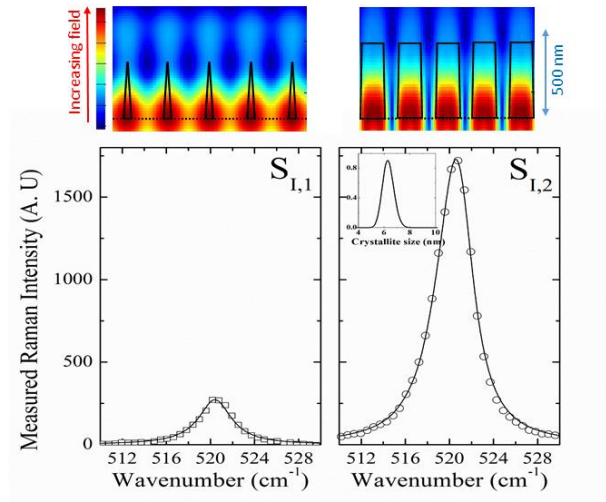


FIG. 3.18 Finite-difference time-domain (FDTD) simulations of the electric field distribution on the surfaces of the samples of the first set, and the Raman spectra corresponding to the samples of the first set. The dashed lines indicate the interface between the resonators and the Si substrate. The size and shape of the resonators of the samples investigated are shown on the top. The symbols indicate the measured Raman spectra. The solid lines indicate the calculated Raman spectra using the spatial correlation model. The derived distribution of the crystallites size in the resonator is also shown.

Several models can be used to quantify the size of the crystallites confining phonons in the pillar-like resonators from the downshift and broadening of the Raman spectrum. The most popular ones are the microscopic force model [79], the bond polarization model [80,81], and the spatial correlation models [73,82]. The spatial correlation models, however, have the advantage that they are less affected by some strong assumptions and approximations such as the continuum medium approximation. Therefore, we adopted a spatial correlation model to deduce from the downshift and broadening of the measured Raman spectrum the crystallites

size distribution in the resonators. The spatial correlation model was fitted to the measured Raman spectra with adjusting the parameters that determine the lognormal function describing the crystallites size distribution (i.e., the most probable size and the skewness of the distribution). The good agreement between the calculated and measured Raman spectra is demonstrated in FIG. 3.18 We also show in FIG. 3.18 the crystallites size distribution obtained by fitting the spatial correlation model to the measured Raman spectra. In Table I. we present the most probable crystallites size in the resonators of the measured samples.

E. Effect of the shape of the resonators in the second samples set (resonators heights ranging between 800 nm and 875 nm)

The Raman spectra and FDTD simulations of the field distribution for the samples of the second set (samples $S_{II,1}$, $S_{II,2}$, and $S_{II,3}$) are shown in FIG. 3.19 We recall here that the height of the resonators in this set is greater than that of the resonators in the first set (see Table I). The FDTD simulations in FIG. 3.19 demonstrate that a noticeable amount of the incident electric field is confined in the cone-like resonators in sample $S_{II,1}$. Therefore, the corresponding Raman spectrum exhibits a significant Raman enhancement accompanied by a downshift and broadening. The Raman enhancement is due to electric field confined in the cone-like resonators, whereas the downshift and broadening of the Raman spectrum is due to light interaction with phonons confined in nanosized crystallites in the cone-like resonators. Thus, unlike the cone-like resonators of the first set, the cone-like resonators of the second set can promote interaction between confined electric field and phonons confined in nanosized crystallites. The FDTD simulations in FIG. 3.19 also demonstrate that the field confinement gets stronger as the resonators become more pillar-like. The results of the FDTD simulations

are supported by the Raman measurements, which demonstrate that the Raman enhancement gets stronger as the diameter of the resonators at the top approaches the diameter of the resonators at the bottom. The spatial correlation model was fitted to the Raman spectra of the samples of the second set with adjusting the parameters determining the lognormal size distribution function. A very satisfactory agreement between the calculated and measured Raman spectra was obtained. The calculated Raman spectra are plotted in FIG. 3.19 using solid lines, and the crystallites size in each of the measured samples obtained from fitting the spatial correlation model to the measured Raman spectra is indicated near the corresponding Raman spectrum. We found a size distribution only for the sample having pillar-like resonators (sample $S_{II,3}$). The other samples of the second set showed monodisperse crystallites.

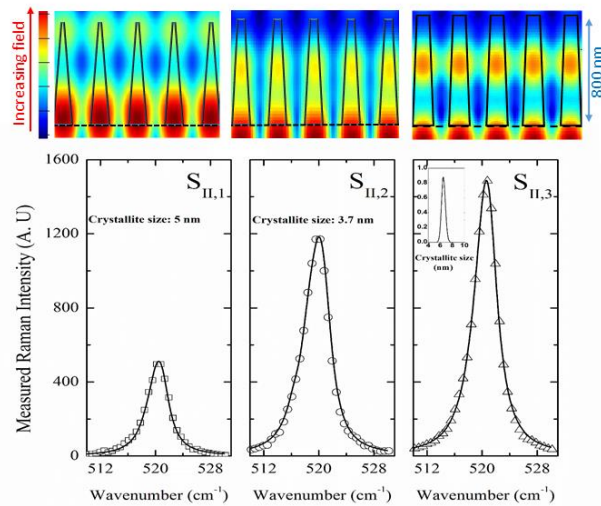


FIG. 3.19 Finite-difference time-domain (FDTD) simulations of the electric field distribution on the surfaces of the samples of the second set, and the Raman spectra corresponding to the samples of the second set. The dashed lines indicate the interface between the resonators and the Si substrate. The size and shape of the resonators of the

samples investigated are shown on the top. The symbols indicate the measured Raman spectra. The solid lines indicate the calculated Raman spectra using the spatial correlation model. The size of the crystallites is indicated by a number in the case of monodisperse crystallites or by a lognormal function in the case of polydisperse crystallites.

F. Effect of the shape of the resonators in the third samples set (resonators heights ranging between 1150 nm and 1280 nm)

The samples in the third set have the highest resonators. The Raman spectra and FDTD simulations of the field distribution for the samples of this set (samples $S_{III,1}$, $S_{III,2}$, and $S_{III,3}$) are shown in FIG. 3.20 Both Raman spectra and FDTD simulations demonstrate that the resonators of the samples in the third set are remarkably more efficient in electric field confinement than the resonators of the samples of the first and second set. However, similar to the first and second set, the field confinement gets stronger as the resonators become more pillar-like. As can be noticed from FIG. 3.20, the pillar-like resonators of sample $S_{III,3}$ in the third set confine almost the totality of the electric field. Moreover, the Raman spectrum of sample $S_{III,3}$ shows a significant downshift and broadening (see also FIG. 3.8). Therefore, among all the measured samples, sample $S_{III,3}$, which is characterized by the highest pillar-like resonators, best ensures the desirable interaction between confined photons and confined phonons. The measured Raman spectra of the samples of the third set were analyzed using the spatial correlation model, and the crystallites sizes in the measured samples were obtained by fitting the spatial correlation model to the measured Raman spectra. The calculated Raman spectra are plotted in FIG. 3.20 using solid lines, and the obtained crystallites size in each of the measured samples is indicated near the corresponding Raman spectrum. For this samples

set, we found that only the sample having cone-like resonators (sample $S_{III,1}$) presents a size distribution. The others samples of the set showed monodisperse crystallites.

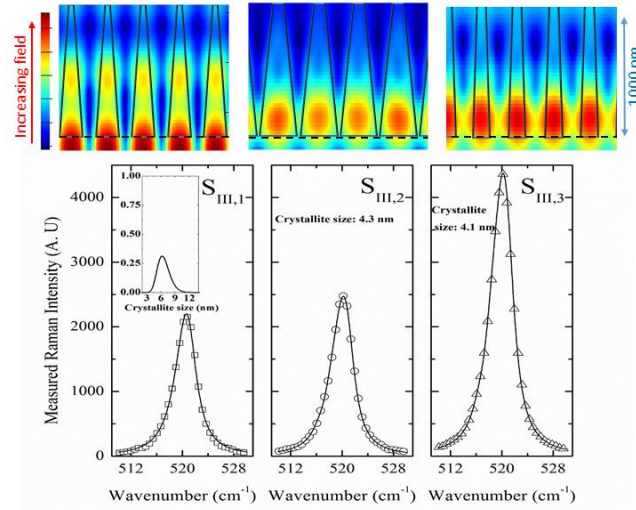


FIG. 3.20 Finite-difference time-domain (FDTD) simulations of the electric field distribution on the surfaces of the samples of the third set, and the Raman spectra corresponding to the samples of the third set. The dashed lines indicate the interface between the resonators and the Si substrate. The size and shape of the resonators of the samples investigated are shown on the top. The symbols indicate the measured Raman spectra. The solid lines indicate the calculated Raman spectra using the spatial correlation model. The size of the crystallites is indicated by a number in the case of monodisperse crystallites or by a lognormal function in the case of polydisperse crystallites.

G. Comparative evaluation of the effect of resonators size and shape on the interaction between confined photons and confined phonons

The Raman spectra and FDTD simulations carried out on the samples of the three samples sets described in Table I. revealed important information about the effect of the resonators shape and size on the confinement of photon and phonon. By comparing the FDTD simulations of the electric field distributions and the Raman enhancements shown in FIG. 3.18, FIG.3.19, and FIG. 3.20, we notice that the field confinement gets stronger as the resonators height is increased. On the other hand, by comparing the FDTD simulations and Raman enhancements shown in each of FIG. 3.18, FIG. 3.19, and FIG. 3.20, we notice that the field confinement gets stronger as the resonators shape becomes cylindrical. Moreover, we can notice from FIG. 3.20 that, although the volume of the resonators of sample $S_{III,2}$ is greater than that of the resonators of sample $S_{III,3}$, the confinement of the electric field in sample $S_{III,2}$ is weaker than that in sample $S_{III,3}$. These results suggest the following. While the volume of the resonators does not present an appreciable effect on the electric field confinement in the resonators, the height and shape of the resonators are key parameters determining the strength of the field confinement in the dielectric resonators. The confinement of the electric field gets stronger as the resonators increase in height and their shape becomes cylindrical. We believe that this is because the highest cylindrical resonators can attain the greatest oscillation amplitude, which is the prime determinant of field confinement. As the resonators height decreases and their shape deviates from the ideal cylindrical shape, the resonators lose their ability to vibrate, and consequently lose their efficiency in confining the incident electric field. Phonon confinement in crystallites of comparable sizes was observed in all the measured samples. This suggests that the resonators

size and shape do not have an appreciable effect on the spatial correlation length in the resonators. Consequently, long cylindrical resonators arranged on two-dimensional lattice points over a large area present great potential for confining an important amount of the incident electric field and promoting the interaction between the confined electric field and phonons confined in nanosized crystallites. Such an interaction significantly enhances the photovoltaic processes in Si because it strongly amplifies the number of photons interacting with Si and does not require total momentum conservation.

H. Electric field confinement causes substantial crystallites heating in the resonators

It is now well known that high laser powers can accumulate an important amount of energy in nanosized crystallites (because of their low thermal properties), and hence distort their Raman spectrum by strengthening the effects of laser heating and Fano resonance. It was found that the threshold power for the effects of laser heating and Fano resonance in nanosized Si crystallites is about $1\text{mW}/\mu\text{m}^2$ [67,68]. As mentioned previously, in order to rule out the effect of laser heating and laser-induced Fano resonance, we have decreased the excitation laser power successively until the Raman spectrum became independent of laser power. However, we found effects of Fano resonance and laser heating in the samples measured in this work for a laser power as low as $0.2\text{ mW}/\mu\text{m}^2$. For samples $S_{\text{II},3}$ and $S_{\text{III},3}$ (the samples with pillar-like resonators), which showed the strongest field confinement, the effects of Fano resonance and laser heating vanished completely only for a laser power as low as $0.1\text{ mW}/\mu\text{m}^2$. Based on the discussion above, we attribute this to the fact that the electric field confinement in the resonators increases significantly the temperature of the crystallites embedded in the resonators. In FIG.3.21, we show the Raman spectra of samples

$S_{II,3}$ and $S_{III,3}$ measured with a laser power of $1\text{mW}/\mu\text{m}^2$ (the reported threshold power for the effects of laser heating and Fano resonance) and a laser power of $0.1\text{ mW}/\mu\text{m}^2$. The spectra are normalized for the sake of comparison. The spectra measured with a laser power of $1\text{mW}/\mu\text{m}^2$ are heavily distorted. A downshift and asymmetric broadening relative to the spectra measured with a laser power of $0.1\text{ mW}/\mu\text{m}^2$ can be clearly noticed. This further highlights the strength of the electric field that can be confined in arrays of dielectric resonators.

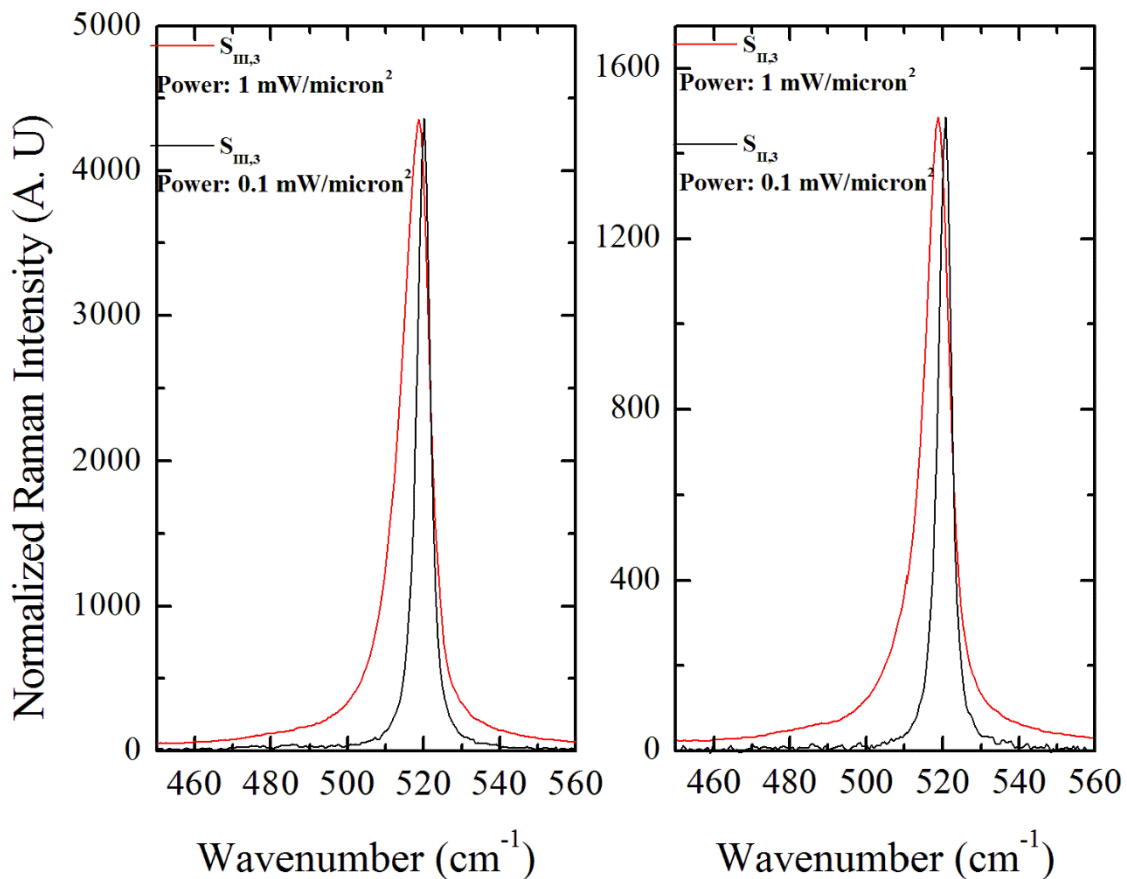


FIG. 3.21 Raman spectra of samples $S_{II,3}$ and $S_{III,3}$ measured with a laser power of $1\text{mW}/\mu\text{m}^2$ (the reported threshold power for the effects of laser heating and Fano resonance) and a laser power of $0.1\text{ mW}/\mu\text{m}^2$. The spectra are normalized for the sake of comparison.

I. CONCLUSION

In this thesis, two models are presented that aim at enhancing the photovoltaic effect in Silicon-based solar cells are presented.

Our first attempt at a solution, consisted of the random deposition of Zinc Oxide nanowires ZnO NWs, of different diameters and different heights, on a Silicon substrate.

The Raman light scattering measurements of these samples showed an appreciable Raman enhancement relative to the Raman spectrum from a bare Si substrate. However, the Raman spectra did not exhibit any signatures of light interaction with ZnO. Thus, it was believed that the localized Mie resonance in the ZnO cylindrical resonators induced forward scattering of the normally incident light into the Si substrate, beneath the resonators, on which the ZnO nanowires are deposited, and therefore leading to the presence of a strong field in the Si substrate; this being the reason behind the Raman peak enhancement. In other words, the Raman peak enhancement is purely characteristic of the Silicon and it does not feature any characteristic peak that belongs to the ZnO NWs.

This solution solved only one aspect of the problem regarding the photovoltaic enhancement in Si, which is the reduction of the lossy light, and proved that ZnO nanowires deposited on a Si substrate can be crucial and beneficial in trapping light within the latter. However, this method did not achieve the coupling between light and nanosized crystallites in which phonons are confined, and therefore did not yield the expected results in terms of enhancing the photovoltaic effect in Silicon-based solar cells.

On the other hand, in the second model, Raman spectra from large arrays of dielectric Si resonators attached to Si substrates showed an appreciable Raman enhancement accompanied by a downshift and broadening relative to the Raman spectrum from a bare Si substrate. FDTD simulations demonstrated that the collective lattice resonance induces an efficient field confinement in the resonators, which results in an appreciable Raman enhancement. A spatial correlation model demonstrated that the spectrum downshift and broadening is the result of the relaxation of the phonon wavevector, which is due to phonon confinement in nanosized Si crystallites in the resonators. The effect of resonators size and shape on the confinement of photons and phonons was investigated. It was demonstrated that, as the resonators increase in height and their shape become cylindrical, the amplitude of their coherent oscillation increases and hence their ability to confine the incoming electric field increases. However, it was found that the resonators shape and size do not have a remarkable effect on phonon confinement. The results presented in this work show that large arrays of long cylindrical dielectric Si resonators drastically suppress the light scattering losses by field confinement and promote the interaction of the confined field with confined phonons. The observed amplified photon-phonon non-conservative interaction mechanism has great potential for strongly enhancing the photovoltaic effect in Si.

Bibliography

- [1] Conibeer, G. (2007). Third-generation photovoltaics. *Materials today*, 10(11), 42-50.
- [2] Bharam, V., & Day, D. Advantages and challenges of silicon in the photovoltaic cells.
- [3] Krebs, F. C., Hösel, M., Corazza, M., Roth, B., Madsen, M. V., Gevorgyan, S. A., & Jørgensen, M. (2013). Freely available OPV—the fast way to progress. *Energy Technology*, 1(7), 378-381.
- [4] Aribisala, H. A. (2013). *Improving the efficiency of solar photovoltaic power system*. University of Rhode Island.
- [5] Solar Cell Central. P/N Junctions. Retrieved from http://solarcellcentral.com/junction_page.html
- [6] American Chemical Society. How a Solar Cell Works. Retrieved from https://www.acs.org/content/acs/en/education/resources/highschool/chemmatters/past-issues/archive-2013-2014/how-a-solar-cell-works.html?cq_ck=1396892718960
- [7] Lin, K. T., Chi, Y. M., Chen, H. L., Tseng, S. C., Chang, H. M., Liao, Y. C., & Lai, Y. S. (2014, July). Enhanced efficiency of silicon-based solar cell by surface plasmon resonance effects over device electrode. In *Active-Matrix Flatpanel Displays and Devices (AM-FPD), 2014 21st International Workshop on* (pp. 307-310). IEEE.
- [8] Matsui, T., Sai, H., Saito, K., & Kondo, M. (2013). High-efficiency thin-film silicon solar cells with improved light-soaking stability. *Progress in Photovoltaics: Research and Applications*, 21(6), 1363-1369.
- [9] A. K. Arora, M. Rajalakshmi, T. R. Ravindran, V. Sivasubramanian, J. Raman Spectrosc. 38, 604 (2007).
- [10] E. Yablonovitch, J. Opt. Soc. Am. **72**, 899 (1982).
- [11] S. Koynov, M. S. Brandt, and M. Stutzmann, Appl. Phys. Lett. **88**, 203107 (2006).

- [12] R. Shuker and R. W. Gammon, *Phys. Rev. Lett.* **25**, 222 (1970).
- [13] K. K. toing, P. M. Amirtharaj, F. H. Pollak, and D. E. Aspnes, *Appl. Phys. Lett.* **44**, 122 (1984).
- [14] H. A. Atwater and A. Polman, *Nat. Mater.* **9**, 205 (2010).
- [15] K. T. Carron, W. Fluhr, M. Meier, A. Wokaun, and H. W. Lehmann, *J. Opt. Soc. Am. B* **3**, 430 (1986).
- [16] S. L. Zou, N. Janel, and G. C. Schatz, *J. Chem. Phys.* **120**, 10871 (2004).
- [17] S. L. Zou and G. C. Schatz, *Chem. Phys. Lett.* **403**, 62 (2005).
- [18] P. Spinelli, M. A. Verschuuren, and A. Polman, *Nat. Commun.* **3**, 692 (2012).
- [19] F. J. Bezares, J. P. Long, O. J. Glembocki, J. Guo, R. W. Rendell, R. Kasica, L. Shirey, J. C. Owrutsky, and J. D. Caldwell, *Opt. Express* **21**, 27587 (2013).
- [20] A. B. Evlyukhin, C. Reinhardt, A. Seidel, B. S. Luck'yanchuk, and B. N. Chichkov, *Phys. Rev. B* **82**, 045404 (2010).
- [21] S. Tsoi, F. J. Bezares, A. Giles, J. P. Long, O. J. Glembocki, J. D. Caldwell, and J. Owrutsky, *Appl. Phys. Lett.* **108**, 111101 (2016).
- [22] S. G. Cloutier, C.- H. Hsu, P. A. Kossyrev, and J. Xu, *Adv. Mater.* **18**, 841 (2006).
- [23] S. G. Cloutier, R. S. Guico, and J. M. Xu, *Appl. Phys. Lett.* **87**, 222104 (2005).
- [24] M. Hofmann, Y.- P. Hsieh, C.- T. Liang, and Y.- F. Chen, *J. Raman Spectrosc.* **44**, 81 (2013).
- [25] D. Banerjee, C. Trudeau, L. F. Gerlein, and S. G. Cloutier, *Appl. Phys. Lett.* **108**, 113109 (2016).
- [26] A. L. Bassi, D. Cattaneo, V. Russo, C. E. Bottani, E. Barborini, T. Mazza, P. Piseri, P. Milani, F. O. Ernst, K. Wegner, and S. E. Pratsinis, *J. Appl. Phys.* **98**, 074305 (2005).

- [27] A. C. A. Silva, E. S. F. Neto, S. W. da Silva, P. C. Morais, and N. O. Dantas, *J. Phys. Chem.* **117**, 1904 (2013).
- [28] Hu, H., Huang, X., Deng, C., Chen, X., & Qian, Y. (2007). Hydrothermal synthesis of ZnO nanowires and nanobelts on a large scale. *Materials Chemistry and Physics*, **106**(1), 58-62.
- [29] Unalan, H. E., Hiralal, P., Rupesinghe, N., Dalal, S., Milne, W. I., & Amaratunga, G. A. (2008). Rapid synthesis of aligned zinc oxide nanowires. *Nanotechnology*, **19**(25), 255608.
- [30] Matos, A. L., & Fonseca, L. C. (2015). *Electric and Magnetic Properties of Iron Manganese Silicide Nanowires* (Doctoral dissertation).
- [31] Lupan, O., Emelchenko, G. A., Ursaki, V. V., Chai, G., Redkin, A. N., Gruzintsev, A. N., & Heinrich, H. (2010). Synthesis and characterization of ZnO nanowires for nanosensor applications. *Materials Research Bulletin*, **45** (8), 1026-1032.
- [32] Steiner, T. D., p. 195, (2004). *Semiconductor nanostructures for optoelectronic applications*. Artech House.
- [33] Huang, M. H., Wu, Y., Feick, H., Tran, N., Weber, E., & Yang, P. (2001). Catalytic growth of zinc oxide nanowires by vapor transport. *Advanced Materials*, **13** (2), 113-116.
- [34] Gwiazda, A., Romyantseva, A., Gokarna, A., Nomenyo, K., Chevalier-César, C., & Léronnel, G. (2017). Simple and Versatile High Aspect Ratio Nanostructuring via Zinc Oxide Masking. *Advanced Materials Technologies*.
- [35] Sajjad Hussain. Investigation of structural and optical properties of nanocrystalline zno. 2008.

- [36] Encyclopedia Britannica. Bragg's law – Crystals. Retrieved from <https://www.britannica.com/science/Bragg-law>
- [37] Zak A K, Abd. Majid W H, Abrishami M E and Yousefi R 2011 *Solid State Sciences* 13 251–256.
- [38] M. E. Rabanal, A. Vrez, B. Levenfeld and J. M. Torralba, *J. Mater. Process. Tech.* 143- 144, 470 (2003).
- [39] Semrock. Filter Types For Raman Spectroscopy Applications. Retrieved from <https://www.semrock.com/filter-types-for-raman-spectroscopy-applications.aspx>
- [40] Mirvat Shams Eddine. Optical analysis of boron nitride thin films. Master's thesis, American University of Beirut, 2012.
- [41] Reham Issam Abu Amer. Crystalline and Optical Properties of Zinc Oxide Nanoparticles Synthesized by a Solvent Based Technique. Master's thesis, American University of Beirut, 2015.
- [42] P. G. Klemens, *Physica B* 316-317, 413 (2002).
- [43] V. Paillard, P. Puech, R. Sirvin, S. Hamma, and P. R. i Cabarrocas, *J. Appl. Phys.* 90, 3276 (2001).
- [44] A. Compaan, M. C. Lee, and G. J. Trott, *Phys. Rev, B* 32, 6731 (1985).
- [45] V. Magidson, and R. Beserman, *Phys. Rev. B* 66, 195206 (2002).
- [46] N. H. Nickel, P. Lengsfeld, and I. Sieber, *Phys. Rev. B* 61, 15558 (2000).
- [47] M. Kazan, C. Zgheib, E. Moussaed, and P. Masri, *Diam. Relat. Mat.* **15**, 1169 (2006).
- [48] K. Nagata, M. Takei, A. Ogura, and K. Uchida, *Jpn. J. Appl. Phys.* 53, 032401 (2014).
- [49] P. M. Fauchet, and I. H. Campbell, *Crit. Rev. Solid State Mat. Sci.* 14, S79 (2006).

- [50] S. Piscanec, M. Contoro, A. C. Ferrari, J. A. Zapien, Y. Lifshitz, S. T. Lee, S. Hofmann, and J. Robertson, *Phys. Rev. B* 68, 241312 (2003).
- [51] Yang, P., Yan, H., Mao, S., Russo, R., Johnson, J., Saykally, R., & Choi, H. J. (2002). Controlled growth of ZnO nanowires and their optical properties. *Advanced Functional Materials*, 12 (5), 323.
- [52] Wang, Z. L. (2004). Zinc oxide nanostructures: growth, properties and applications. *Journal of Physics: Condensed Matter*, 16 (25), R829.
- [53] Wang, Z. L. (2004). Nanostructures of zinc oxide. *Materials today*, 7(6), 26-33.
- [54] Lu, J. G. (2012). Fundamental Properties of Zinc Oxide Nanowires. In *Encyclopedia of Nanotechnology* (pp. 919-927). Springer Netherlands.
- [55] Eranna, G. (2011). *Metal oxide nanostructures as gas sensing devices*. CRC Press.
- [56] Janotti, A., & Van de Walle, C. G. (2009). Fundamentals of zinc oxide as a semiconductor. *Reports on progress in physics*, 72 (12), 126501.
- [57] Rodnyi, P. A., & Khodyuk, I. V. (2011). Optical and luminescence properties of zinc oxide. *Optics and Spectroscopy*, 111 (5), 776-785.
- [58] Sidiropoulos, T. P., Röder, R., Geburt, S., Hess, O., Maier, S. A., Ronning, C., & Oulton, R. F. (2016, June). Ultrafast ZnO nanowire lasers: nanoplasmonic acceleration of gain dynamics at the surface plasmon polariton frequency. In *Lasers and Electro-Optics (CLEO), 2016 Conference on* (pp. 1-2). IEEE.
- [59] Oulton, R. F., Sorger, V. J., Zentgraf, T., Ma, R. M., Gladden, C., Dai, L., ... & Zhang, X. (2009). Plasmon lasers at deep subwavelength scale. *Nature*, 461 (7264), 629.
- [60] Yoshikawa, H., & Adachi, S. (1997). Optical constants of ZnO. *Japanese Journal of Applied Physics*, 36 (10R), 6237.

- [61] Kneipp, K., Wang, Y., Kneipp, H., Perelman, L. T., Itzkan, I., Dasari, R. R., & Feld, M. S. (1997). Single molecule detection using surface-enhanced Raman scattering (SERS). *Physical review letters*, 78 (9), 1667.
- [62] Anker, J. N., Hall, W. P., Lyandres, O., Shah, N. C., Zhao, J., & Van Duyne, R. P. (2008). Biosensing with plasmonic nanosensors. *Nature materials*, 7 (6), 442-453.
- [63] Danckwerts, M., & Novotny, L. (2007). Optical frequency mixing at coupled gold nanoparticles. *Physical Review Letters*, 98 (2), 026104.
- [64] Kim, S. W., Kim, S., Park, I. Y., & Choi, J. (2010, May). High-harmonic generation by resonant plasmon field enhancement. In *Conference on Lasers and Electro-Optics* (p. CThQ1). Optical Society of America.
- [65] Yu, Z., Veronis, G., Fan, S., & Brongersma, M. L. (2008). Gain-induced switching in metal-dielectric-metal plasmonic waveguides. *Applied Physics Letters*, 92 (4), 041117.
- [66] Baca, A. G., Brown, J., Buckley, D. N., Nam, P., O'Dwyer, C., & Etcheberry, A. (2009). State-of-the-art program on compound semiconductors 50 (SOTAPOCS 50)-and-processes at the semiconductor solution interface 3. *The Electrochemical Society, New Jersey*.
- [67] Soudi, A., Dhakal, P., & Gu, Y. (2010). Diameter dependence of the minority carrier diffusion length in individual ZnO nanowires. *Applied Physics Letters*, 96(25), 253115.
- [68] G. Faraci, S. Gibilisco, and A. R. Pennisi, *Phys. Rev. B* 80, 193410 (2009).
- [69] R. Gupta, Q. Xiong, C. K. Adu, U. J. Kim, and P. C. Eklund, *Nano Lett.* 3, 627 (2003).

- [70] A. Iskandar, A. Gwiazda, Y. Huang, M. Kazan, A. Bruyant, M. Tabbal, and G. Lerondel, *J. Appl. Phys.* 120, 095106 (2016).
- [71] S. Hayashi, M. Ito, and H. Kanamori *Solid State Commun.* 44, 75 (1982).
- [72] S. Hayashi, and Y. Yamamoto, *Superlattices Microstruct.* 2, 581 (1986).
- [73] Richter, H., Wang, Z. P., & Ley, L. (1981). The one phonon Raman spectrum in microcrystalline silicon. *Solid State Communications*, 39(5), 625-629.
- [74] Campbell, I. H., & Fauchet, P. M. (1986). The effects of microcrystal size and shape on the one phonon Raman spectra of crystalline semiconductors. *Solid State Communications*, 58(10), 739-741.
- [75] Tiong, K. K., Amirtharaj, P. M., Pollak, F. H., & Aspnes, D. E. (1984). Effects of As⁺ ion implantation on the Raman spectra of GaAs: “Spatial correlation” interpretation. *Applied Physics Letters*, 44(1), 122-124.
- [76] Roodenko, K., Goldthorpe, I. A., McIntyre, P. C., & Chabal, Y. J. (2010). Modified phonon confinement model for Raman spectroscopy of nanostructured materials. *Physical Review B*, 82(11), 115210.
- [77] S. Piscanec, M. Cantoro, A. C. Ferrari, J. A. Zapien, Y. Lifshitz, S. T. Lee, S. Hofmann, and J. Robertson, *Phys. Rev. B* 68, 241312 2003.
- [78] A. Li Bassi *et al.*, *J. Appl. Phys.* 98, 074305 2005.
- [79] W. Cheng, and S.- F. Ren, *Phys. Rev. B* 65, 205305 (2002).
- [80] J. Zi, K. Zhang, and X. Xie, *Phys. Rev. B* 55, 9263 (1997).
- [81] T. Thonhauser, and G. D. Mahan, *Phys. Rev. B* 71, 081307 (2005).
- [82] P. Parayanthal, and F. H. Pollak, *Phys. Rev. Lett.* 52, 1822 (1984).
- [83] K. W. Adu, H. R. Gutiérrez, U. J. Kim, G. U. Sumanasekera, and P. C. Eklund, *Nano Lett.* 5, 409 (2005).

- [84] P. Zhang, Y. Feng, R. Anthony, U. Kortshagen, G. Conibeer, and S. Huang, *J. Raman Spectrosc.* 46, 1110 (2015).
- [85] G. Faraci, G. Mannino, A. R. Pennisi, R. Ruggeri, P. Sberna, and V. Privitera, *J. Appl. Phys.* 113, 063518 (2013).
- [86] R. Brout, *Phys. Rev.* 113, 43 (1959).

